Studies on electromagnetically induced transparency in ^{87}Rb atoms

By

CHARU MISHRA

PHYS03201404009

Raja Ramanna Centre for Advanced Technology, Indore

A thesis submitted to the

Board of Studies in Physical Sciences

In partial fulfillment of requirements

For the Degree of

DOCTOR OF PHILOSOPHY

of

HOMI BHABHA NATIONAL INSTITUTE

August, 2020

Homi Bhabha National Institute[1]

Recommendations of the Viva Voce Committee

As members of the Viva Voce Committee, we certify that we have read the dissertation prepared by **Ms. Charu Mishra** entitled **"Studies on electromagnetically induced transparency in ^{87}Rb atoms"** and recommend that it may be accepted as fulfilling the thesis requirement for the award of Degree of Doctor of Philosophy.

Chairman - Name & Signature with date : **Dr S. K. Dixit**	21/8/2020
Guide / Convener - Name & Signature with date: **Dr S. R. Mishra**	SRMishra 21.8.2020
Co-guide - Name & Signature with date (if any)	
Examiner - Name & Signature with date: **Dr Poonam Arora**	Poonam Arora 21/08/2020
Member 1- Name & Signature with date : **Dr J. A. Chakera**	21/8/2020
Member 2- Name & Signature with date : **Dr S. K. Majumder**	21/08/2020
Member 3- Name & Signature with date : **Dr S. Pradhan**	Pradhan 21/08/2020

Final approval and acceptance of this thesis is contingent upon the candidate's submission of the final copies of the thesis to HBNI.

I/We hereby certify that I/we have read this thesis prepared under my/our direction and recommend that it may be accepted as fulfilling the thesis requirement.

Date: **21st August, 2020**

SRMishra 21.8.2020

Place: **Signature** **Signature**

Co-guide (if any) **Guide**

[1] This page is to be included only for final submission after successful completion of viva voce.

STATEMENT BY AUTHOR

This dissertation has been submitted in partial fulfillment of requirements for an advanced degree at Homi Bhabha National Institute (HBNI) and is deposited in the Library to be made available to borrowers under rules of the HBNI.

Brief quotations from this dissertation are allowable without special permission, provided that accurate acknowledgement of source is made. Requests for permission for extended quotation from or reproduction of this manuscript in whole or in part may be granted by the Competent Authority of HBNI when in his or her judgment the proposed use of the material is in the interests of scholarship. In all other instances, however, permission must be obtained from the author.

Charu Mishra

(Charu Mishra)

DECLARATION

I, hereby declare that the investigation presented in the thesis has been carried out by me. The work is original and has not been submitted earlier as a whole or in part for a degree / diploma at this or any other Institution / University.

Charu Mishra

(Charu Mishra)

List of Publications arising from the thesis

Journal:

1. "Electromagnetically Induced Transparency in Λ-systems of ^{87}Rb atom in magnetic field", Charu Mishra, A. Chakraborty, A. Srivastava, S. K. Tiwari, S. P. Ram, V. B. Tiwari and S. R. Mishra, J. Mod. Opt., **2018**, 65 (20), 2269-2277.

2. "Coupling field dependent quantum interference effects in a Λ-system of ^{87}Rb atom", Charu Mishra, A. Chakraborty, Vivek Singh , S. P. Ram, V. B. Tiwari and S. R. Mishra, Phys. Lett. A, **2018**, 382 (45), 3269-3273.

3. "Spectral characteristics of a modified inverted-Y system beyond rotating wave approximation", Charu Mishra, A. Chakraborty and S. R. Mishra, J. Phys. B: At. Mol. Opt. Phys., **2019**, 52, 095002, 1-9.

4. "On electromagnetically induced transparency in N-systems in cold ^{87}Rb atoms", Charu Mishra, A. Chakraborty, S. P. Ram, S. Singh, V. B. Tiwari and S. R. Mishra, J. Phys. B: At. Mol. Opt. Phys., **2020**, 53, 015001, 1-8.

Conferences:

1. "Probe beam intensity dependent asymmetry in Electromagnetically Induced Transparency signal of ^{87}Rb atom", Charu Mishra, A. Chakraborty, A. Srivastava, S. K. Tiwari, S. P. Ram, S. R. Mishra and H. S. Rawat, et.al, CP-4.41, Proc. DAE-BRNS National Laser Symposium (NLS-25), KIIT University, Bhubaneswar, Dec. 20-23, 2016.

2. "On resolution of electromagnetically induced transparency signals in presence of magnetic field", Charu Mishra, A. Chakrabortya, S. P. Ram, V. B. Tiwari, S. R. Mishra, CP-04.10, Proc. DAE-BRNS National Laser Symposium (NLS-26), BARC, Mumbai, Dec. 20-23, 2017.

3. "Studies on ultracold atoms in driven optical lattices", Charu Mishra, A. Chakraborty, S. R. Mishra, International conference on Recent Trends in Cold and Ultracold Matter 2018, IIT Guwahati, Assam, March 27-29, 2018.

4. "Emergence of absorption in Autler-Townes window in a Λ-system in cold ^{87}Rb atoms", Charu Mishra, A. Chakraborty, S. P. Ram, S. Singh, V. B. Tiwari, S. R. Mishra, 13^{th} European Conference on Atoms, Molecules and Photons, Florence, Italy, April 8-12, 2019.

Charu Mishra

(Charu Mishra)

Dedicated to my family

ACKNOWLEDGEMENTS

I would like to express my gratitude to people who have supported and appreciated me during my PhD journey. Foremost, I thank my supervisor Dr. Satya Ram Mishra for his constant support throughout my PhD. The interaction with him has always been inspirational. Thank you for advising and encouraging me for my research work. Besides him, I would like to acknowledge the lab members Dr. Vibhuti Tiwari, Dr. S. P. Ram, Dr. Surendra Singh, Vivek Singh and Amit Chaudhary for their help in the experiments as well as helpful suggestions. Apart from the lab, I would like to thanks Dr. Arup Banerjee for his many valuable advices over my work and for enlightening me with his deep knowledge of quantum optics during different Doctoral meetings. Also, my thanks to all my Doctoral Committee members for their constructive feedbacks and suggestions while presenting my work in front of them.

This thesis also deserves a huge thanks to my senior Dr. Arijit Chakraborty. I am very grateful to him as he always helped me out whenever I got stuck in any problem of my PhD. His enthusiastic attitude for research is very impressive. Thank you for listening my grumbling time to time. I also want to thanks my loving husband Mr. Shalabh Chaturvedi for his support and encouragement during my thesis writting. You have always been an inspirational to me. I thank my friends for providing a healthy environment both in the hostel and department. Thank you for creating beautiful memories of playing volleyball together, tea in the evenings, get-together for lunch or dinner, many useless gossips and helps in different ways. Your company is unforgetable.

I cannot complete this without acknowledging my family. They understood me these years and always been supportive to me. Thank you for letting me choose my career as I wanted to.

Table of Contents

List of Figures

List of Tables

Chapter 5

Summary and outlook

5.1 Summary

This thesis describes the experimental and theoretical study of electromagnetically induced transparency in different schemes prepared in ^{87}Rb atoms at room temperature and in cold atom cloud trapped in a magneto-optical trap (MOT). The EIT offers control in laser absorption in a medium, and also provides a degree of freedom to manipulate the spectral features with a large number of additional coupling fields connected with the system. In this respect, the study is initially carried out in Λ-systems and then proceeded in more complex structures like N-system and modified inverted-Y system.

Initially, a comparative study of EIT has been carried out in two Λ systems in D_2 line transition of ^{87}Rb atom in order to ascertain a better EIT signal from application point of view [87]. This experimental and theoretical study is carried out in absence and presence of a longitudinal magnetic field. During this study, we have obtained that one of the two Λ-systems exhibit stronger and more symmetric EIT signal than that in other Λ-system in absence of the magnetic field. The presence of the magnetic field splits single EIT into three EIT signals for both the Λ systems, and it has been obtained that at higher coupling power central EIT peak of prevailed Λ-system exhibit larger slope than the EIT signal in absence of magnetic field. Further, we proceeded our study in the prevailed Λ-system with a standing wave coupling field, where electromagnetically induced absorption (EIA) signal instead of EIT signal has been observed. The slope of this EIA signal, EIT signal in absence and presence of magnetic field is calculated for different coupling power and is obtained that EIA signal has largest slope compared to rest of the two signals for each coupling power [9]. Thus, it is interpretated that the EIA signal in presence of standing wave coupling beam can be preferably used for tight laser frequency locking with higher stability and performances.

Subsequently, the EIT in an extension of Λ-system, *i.e.* N-system, has been investigated in cold ^{87}Rb atoms trapped in a MOT. The cold atom cloud diminishes the Doppler effect as well as reduce the collisional dephasing rate in the atomic system. The study is carried out in two N-systems which are prepared with a scan of probe beam frequency and fixed frequency of two drive beams in D_2 line transition of ^{87}Rb atom. To consolidate the experimental observations, numerical study has also been made by solving Liouville equation using density matrix formalism. The probe transmission spectrum of both the N-systems has shown dual EIT structure due to emergence of a transmission dip at center of Autler-Townes splitting, which is qualitatively explained using semi-classical dressed state approach. In the parametric dependent study, it is obtained that coupling and control beam of N-system governs the side transmission dips and central transmission dip respectively [107]. The absorption or transparency in the probe transmission spectrum can be controlled with the detuning of coupling and control beam, which finds application in optical switching device.

The study of EIT is then carried out theoretically in a more complex structure, *i.e.* in a modified inverted-Y system (IY^+-system), using a numerical matrix propagation (NMP) method [108]. This system comprises of all the basic systems like Λ-, ladder-, vee-, N- and inverted-y system that can exhibit EIT signal. This IY^+-system offers investigation of interdependence of each basic systems on other basic systems. In NMP-method, a density matrix has been propagated with respect to time in order to study transient characteristics and to obtain the steady state condition. By comparing the probe absorption spectrum of inverted-Y system obtained from rotating wave approximation and NMP method, the validity of NMP method is established. The spectral characteristics of IY^{+}-system depending on strength and detuning of three coupling fields is studied and obtained that interchange, splitting and shifting of the transparency and absorption peaks can be achieved by tuning the coupling fields parameters. The obtained results are explained using dressed and doubly dressed-state approach. The three coupling fields in this IY^{+}-system provides a larger degree of freedom to manipulate the spectral feature in the desired manner and obtained results find applications in multi-channel optical communication and optical switching devices.

5.2 Outlook

The studies carried out in this thesis have shown interesting results which find applications in several places. As has been shown in chapter 2, the EIA signal observed with standing wave coupling beam has steeper slope at higher coupling beam power. Such steeper signal can be preferred for laser frequency locking due to its higher stability and performance. Another steeper slope has also been observed in the central EIT signal among three EIT peaks in the presence of the magnetic field at higher coupling beam power. The control of spacing between these three EIT peaks depending on strength of the applied magnetic field as well as steeper central EIT peak offers locking of a laser frequency at a frequency detuning controlled by the magnetic field. Thus, the signals obtained with standing wave coupling beam as well as with travelling wave coupling beam in presence of magnetic field can be use for precise frequency locking in the laoboratories.

The theoretical prediction made in chapter 4 about probe spectral features of a modified inverted-Y system are yet to be realized experimentally. This can be done by employing

D_1, D_2 lines and higher states of ^{87}Rb atoms. The signals of the modified inverted-Y system can be used in technologies like optical switching as well as multi-channel optical communications in near future.

SUMMARY

The thesis work is based on experimental and theoretical studies of electromagnetically induced transparency (EIT) in different atomic systems. Initially, the EIT in two Λ-systems in D_2 line transition of ^{87}Rb atom has been investigated in absence and presence of a longitudinal magnetic field. This experimental study is carried out in a Rb vapor cell at room temperature. The results of two Λ-systems have been compared, where one of the Λ-system has shown more stronger and symmetric EIT signal in the absence of magnetic field and steeper slope of the central EIT peak in the presence of the magnetic field. The prevailed Λ-system is also investigated with standing wave coupling beam where electromagnetically induced absorption (EIA) is observed. This EIA signal exhibits more steeper slope which is more suitable for applications like tight laser frequency locking as compared to the EIT signal.

The study of EIT then progressed in an extension of Λ-system, *i.e.,* N-system. The two N-systems preparaed in D_2 line transition of ^{87}Rb atoms has been investigated in cold atom cloud trapped in a magneto-optical trap (MOT). The N-systems have shown three transmission dips in the probe spectrum. Along with the experimental study, numerical study has also been carried out using density matrix formalism and solving Liouville equation. The parametric dependence study of these N-systems has shown that control field of N-system governs the central transmission dip and coupling field of N-system governs the side transmission dips. The presence of aditional electromagnetic field in the N-system offers a large degree of freedom for control and manipulation of the spectral features.

Subsequently, a theoretical investigation in a more complex structure, i.e. a five-level modified inverted-Y system has been made using a numerical matrix propagation method.

In this study, the interdependence of systems like Λ-, ladder- and vee-systems has been obtained with the variation in parameters of different coupling fields. The obtained results have shown the inter-conversion of absorption and transparency, splitting and shifting of absorption peaks. These obtained spectral features may be useful in optical switching devices involving quantum interference effects.

Chapter 1

Introduction

Electromagnetically induced transparency (EIT) is an interesting effect which occurs due to induced atomic coherence due to an external electromagnetic field and resulting quantum interferences in an atomic system. As the name itself suggests, EIT leads to enhancement in probe transmission in an otherwise opaque medium due to presence of an another electromagnetic field called as coupling field. According to quantum mechanics, whenever there is more than one excitation path for transition, the transition amplitudes for different paths combine to produce quantum interference. When the destructive quantum interference occurs, the suppression of probe absorption leads to enhanced probe transmission, which is EIT.

The concept of EIT was first given by Harris in 1989 [1] and then demonstrated by him and his co-worker in 1990 [2]. Harris et al. [2] had performed the EIT experiment on Strontium vapour using pulse laser and their results revealed that this effect can be seen in the atomic system where atomic coherence is created by coupling field and probe field experiences quantum interference. As the EIT signal is a result of quantum interference, its linewidth can be very narrower than natural linewidth of the excited state [3]. This feature finds applications in the precision spectroscopy, precise atomic clocks [4], high resolution spectroscopy [5, 6, 7], and laser locking [8, 9]. Along with the suppressed absorption,

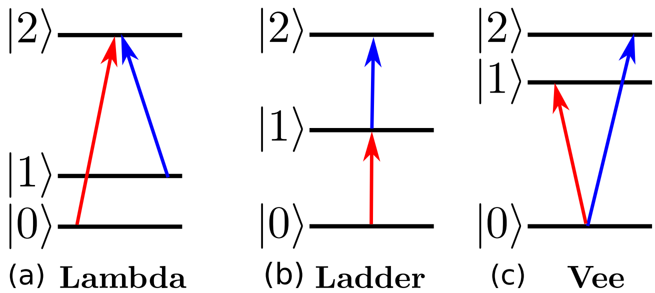

Figure 1.1: (a) Λ system, (b) *ladder* system, and (c) *Vee* system that can exhibit EIT feature in their probe transmission spectrum.

EIT also shows strong dispersive characteristic for refraction. Since the dispersion is inversely related to group velocity of the probe field, higher change in dispersion due to EIT results in the reduction of group velocity of probe field inside the atomic medium. This gives rise to slow light application [10, 11, 12]. Sometimes, group velocity even can be reduced to zero and storage of light is possible to attain [10, 12, 13, 14, 15]. Another interesting feature of EIT effect is that it gives enhanced third-order susceptibility. Thus, EIT provides enhanced non-linearity with least linear absorption in an atomic medium [16, 17, 18, 19, 20, 21, 22].

Atomic systems with multi-EIT window are particularly interesting due to their applications in multi-channel optical communication. The multi-EIT window can be obtained by applying a static magnetic field to the EIT atomic system. The presence of a magnetic field lifts the degeneracy of magnetic sublevels resulting in the formation of multiple EIT peaks in probe transmission spectrum. Another way to generate multiple EIT feature is by applying additional coupling fields connecting more excited states, for example an inverted-Y system [23, 24, 25, 26, 27, 28], or using a bichromatic or polychromatic coupling field [29, 30, 31, 32, 33] in the EIT atomic system. The phenomenon of EIT also has applications in quantum information processing [34, 35], sensitive magnetometry [36, 37, 38, 39, 40, 41], optical communication network [42], optical switching devices [43, 44], etc.

The basic schemes that can exhibit EIT feature are three-level atomic systems interacting with two resonant laser fields. The weaker light field, commonly referred as the 'probe beam' is collected on a detector to observe the effect of the EIT whereas the stronger light field, known as the 'coupling beam', is used to generate the coherence between the associated levels. The three common configurations are Λ [45, 46, 47, 48], *ladder* [49, 50, 51] and *Vee* [52, 53, 54] systems, and their energy levels and transitions are shown in Fig 1.1. A Λ-system is characterized by two ground states and one common excited state through which both the probe and coupling fields interact with the atomic system. In a *ladder* system, one electromagnetic field interacts with ground and intermediate state and another field interacts with intermediate and excited state. When both the probe and coupling fields interact with common ground state but with different excited states, the system formed is known as *Vee* system. Among all the three systems, the Λ-system exhibits minimal coherence dephasing rate of the dipole forbidden transition. This offers higher amplitude of EIT than that in other systems [55]. Hence, Λ-system is a preferable system for investigation and applications of EIT phenomenon.

This thesis deals with the exploration of EIT effect in Λ-system and its extended system formed in D_2 line transition of ^{87}Rb atom. The thesis work contains both experimental as well as theoretical studies on EIT phenomenon. The study begins with Λ-system at room temperature, where EIT in two possible Λ-systems has been compared in order to obtain stronger and symmetric EIT signal. The prevailed Λ system has been further investigated in different conditions. The obtained results may find applications in tight laser frequency locking [8, 9] and optical switching devices [43, 56]. This work is presented in chapter 2 of this thesis. The thesis work then proceeded with an extension of Λ-system, *i.e.* N system where an interesting dual like structure of EIT has been observed. The N-system has been investigated in cold atomic sample of ^{87}Rb atoms trapped in a magneto-optical trap. The cold atom offers reduced Doppler effect as well as relatively low collisional effect. These studies are presented in chapter 3 of this thesis. Subsequently, the thesis work has been extended to theoretical investigation of a more complicated structure *i.e.* modified inverted-Y system. The obtained results of this system have been discussed in

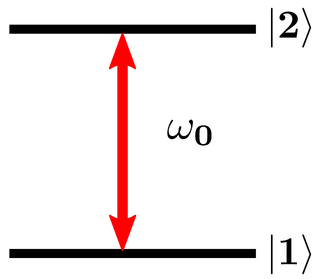

Figure 1.2: A two level atomic system interacting with a probe field of frequency ω.

chapter 4 of this thesis. Finally, chapter 5 describes the conclusion and future scope of the thesis work. The remaining sections of this chapter present general introduction about the subject light-atom interaction and basic mechanisms to cool and trap atoms.

1.1 Theoretical background

In order to understand the underlying physics behind the interaction of electromagnetic field with atom, it is important to obtain the optical response of the medium. We begin with a simplest system *i.e.* two-level system interacting with a probe field.

1.1.1 Two-level atomic system

Consider a two-level atom with ground state $|1\rangle$ and excited state $|2\rangle$ interacting with an electromagnetic field, as shown in Fig 1.2. The energies of states $|1\rangle$ and $|2\rangle$ are $\hbar\omega_1$ and $\hbar\omega_2$ respectively, such that $\omega_2 - \omega_1 = \omega_0$. The atomic Hamiltonian for the two-level atomic system can be written as [57],

$$\mathcal{H}_0 = \hbar\omega_1|1\rangle\langle 1| + \hbar\omega_2|2\rangle\langle 2|, \tag{1.1}$$

such that $\mathcal{H}_0|1\rangle = \hbar\omega_1|1\rangle$ and $\mathcal{H}_0|2\rangle = \hbar\omega_2|2\rangle$. The interaction Hamiltonian due to coupling of the atom with the electromagnetic field $\vec{E} = \vec{E_0}\ cos(\omega t)$ of frequency ω can be written as,

$$\mathcal{H}_I = -\vec{\mu} \cdot \vec{E}, \tag{1.2}$$

where $\vec{\mu}$ is dipole moment operator and $\vec{E}$ is electric field vector. The total Hamiltonian of the system is,

$$\mathcal{H} = \mathcal{H}_0 + \mathcal{H}_I. \tag{1.3}$$

To obtain the dynamics of the system, we need to solve the Schrödinger equation, *i.e.*,

$$i\hbar \frac{\partial |\psi(t)\rangle}{\partial t} = \mathcal{H} |\psi(t)\rangle. \tag{1.4}$$

The wave function ψ as a function of time t can be expressed as linear combinaton of basis states $|1\rangle$ and $|2\rangle$ as,

$$|\psi(t)\rangle = c_1(t) e^{-i\omega_1 t} |1\rangle + c_2(t) e^{-i\omega_2 t} |2\rangle, \tag{1.5}$$

where $c_{1,2}$ are amplitudes and $\hbar\omega_{1,2}$ are energy of atomic states $|1\rangle$ and $|2\rangle$ respectively. On substituting equation (1.5) in equation (1.4), we obtain two coupled differential equations for coefficient c_1 and c_2 as,

$$i\hbar \dot{c_1} = c_2 \langle 1|\mu \cdot E|2\rangle e^{-i\omega_0 t} \tag{1.6}$$

$$i\hbar \dot{c_2} = c_1 \langle 2|\mu \cdot E|1\rangle e^{i\omega_0 t}, \tag{1.7}$$

where $\hbar\omega_0 = \hbar\omega_2 - \hbar\omega_1$. With definition $\Omega = \frac{\langle 1|\vec{\mu}\cdot\vec{E}|2\rangle}{\hbar}$, above two equations can be written as,

$$i\dot{c_1} = c_2\Omega(\frac{e^{i(\omega-\omega_0)t} + e^{-i(\omega+\omega_0)t}}{2}) \quad (1.8)$$

$$i\dot{c_2} = c_1\Omega^*(\frac{e^{i(\omega+\omega_0)t} + e^{-i(\omega-\omega_0)t}}{2}), \quad (1.9)$$

At this stage, rotating-wave approximation(RWA) can be made where the terms like $e^{\pm i(\omega+\omega_0)t}$ are ignored. These terms oscillates with twice the frequency of interacting field and averages to zero soon. After applying RWA and defining the detuning as $\Delta = \omega - \omega_0$, the coupled equations can be written as,

$$i\dot{c_1} = c_2\Omega\frac{e^{i\Delta t}}{2} \quad (1.10)$$

$$i\dot{c_2} = c_1\Omega^*\frac{e^{-i\Delta t}}{2}, \quad (1.11)$$

On differentiating above two equations again, we obtained coupled equations as,

$$\ddot{c_1} - i\Delta\dot{c_1} + \frac{\Omega^2}{4}c_1 = 0 \quad (1.12)$$

$$\ddot{c_2} + i\Delta\dot{c_2} + \frac{\Omega^2}{4}c_2 = 0. \quad (1.13)$$

Initially, when there is no electromagnetic field, all the atoms remain in ground state $|1\rangle$. Thus, using initial conditions $c_1(0) = 1$ and $c_2(0) = 0$, the probabilty of population in excited state at time t is calculated and expressed as,

$$|c_2|^2 = |\frac{\Omega}{\Omega'}|^2 sin^2\Big(\frac{\Omega' t}{2}\Big), \quad (1.14)$$

where $\Omega' = \sqrt{\Delta^2 + \Omega^2}$. For the case of resonant electromagnetic field interacting with two-level atom, the above obtained equation shows that atom undergoes an oscillation between two atomic state with a frequency Ω, which is known as Rabi frequency.

1.1.2 Density Matrix Formalism

The atomic system interacting with the electromagnetic field also experiences spontaneous emission which is a dissipative process in the system. The other dissipative process like collisional effect can also be present in the system. In such case, the evolution of the system should be described in term of density matrix operator (ρ) rather than a state vector ($|\psi\rangle$). The density operator for a quantum system may be expressed as,

$$\rho = \sum_{i=1}^{2} p_i |\psi_i\rangle\langle\psi_j|, \tag{1.15}$$

where system is likely to be found in the state $|\psi_i\rangle$ with probabilty p_i. The diagonal (ρ_{ii}) and off-diagonal density matrix elements ($\rho_{ij}; i \neq j$) show the population in the atomic state $|\psi_i\rangle$ and coherence between the states $|\psi_i\rangle$ and $|\psi_j\rangle$, respectively. The dynamics of the atomic system in terms of density matrix are governed by the Heisenberg equation which can be expressed as,

$$\dot{\rho} = -\frac{i}{\hbar}[\mathcal{H}, \rho]. \tag{1.16}$$

Under rotating-wave approximation (RWA), the Hamiltonian for two-level atom interacting with an electromagnetic field of frequency ω and Rabi frequency Ω can be written in matrix form in the basis set of atomic states $|1\rangle$ and $|2\rangle$ as (derivation is in Appendix A),

$$\mathcal{H} = -\frac{\hbar}{2}\begin{bmatrix} 2\Delta & \Omega \\ \Omega^* & 0 \end{bmatrix}, \tag{1.17}$$

where Δ is detuning of the electromagnetic field, defined as $\Delta = \omega_0 - \omega$. The time evolution of the atomic system can be obtained using Hamiltonian from equation (1.17) in equation (1.16). The elements of time evolution density matrix, in general, can be expressed as,

$$\dot{\rho_{ij}} = -\frac{i}{\hbar}[\sum_k (\mathcal{H}_{ik}\rho_{kj} - \rho_{ik}\mathcal{H}_{kj})], \tag{1.18}$$

where $\mathcal{H}_{ik}$ is matrix element of the Hamiltonian in equation (1.17) and ρ_{ik} is density matrix element, with i and $k \in \{1, 2\}$. Using $\mathcal{H}_{ik}$ from equation (1.17) in equation (1.18), the following set of differential equations are obtained as,

$$\dot{\rho_{11}} = -i(\Omega^* \rho_{12} - \Omega\rho_{21}) \tag{1.19}$$

$$\dot{\rho_{22}} = i(\Omega\rho_{12} - \Omega^* \rho_{21}) \tag{1.20}$$

$$\dot{\rho_{21}} = -i\Delta\rho_{21} + i\Omega^*(\rho_{11} - \rho_{22}). \tag{1.21}$$

The time evolution of population in states due to spontaneous emission decay depends on the decay rate of excited state (Γ) as,

$$\left(\frac{d}{dt}\rho_{22}\right)_{sp} = \left(-\frac{d}{dt}\rho_{11}\right)_{sp} = -\Gamma\rho_{22} \tag{1.22}$$

and the evolution of coherence depending on Γ [58] is

$$\left(\frac{d}{dt}\rho_{21}\right)_{sp} = \left(\frac{d}{dt}\rho_{12}\right)_{sp} = -\frac{\Gamma}{2}\rho_{21}. \tag{1.23}$$

Incorporating the above decay terms for populations and coherence, the newly formed equations of motion are,

$$\dot{\rho_{11}} = -\frac{i}{2}(\Omega^*\rho_{12} - \Omega\,\rho_{21}) + \Gamma\rho_{22} \tag{1.24}$$

$$\dot{\rho_{22}} = \frac{i}{2}(\Omega\,\rho_{12} - \Omega^*\rho_{21}) - \Gamma\rho_{22} \tag{1.25}$$

$$\dot{\rho_{21}} = -(i\Delta + \Gamma/2)\rho_{21} + \frac{i}{2}\Omega^*(\rho_{11} - \rho_{22}). \tag{1.26}$$

1.1.3 Relation between microscopic and macroscopic properties

The external electromagnetic field induces dipole moment in the atom resulting in the polarization of the atom. The polarization ($\vec{P}$) of the atomic medium is defined as dipole moment per unit volume and is expressed as,

$$\begin{aligned}\vec{P} &= n\,\langle\vec{\mu}\rangle = nTr(\vec{\rho}\,\vec{\mu})\\ &= n\,(\vec{\mu_{12}}\,\tilde{\rho_{21}}\,e^{-i\omega t} + \vec{\mu_{21}}\,\tilde{\rho_{12}}\,e^{i\omega t}),\end{aligned} \tag{1.27}$$

where n is number of atoms per unit volume and μ_{ij} $(i, j\epsilon\{1, 2\})$ is induced dipole moment. Also, the polarization of the medium is related to the electric field by

$$\vec{P} = \epsilon_0\,\chi(\omega)\vec{E} = \frac{1}{2}\,\epsilon_0\,\vec{E_0}\,(\chi\,e^{-i\omega t} + \chi^*\,e^{i\omega t}), \tag{1.28}$$

where ϵ_0 is the permittivity of free space, $\chi(\omega)$ is known as susceptibility of the medium, and E_0 is the strength of the electromagnetic field. The susceptibility is complex in nature where its real part gives dispersion of the medium and imaginary part describes the absorption of electric field inside the medium. From equations (1.27) and (1.28), the relation between susceptibility (χ, which is a macroscopic property) and the induced dipole moment of the atom (μ_{21}, which is a microscopic property) can be obtained as,

$$\chi(\omega) = \frac{2\, n\, |\vec{\mu_{21}}|^2 \tilde{\rho_{12}}}{\hbar\, \epsilon_0\, \Omega^*}. \tag{1.29}$$

In practice, though two-level system does not exist, a closed transition between two states of any atom can be approximated to a two-level atomic system. Such system can be used to understand the principle of laser cooling via radiation force, which is discussed in section 1.3.

1.2 Three-level Λ-system

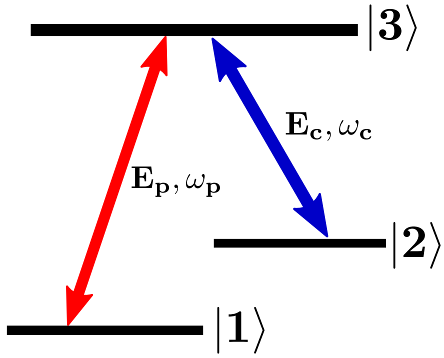

Figure 1.3: A three level Λ system interacting with a probe and a strong coupling field shown by red and blue arrow respectively.

To obtain a theoretical description of EIT, a three-level Λ-system is considered where an excited state $|3\rangle$ is coupled with ground states $|1\rangle$ and $|2\rangle$ via a weak probe field with amplitude E_p and frequency ω_p, and a strong coupling field with amplitude E_c and frequency ω_c, respectively. The coupling between states $|1\rangle$ and $|2\rangle$ is dipole forbidden. The Λ-system is shown in Fig 1.3.

1.2.1 Derivation of Hamiltonian

The total Hamiltonian of the Λ-system can be expressed in matrix form in the basis of ground states $|1\rangle$, $|2\rangle$ and excited state $|3\rangle$ as,

$$\mathcal{H} = \begin{pmatrix} \hbar\omega_1 & 0 & -\mu_{13}E \\ 0 & \hbar\omega_2 & -\mu_{23}E \\ -\mu_{31}E & -\mu_{32}E & \hbar\omega_3 \end{pmatrix}, \tag{1.30}$$

where μ_{ij} is the element of dipole moment and E is the total electric field in the medium. The total electric field E is defined as,

$$\begin{aligned} E &= E_p cos(\omega_p t) + E_c cos(\omega_c t) \\ E &= \frac{E_p}{2}(e^{i\omega_p t} + e^{-i\omega_p t}) + \frac{E_c}{2}(e^{i\omega_c t} + e^{-i\omega_c t}). \end{aligned} \tag{1.31}$$

For simplicity of calculation, the Hamiltonian should be transformed to interaction picture using a time evolution operator $U(t)$, such that

$$U(t) = e^{i\mathcal{H}_0 t/\hbar} = \begin{bmatrix} e^{i\omega_1 t} & 0 & 0 \\ 0 & e^{i\omega_2 t} & 0 \\ 0 & 0 & e^{i\omega_3 t} \end{bmatrix}, \tag{1.32}$$

where $\mathcal{H}_0$ is the unperturbed Hamiltonian of the system. The transformation of Hamiltonian can be obtained as,

$$U\mathcal{H}U^{+} = \begin{bmatrix} \hbar\omega_1 & 0 & -\mu_{13}Ee^{i(\omega_1-\omega_3)t} \\ 0 & \hbar\omega_2 & -\mu_{23}Ee^{i(\omega_2-\omega_3)t} \\ -\mu_{31}Ee^{-i(\omega_1-\omega_3)t} & -\mu_{32}Ee^{-i(\omega_2-\omega_3)t} & \hbar\omega_3 \end{bmatrix}. \tag{1.33}$$

On using equation (1.31) in the above transformed Hamiltonian, we obtain two exponential terms for each non-zero diagonal elements. for example,

$$(U\mathcal{H}U^{+})_{13} = -\mu_{13}E_p(e^{i(\omega_1-\omega_3-\omega_p)t} + e^{i(\omega_1-\omega_3+\omega_p)t}).$$

Assuming the electromagnetic field is near resonant to the transition frequency, the terms like $e^{i(\omega_1-\omega_3-\omega_p)t}$ oscillate with twice the frequency of electromagnetic field and gets average out to zero quickly. We drop such terms from all the transformed elements and this approximation is known as rotating wave approximation (RWA). The transformed Hamiltonian after RWA is,

$$\mathcal{H}' = U\mathcal{H}U^{+} = \frac{1}{2}\begin{bmatrix} 2\hbar\omega_1 & 0 & -\mu_{13}E_p e^{i(\omega_1-\omega_3+\omega_p)t} \\ 0 & 2\hbar\omega_2 & -\mu_{23}E_c e^{i(\omega_2-\omega_3+\omega_c)t} \\ -\mu_{31}E_p e^{-i(\omega_1-\omega_3+\omega_p)t} & -\mu_{32}E_c e^{-i(\omega_2-\omega_3+\omega_c)t} & 2\hbar\omega_3 \end{bmatrix}. \tag{1.34}$$

This Hamiltonian is in interaction picture. We again transfer this Hamiltonian into Schrödinger picture with definition $\Omega_p = \frac{E_p|\mu_{13}|}{\hbar}$ and $\Omega_c = \frac{E_c|\mu_{23}|}{\hbar}$, as

$$\mathcal{H} = U^{+}\mathcal{H}'U = \frac{\hbar}{2}\begin{bmatrix} 2\omega_1 & 0 & -\Omega_p e^{i\omega_p t} \\ 0 & 2\omega_2 & -\Omega_c e^{i\omega_c t} \\ -\Omega_p^* e^{-i\omega_p t} & -\Omega_c^* e^{-i\omega_c t} & 2\omega_3 \end{bmatrix}. \tag{1.35}$$

In order to remove the time dependence, the Hamiltonian needs to be transformed in corotating frame and the new basis is known as rotating basis. The new basis is related to old basis by $|\tilde{n}\rangle = \tilde{U}(t)|n\rangle$.

The unitary matrix $\tilde{U}$ which can transform the Hamiltonian is,

$$\tilde{U(t)} = \begin{bmatrix} e^{-i\omega_p t} & 0 & 0 \\ 0 & e^{-i\omega_c t} & 0 \\ 0 & 0 & 1 \end{bmatrix}. \tag{1.36}$$

The Hamiltonian in corotating frame should satisfy the Schrödinger equation, *i.e.,*

$$\begin{aligned} \tilde{\mathcal{H}}|\tilde{n}\rangle &= i\hbar\frac{\partial}{\partial t}|\tilde{n}\rangle \\ &= i\hbar\frac{\partial}{\partial t}(\tilde{U}|n\rangle) \\ &= i\hbar(\frac{\partial\tilde{U}}{\partial t}|n\rangle + \tilde{U}\frac{\partial|n\rangle}{\partial t}) \\ &= i\hbar(\frac{\partial\tilde{U}}{\partial t}|n\rangle + \frac{-i}{\hbar}\tilde{U}\mathcal{H}|n\rangle) \\ \tilde{\mathcal{H}}|\tilde{n}\rangle &= (i\hbar\frac{\partial\tilde{U}}{\partial t}\tilde{U}^\dagger + \tilde{U}\mathcal{H}\tilde{U}^\dagger)\tilde{U}|n\rangle. \end{aligned} \tag{1.37}$$

Using unitary matrix $\tilde{U}$ from equation (1.36) and Hamiltonian from equation (1.35) in equation (1.37), we obtain

$$\tilde{\mathcal{H}} = \frac{\hbar}{2}\begin{bmatrix} 2(\omega_1 + \omega_p) & 0 & -\Omega_p \\ 0 & 2(\omega_2 + \omega_c) & -\Omega_c \\ -\Omega_p^* & -\Omega_c^* & 2\omega_3 \end{bmatrix}. \tag{1.38}$$

One can add multiple of identity to the Hamiltonian $\tilde{\mathcal{H}}$ without changing any physical results. With addition of $-2\omega_3 I$, we obtain the Hamiltonian for three-level Λ-system in terms of detuning of fields ($\Delta_p = \omega_3 - \omega_1 - \omega_p$ and $\Delta_c = \omega_3 - \omega_2 - \omega_c$) as,

$$\tilde{\mathcal{H}} = -\frac{\hbar}{2}\begin{bmatrix} 2\Delta_p & 0 & \Omega_p \\ 0 & 2\Delta_c & \Omega_c \\ \Omega_p^* & \Omega_c^* & 0 \end{bmatrix}. \tag{1.39}$$

1.2.2 Optical response

Susceptibility χ is the optical response of an atomic medium to the applied electromagnteic field. In order to obtain the dynamics of the atomic system, χ should be obtained by solving the Heisenberg equation,

$$\dot{\rho} = -\frac{i}{\hbar}[\mathcal{H}, \rho]. \tag{1.40}$$

To account dissipation of the system, the relaxation terms can be added phenomenologically and assuming $\Omega_{p,c}$ as a real parameter, the optical Bloch equations are obtained from equation (1.40) and equation (1.39) as following,

$$\begin{aligned}
\dot{\rho_{11}} &= \frac{i}{2}\Omega_p(\rho_{31} - \rho_{13}) + \Gamma_1\rho_{33} \\
\dot{\rho_{22}} &= \frac{i}{2}\Omega_c(\rho_{32} - \rho_{23}) + \Gamma_2\rho_{33} \\
\dot{\rho_{33}} &= \frac{i}{2}\Omega_p(\rho_{13} - \rho_{31}) + \frac{i}{2}\Omega_c(\rho_{23} - \rho_{32}) - \Gamma\rho_{33} \\
\dot{\rho_{13}} &= [i\Delta_p + \Gamma/2]\rho_{13} + \frac{i}{2}\Omega_p(\rho_{33} - \rho_{11}) - \frac{i}{2}\Omega_c\rho_{12} \\
\dot{\rho_{12}} &= [i(\Delta_p - \Delta_c) + \gamma]\rho_{12} + \frac{i}{2}\Omega_p\rho_{32} - \frac{i}{2}\Omega_c\rho_{13} \\
\dot{\rho_{23}} &= [i\Delta_c + \Gamma/2]\rho_{23} - \frac{i}{2}\Omega_p\rho_{21} + \frac{i}{2}\Omega_c(\rho_{33} - \rho_{22}).
\end{aligned} \tag{1.41}$$

In above equations, $\Gamma = \frac{1}{2}(\Gamma_1 + \Gamma_2)$, where $\Gamma_{1,2}$ is decay rate from excited state $|3\rangle$ to ground states $|1\rangle$ and $|2\rangle$, respectively, and γ is dephasing decay. The optical response of the medium is defined by susceptibility (χ) and is depends on optical coherence ρ_{13}. The ρ_{13} can be obtained by solving above equations in steady state condition as (derivation is

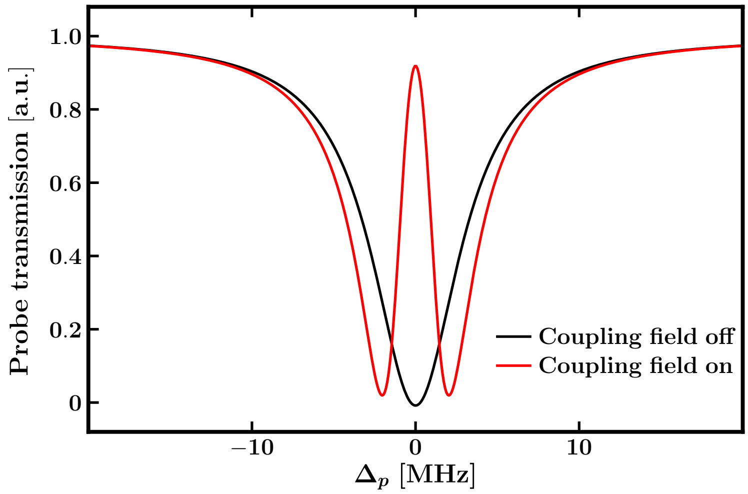

Figure 1.4: The probe transmission as a function of probe field detuning Δ_p. The black curve shows the probe transmission in absence of coupling field ($\Omega_c = 0$) and red curve shows the probe transmission in presence of coupling field ($\Omega_c = 2\pi \times 4$MHz). The EIT feature is depicted in red curve by enhanced transmission at zero detuning of probe field.

presented in Appendix B (B.9)),

$$\rho_{13} = \frac{i\Omega_p/2}{(i\Delta_p + \Gamma/2) + \frac{\Omega_c^2}{4[i(\Delta_p - \Delta_c) + \gamma]}}. \tag{1.42}$$

Recalling the relation between susceptibility and density matrix element from equation (1.29) and using ρ_{13} from equation (1.42), we get

$$\chi(\omega) = \frac{2\, n\, |\mu_{13}|^2}{\hbar\, \epsilon_0\, \Omega_p} \frac{2i\Omega_p\, [i(\Delta_p - \Delta_c) + \gamma]}{4(i\Delta_p + \Gamma/2)\, [i(\Delta_p - \Delta_c) + \gamma] + \Omega_c^2}. \tag{1.43}$$

In real experiment, the optical response of the medium can be seen from probe transmission spectrum. The probe transmission depends on absorption coefficient α which is defined as $\alpha = kIm(\chi(\omega))$ and the probe transmission is

$$T = \exp\{-\alpha l\}, \tag{1.44}$$

where l is length of the atomic medium. Using equation (1.43) and (1.44), the probe transmission as a function of probe field detuning is plotted in Fig 1.4 with parameters $n = 1.2 \times 10^9\ cm^{-3}$, $l = 1mm$, $\Gamma = 2\pi \times 6$ MHz, $\gamma = 2\pi \times 0.1$ MHz, $\Omega_p = 2\pi \times 1$ MHz. When the coupling field is off, *i.e.* $\Omega_c = 0$, the probe transmission is shown by black curve which shows transmission dip at resonance which means the atomic medium absorbs photons from probe field. Whereas, a peculiar behaviour can be seen in presence of coupling field shown by red curve in the figure ($\Omega_c = 2\pi \times 4$MHz), *i.e.* the probe transmission enhances at resonance. This enhanced transmission is the EIT feature in the spectrum.

1.3 Laser cooling and trapping of atoms

The cooling of atom provides a great medium for study of EIT. The cold atoms eliminate the Doppler effect and reduce the collisional dephasing rate effectively. The basic mechanisms to cool the atoms are discussed in this section.

1.3.1 Doppler cooling and optical molasses

A simplest way to reduce the temperature of atoms is by providing a frictional force to the moving atoms. This can be achieved through the Doppler cooling mechanism. In this mechanism, the frictional force is generated due to transfer of momentum of the absorbed photon to the atom in the direction opposite to the atomic motion. This purpose can be served by a red detuned laser beam counter-propagating with respect to the atomic motion because the Doppler shifted frequency of counter-propagating beam becomes resonant to the atomic frequency. Whereas, the co-propagating beam becomes more red-detuned from atomic resonance frequency in atomic frame of reference. Thus, the atom absorbs photon from the counter-propagating laser beam and gets excited. With the absorption of photon, the atom gains a momentum kick in the direction opposite to its motion and gets

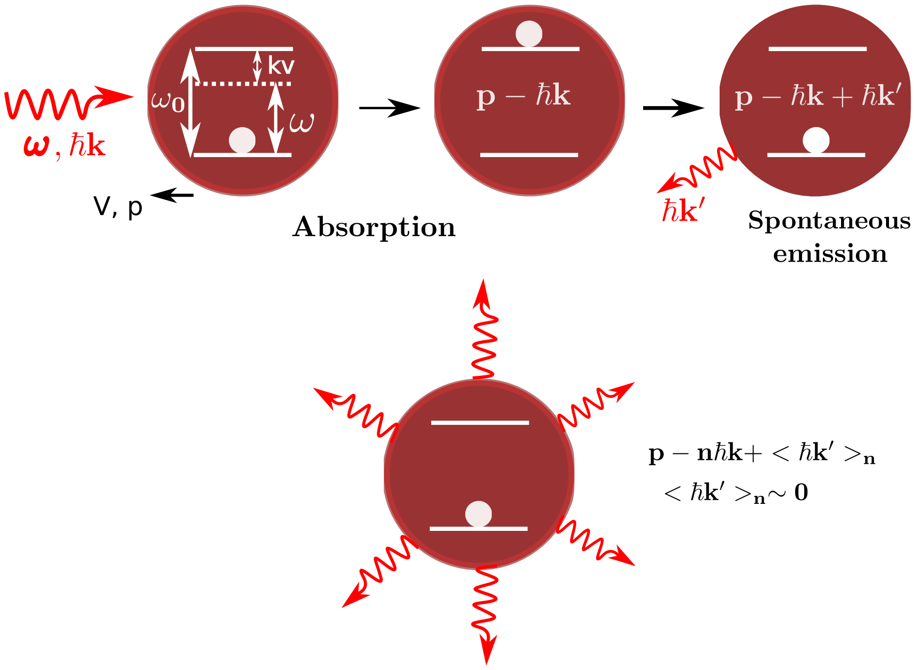

Figure 1.5: Schematic diagram of the Doppler cooling mechanism. The dotted line depicts frequency of laser beam (ω) which is red detuned from atomic transition frequency (ω_0). Due to Doppler effect, counter-propagating laser beam becomes resonant to atomic transition frequency and hence atom absorb and spontaneously emit photon on interaction with this laser beam.

slow down. Also, during spontaneous emission, the atom again gains a momentum kick but in random direction. Under many cycles of absorption and emission of photons, *i.e.* scattering of photons, the momentum kick in random direction due to the spontaneous emission averages out to zero. At the end, the resultant momentum kick received by the atom is due to the absorption of photons. This results in slow down of the atomic motion. The schematic of absorption and emission process is shown in Fig 1.5.

The radiation force exerted on the atom in the scattering process is defined as rate of change of momentum,

$$F_{scatt} = \hbar k \gamma_{sc}, \tag{1.45}$$

where $\hbar\ k$ is momentum of photon with $\hbar$ to be Plank's constant and k is wave vector of the laser beam, and γ_{sc} is the photon scattering rate, [59]

$$\gamma_{sc} = \frac{\Gamma}{2}\frac{I/I_s}{1 + \frac{I}{I_s} + (\frac{2\delta}{\Gamma})^2}. \tag{1.46}$$

Here, Γ is decay rate of the excited state, I is intensity of the laser beam, I_s is the saturation intensity and δ is detuning of laser frequency.

For the case, when an atom is placed between two counter-propagating red-detuned laser beams, the total force exerted on the atom with velocity v due to two beams can be obtained as [60],

$$\begin{aligned} F &= F^{+}_{scatt} - F^{-}_{scatt} && (1.47)\\ F &= \hbar k\frac{\Gamma}{2}\Big(\frac{I/I_s}{1 + \frac{I}{I_s} + (\frac{2(\delta-kv)}{\Gamma})^2} - \frac{I/I_s}{1 + \frac{I}{I_s} + (\frac{2(\delta+kv)}{\Gamma})^2}\Big). && (1.48)\end{aligned}$$

Assuming the case $kv << \Gamma$, scattering force can be approximated as,

$$F \approx -\frac{I}{I_s}\frac{\delta}{\Gamma}\frac{8\hbar k^2}{(1 + \frac{I}{I_s} + (\frac{2\delta}{\Gamma})^2)^2}v. \tag{1.49}$$

The above obtained force can be expressed as $F = -\beta v$ with $\beta = 8\hbar k^2 \frac{I}{I_s}\frac{\delta/\Gamma}{[1+I/I_s+(2\delta/\Gamma)^2]^2}$. This force is a frictional force and is responsible to slow down the atom in one dimension. To extend this cooling mechanism in three dimension, three pairs of counter-propagating red detuned laser beams can be used from three orthogonal directions. This arrangement is also known as optical molasses.

In this mechanism, there exist fluctuation in the absorption of photons followed by its spontaneous emission in a particular period of time. Thus, the random kick due to spontaneous emission does not completely average out to zero and causes a limitation in the cooling temperature. This limited temperature is called Doppler cooling limit and given by [61]

$$T_D = \frac{\hbar\Gamma}{2K_B}, \tag{1.50}$$

where, K_B is Boltzmann constant and Γ is atomic linewidth which is $2\pi\times$ 6 MHz for ^{87}Rb atom. According to this limit, the minimum temperature that can be achieved by Doppler cooling method for ^{87}Rb is 140 μK. But in the real life experiments, the temperature below the Doppler limit has been obtained. This can be explained by sub-Doppler cooling mechanism discussed in the next subsection 1.3.2.

1.3.2 Sub-Doppler cooling

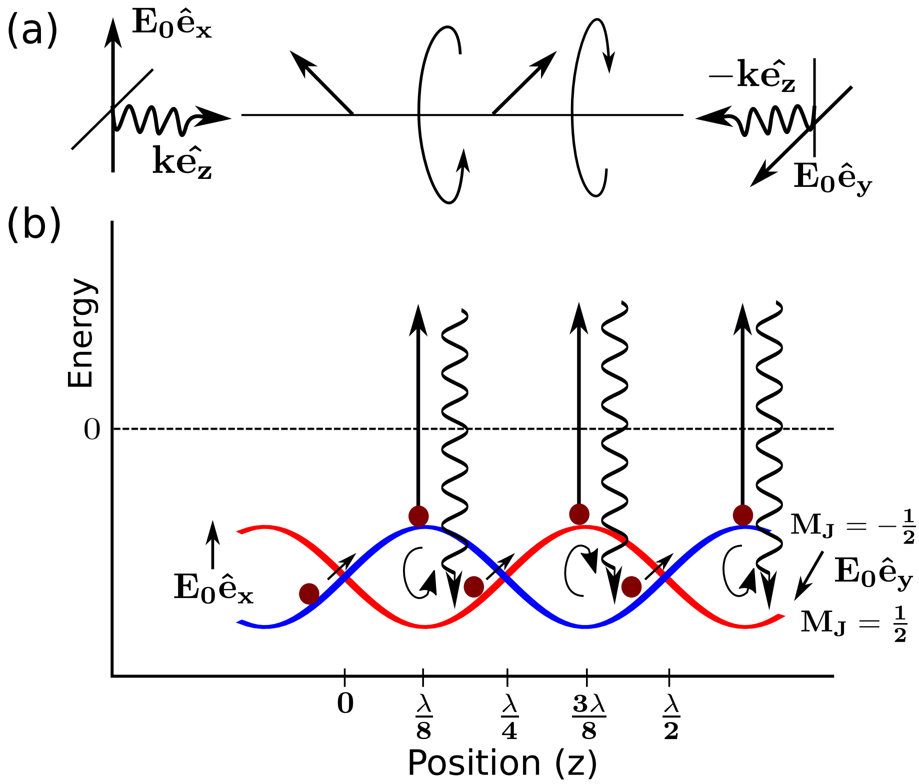

Figure 1.6: (a) Formation of polarization gradient due to superimpose of two orthogonally linearly polarized counter-propagating laser beams, (b) The periodic modulation of light shift energy of ground states due to polarization gradient. The atom follows the light shift energy and optically pumped from hill of one gorund state to valley of another ground state. During optical pumping, the atom radiates away its potential energy.

The key role in the sub-Doppler cooling mechanism is played by multiple levels of real atom, polarization gradient, light shift and spatially dependent optical pumping. The way this mechanism allows to reach ultra low temperature can be understood as follows.

Refer diagram in Fig 1.6, and consider an atom with ground state angular momentum $J = 1/2$ and excited state angular momentum $J = 3/2$ is placed in a pair of counter-propagating laser beams with same frequency (ω_L) and mutually orthogonal linear polarization. On assuming the propagation of beams in z-direction, the resulting electric field can be expressed as,

$$\begin{aligned} \epsilon &= \epsilon_0[\hat{x}cos(\omega_L t - kz) + \hat{y}cos(\omega_L t + kz)] \\ &= \epsilon_0[(\hat{x} + \hat{y})cos(\omega_L t)cos(kz) + (\hat{x} - \hat{y})sin(\omega_L t)sin(kz)]. \end{aligned} \tag{1.51}$$

Due to interference, the polarization of the resulting superimposed laser beam varies with space, which can be obtained from the equation (1.51). At $z = 0$, the resulting electric field is ,

$$\epsilon = \epsilon_0(\hat{x} + \hat{y})cos(\omega_L t), \tag{1.52}$$

and polarization is linear with angle $\pi/4$ with respect to x-axis. Similarly, we can obtain the polarizations of the resulting electric field at other positions also. This polarization gradient is shown in Fig 1.6 (a).

Whenever near resonant field interacts with atom, the light shift of energy of the atomic states occur. The light shift depends on the Clebsch-Gordan (CG) coefficient which is different for different magnetic sublevels and is also a function of the polarization of the interacting field. Thus, due to polarization gradient, there exists periodic modulation of the light shift of each sublevels. Now, suppose at position $z = \lambda/8$, where polarization is σ^+, the atom with velocity v is in state $m_J = 1/2$ and follows the light shift of the atomic state, *i.e.* it climbs up a potential hill. When it reaches to the position $z = 3\lambda/8$, *i.e.* where the polarization is σ^- , the atom is at top of the hill and is optically pumped to the valley of another ground state $m_J = -1/2$ via absorption and spontaneous emission. Again, atom follows the light shift and climbs the potential hill. During climbing up the potential hill, the potential energy of the atom increases but kinetic energy decreases and overall energy of the atom remains constant. When the atom undergoes one absorption and spontaneous emission, due to larger frequency of the spontaneous emission than that of absorption, the atom looses its potential energy which in turn results in a reduction of kinetic energy. In this way, for each travel length of $\lambda/4$, the atom looses its kinetic energy and hence the temperature is lowered. The schematic of this mechanism is shown in Fig 1.6 (b). The process of absorption and spontaneous emission continues as atom moves, and keeps on loosing energy. However, the temperature through this mechanism can not go down indefinetly. The limitation in temperature is the recoil temperature *i.e.* $T_R = \hbar^2 k^2/2M$.

1.3.3 Magneto-optical trap

The mechanisms discussed in previous sub-sections reduce the temperature of the atoms but fails to maintain the atoms in the interaction zone of the laser beams for cooling due to lack of a trapping mechanism. In order to trap the atoms at the center, a position dependent force is required. Whereas, for cooling purposes, a velocity dependent force is needed. The configuration that can cool as well as trap the atoms is known as Magneo-optical trap (MOT). In this technique, a spatially varying force is exerted by laser beams in presence of an inhomogeneous magnetic field.

To understand the basic principle of cooling and trapping in the MOT, consider an atom with ground state angular momentum $J = 0$ and excited state angular momentum $J = 1$, moving in z-direction. The inhomogeneous magnetic field is applied to the atom by using a pair of anti-helmholtz coil, where magnetic field at the center of two coils (*i.e.* $z = 0$) is zero and it varies linearly with space away from the center. As the magnetic field is

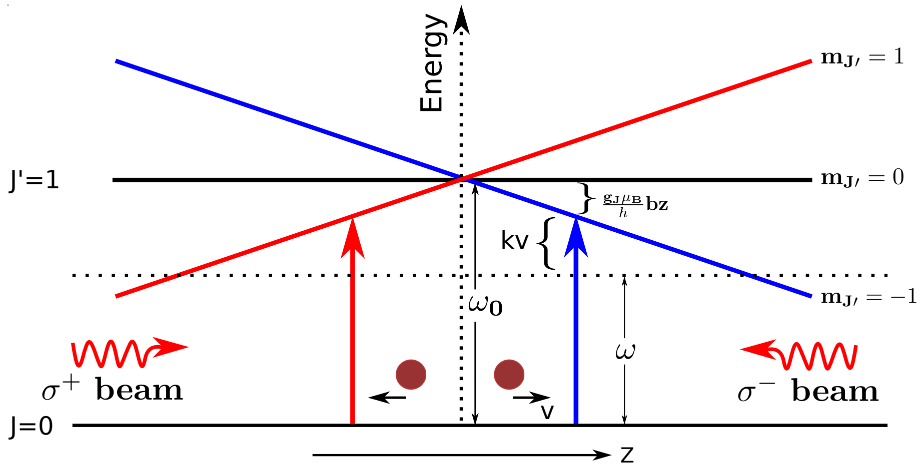

Figure 1.7: Schematic diagram of one dimensional magneto-optical trap. The two counter-propagating laser beams with orthogonal circular polarization are of frequency ω which is red detuned from atomic transition frequency ω_0. Due to inhomogeneous magnetic field, excited Zeeman sublevels varies linearly with space (z). The effective detuning of laser beams become function of atomic velocity v as well as position z. From both the sides of $z = 0$, atom experiences a push towards $z = 0$. In this way, atom remains trapped at the center.

linearly dependent on spatial coordinates ($B(z) = bz = \frac{dB}{dz} \cdot z$), the energy of excited Zeeman sub levels also shifts depending on the spatial position of the atom, *i.e.* $\frac{g_J \mu_B}{\hbar} bz$, as shown in Fig 1.7. The Zeeman sub-level $m_J = +1$ is closer to ground state for $z < 0$ and $m_J = -1$ is closer to ground state for $z > 0$. The two counter-propagating red detuned laser beams with orthogonal circular polarizations (σ^+ and σ^-) are allowed to incident on the atom. When the atom moves in positive z-direction, the Doppler shifted frequency of counter-propagating σ^- laser beam at particular position ($\omega + kv$) becomes resonant to the frequency of atomic transition $m_J = 0$ to $m_J = -1$, *i.e.* $\omega_0 - \frac{g_J \mu_B}{\hbar} bz$. The σ^- laser beam gives a push to the atom towards the center ($z = 0$) with the same principal as of Doppler cooling. Similarly when the atom moves in negative z-direction, the Doppler shifted frequency of counter-propagating σ^+ laser beam at particular position becomes resonant to the atomic transition $m_J = 0$ to $m_J = +1$ and gives a push to the atom opposite to its motion. In this way, the atom is forced to remain at the center. In this technique, the effective detuning of beams depend on both velocity and position of the atom due to Doppler shift (kv) and Zeeman shift ($\alpha = g_J m_J \mu_B \frac{dB}{dz}$) as $\delta_{\pm} = \delta \mp k \cdot v \mp \alpha z$. The total force exerted on the atom in the MOT can be obtained as [61],

$$F_{MOT} = F^{\sigma^+}_{scatt} - F^{\sigma^-}_{scatt} \tag{1.53}$$
$$= \hbar k \frac{\Gamma}{2}\Big(\frac{I/I_s}{1+\frac{I}{I_s}+(\frac{2(\delta-kv-\alpha z)}{\Gamma})^2} - \frac{I/I_s}{1+\frac{I}{I_s}+(\frac{2(\delta+kv+\alpha z)}{\Gamma})^2}\Big). \tag{1.54}$$

With assumption that the Zeeman shift and the Doppler shift is very small, the above equation can be approximated as

$$F_{MOT} = -\beta v - \eta z, \tag{1.55}$$

where, β is same as defined in section 1.3.1 and $\eta = \alpha/k\beta$. The coefficient of v in equation (1.55) shows dissipative force and coefficient of z in the same equation shows restoring force which trap the atoms. In real experiments, the MOT is realized in three dimension by applying three pairs of counter-propagating laser beams. The MOT is the most common tool to trap and cool neutral atoms.

1.4 Rubidium structure

As this thesis covers all the studies in Rubidium atomic medium, the atomic structure of Rubidium and some related information is discussed in this section. Rubidium, symbolizes as Rb, is an element that belongs to alkali group of periodic table. It has 37 atomic number and has two isotopes with mass number 85 and 87. The natural Rb is composed of 72 % ^{85}Rb and 28 % ^{87}Rb. As being an alkali metal, Rb is highly reactive and gets oxidized in air. In our study, the choosen atomic medium is Rb gas as the wavelength of laser required for transition in this medium is easily available and also the energy levels of Rb allows the formation of Λ system for EIT experiment with least perturbation due to

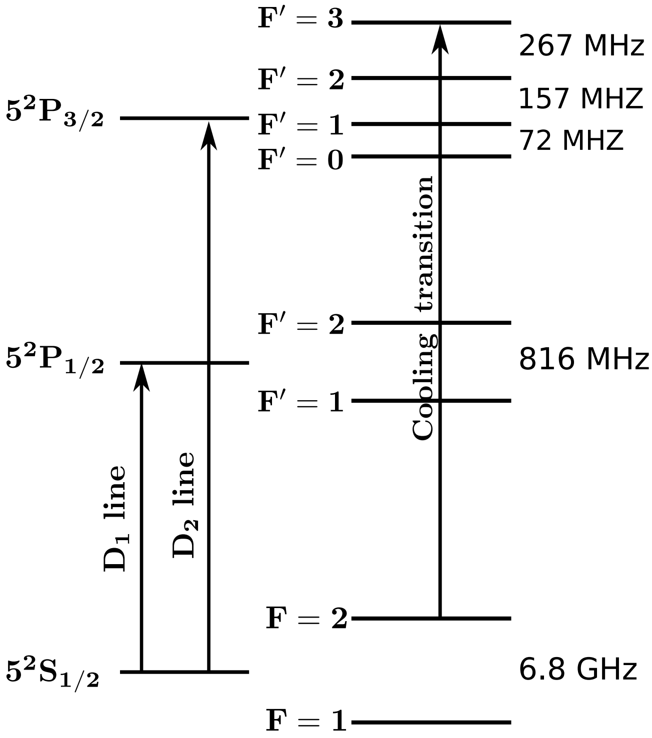

Figure 1.8: Energy level diagram of ^{87}Rb atom showing fine and hyperfine structure.

highly separated excited hyperfine states. Rb gas is special in science field as its ground state hyperfine splitting are used in high precision frequency measurement and also in atomic clock. Not only this, but Rb is also a major contender for generating cold atomic cloud.

From Pauli′s exclusion principles, a single electron of Rb atom exist in valence orbital 5S. The orbital angular momentum L of Rb atom interacts with its spin angular momentum S and give total electronic angular momentum $J = L + S$. This interaction perturbs the energy levels of the Rb atom and give rise to fine structure, where excited state 5P splits into two states with quantum number $j = 1/2$ and $3/2$. The transition from ground state to these two excited states are termed as D line transition i.e. D_1 line for transition $5^2S_{1/2} \rightarrow 5^2P_{1/2}$ with wavelength 795 nm, and D_2 line for transition $5^2S_{1/2} \rightarrow 5^2P_{3/2}$ with wavelength 780 nm. The total electronic angular momentum J also interacts with nuclear spin I and result in emergence of hyperfine structure. The hyperfine levels F range from $|J - I|$ to $|J + I|$.

As this thesis deals with ^{87}Rb atoms, we discuss here only hyperfine structure of ^{87}Rb atom. The nuclear spin of ^{87}Rb atom is $3/2$, therefore for $J = 1/2$, $F = 1, 2$. For $J = 3/2$, $F = 0, 1, 2, 3$. The energy level diagram of ^{87}Rb atom is shown in Fig 1.8. The cooling transition can be easily obtained in D_2 line transition of ^{87}Rb atom. Due to availability of laser systems, the EIT work has also been carried out in D_2 line transition of ^{87}Rb atom. Also, the closely spaced excited hyperfine state of D_2 line transition allows to study the effect of neighbouring levels in EIT signal.

Chapter 2

Electromagnetically induced transparency in Λ-system in Rb vapor cell

2.1 Introduction

In this chapter, a study of electromagnetically induced transparency in two Λ-systems in D_2 line transition of ^{87}Rb atom in vapor cell has been presented. A vapor cell is an useful medium to study light-atom interaction due to availability of large interaction regime between atoms and laser beams. The vapor cell is easy to handle and also cost effective. In a typical Rb-vapor cell, having natural rubidium atoms, the constituent isotopes are 72% of ^{85}Rb and 28% of ^{87}Rb. In vapor cell, at room temperature, non-zero velocity class of atoms reduces the line-width of EIT via thermal avergaing [62], which offers a very narrow EIT peak in a transmitted probe signal [63]. On the other side, the thermal motion of atoms at room temperature leads to Doppler broadening which is larger than the hyperfine splitting of the excited state of Rubidium. This can mask the EIT feature in probe transmission spectrum. To reduce Doppler effect in Λ-system, probe and coupling beams should propagate collinearly in same direction through the atomic medium. In such case, two-photon resonance condition reduces the Doppler effect and narrow EIT feature can be obtained in the probe transmission spetrum.

This chapter begins with the description of EIT experiment in Rb vapor cell and then results of the study are discussed. The studied two Λ-systems in D_2 line transition of ^{87}Rb atom differ from each other in respect of their different neighbouring energy levels of the excited state and different Clebsch-Gordan coefficient for coupling transition. In this regard, a comparative study of EIT in two Λ-systems at room temperature is established in this chapter. A narrow line-width and significant strength of EIT is required to be obtained, as such signal finds a place for very significant applications like slow-light propagation [10, 12], high resolution spectroscopy [6, 7] and laser frequency locking [8]. The dependence of EIT features on physical parameters is the way to obtain stronger and narrower EIT signal to be useful for proper application. In this respect the EIT feature with the variation in strength of coupling field and magnetic field has been investigated. One of the two Λ- systems has shown more stronger EIT signal than that of other Λ- system at different conditions. The investigation of EIT feature with standing wave coupling beam is further carried out in the prevailed Λ- system.

2.2 Experimental Realization

In order to experimentally realize the Λ-system, two different external cavity diode lasers (ECDLs) were used. One of the ECDLs (TA-Pro TOPTICA, Germany) with $1/e^2$ radii $\sim$ 1.36 mm was used to derive probe beam and another ECDL (DL-100, TOPTICA, Germany) with $1/e^2$ radii $\sim$ 2.04 mm was used to derive strong coupling beam. Both the lasers were operated at 780 nm wavelength with spectral line-width less than 1 MHz. The two Λ-systems, hereafter referred as system (A) and (B) and are shown in Fig 2.1, were generated using a fixed frequency for probe beam and a scanned frequency of coupling

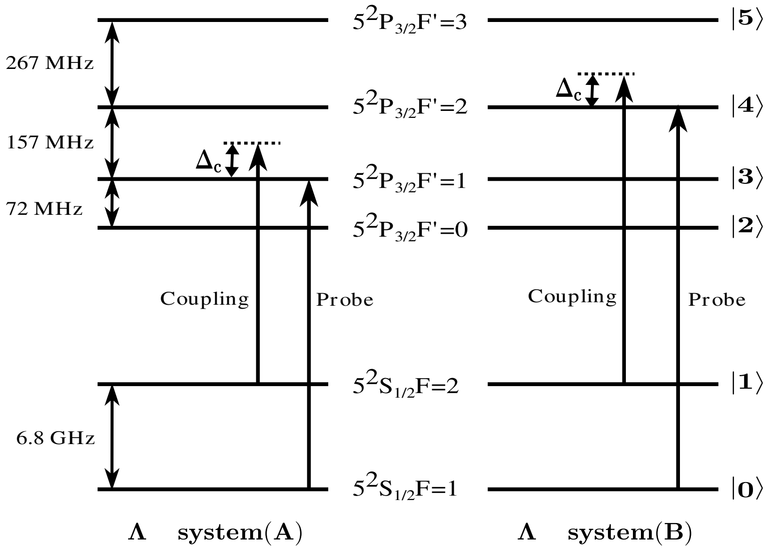

Figure 2.1: The studied Λ systems formed in D_2 line transition of ^{87}Rb, with Δ_c as the detuning of the coupling beam from corresponding resonance transition frequencies.

beam. The probe beam frequency was fixed so that the effect of coupling beam can be seen over a flat probe transmission signal due to resonant frequency of the probe beam. This offers easier detection of small changes in the probe signal due to coupling beam effect. For system (A) and (B), the fixed frequencies of the probe beams were corresponding to the transition $|5^2S_{1/2}F = 1\rangle \rightarrow |5^2P_{3/2}F' = 1\rangle$ and $|5^2S_{1/2}F = 1\rangle \rightarrow |5^2P_{3/2}F' = 2\rangle$ respectively. For both systems, the coupling beam was scanned across the transitions $|5^2S_{1/2}F = 2\rangle \rightarrow |5^2P_{3/2}F' = 1, 2, 3\rangle$. The frequencies of lasers were referenced to a given transition using saturated absorption spectroscopy (SAS) technique [64, 65, 66, 67].

The schematic diagram of the experimental setup is shown in Fig 2.2. A weak part of each of the probe and coupling beams was used for SAS and remaining part of both of these beams were used for EIT experiments. A co-propagating configuration of both the probe and coupling beams were prepared and made them pass through a 50 mm long Rb vapor cell in order to reduce the Doppler effect [68]. The pressure inside the vapor cell is $\sim 3.6 \times 10^{-7}$ Torr and number density of Rb atoms is $\sim 1.2 \times 10^{10}$ cm^{-3}. A long current carrying solenoid was wrapped over the Rb vapor cell for the purpose of generating longitudinal magnetic field inside the cell for measurements in presence of magnetic

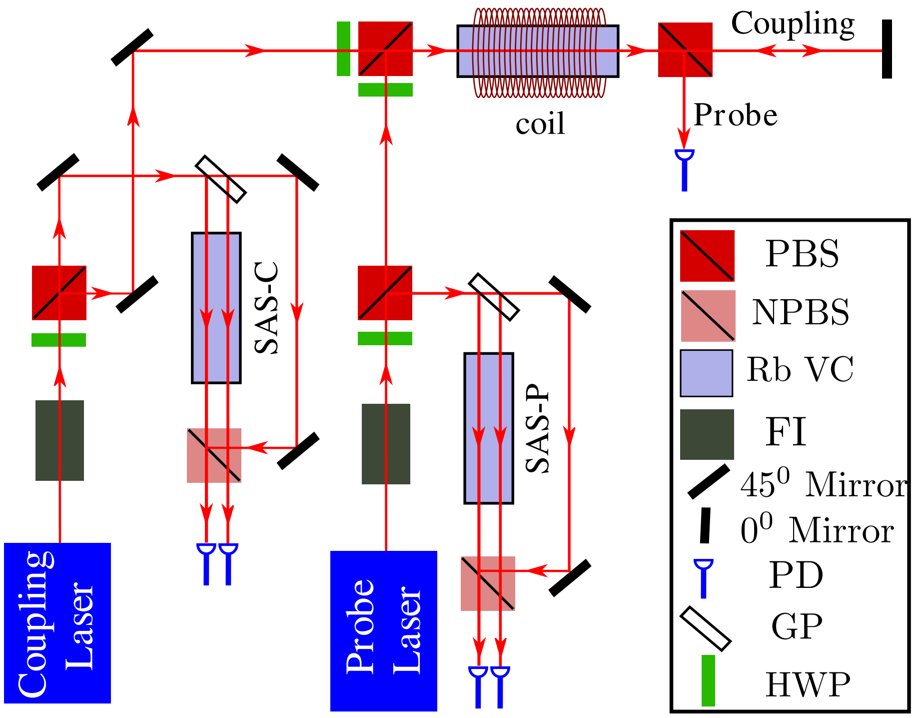

Figure 2.2: Schematic diagram of the experimental setup. GP: glass plate; FI: Faraday isolator; NPBS: non-polarising beam splitter; PBS: polarising beam splitter; HWP: half-wave plate; RbVC: Rubidium vapor cell; PD: photodiode; SAS-P: saturated absorption spectroscopy for probe beam and SAS-C: saturated absorption spectroscopy for coupling beam.

field. By keeping the solenoid length much longer than the vapor cell length, the homogeneity of the applied magnetic field was maintained. To avoid the stray magnetic field, the Rb vapor cell wrapped with coil were kept inside two layers of μ-metal sheet. For experiment with standing wave coupling beam, a zero degree mirror was kept after polarizing beam splitter to retro-reflect the transmitted co-propagating coupling beam which produces standing wave inside the Rb vapor cell. Using a half-waveplate (HWP) and a polarizing beam splitter (PBS), the power in the probe and coupling beams (P_p and P_c, respectively) were controlled (Fig 2.2). In this study, P_c indicates the power of the coupling beam in co-propagating direction. The polarizations of two beams were kept linear but mutually orthogonal to each other so that after traversing the Rb vapor cell, the probe beam can be separated out using polarizing beam splitter. The transmitted probe beam was collected on photo-diode and the transmitted probe signal was measured on an oscilloscope connected with the photodiode.

2.3 Results and Discussion

The comparison of EIT observations in two Λ-systems for various external parameters and the comparison of EIT signal at different conditions has been made from application point of view in this section. During the measurements, the power of the probe beam (P_p) was kept fixed at 0.08 mW while the other parameters were varied as per requirement of the experiment. The strength of the beam is defined by Rabi frequency (Ω) which can be expressed in terms of beam intensity I, saturation intensity $I_{sat} = \frac{c\epsilon_0\Gamma^2\hbar^2}{4d^2}$, and natural line width Γ ($2\pi \times 6$ MHz) as,

$$\Omega = \Gamma\sqrt{\frac{I}{2I_{sat}}}. \tag{2.1}$$

In the expression of saturation intensity I_{sat}, d is the atomic dipole moment which is $d = \mu_{ij}\mu_0$, where $\mu_0 = 3.58\times10^{-29}$ C-m for D_2 line transition of ^{87}Rb atom and μ_{ij} is dipole transition matrix element between states i and j. Here, c is speed of light ($c = 3 \times 10^8$ m/s), ϵ_0 is vacuum permittivity ($\epsilon_0 = 8.85 \times 10^{-12}$ F/m) and $\hbar$ is reduced Planck's constant ($\hbar = 1.05 \times 10^{-34}$ J-s). As saturation intensity depends on dipole moment, its value is different for different transitions. For example, for transitions $F = 1 \rightarrow F' = 1, 2$ and $F = 2 \rightarrow F' = 2$, $I_{sat} = 2.0\ mW/cm^2$. For transition $F = 2 \rightarrow F' = 1$, $I_{sat} = 10.0\ mW/cm^2$. Since μ_{ij} values for probe beam transition in two Λ-systems are same, therefore probe beam strength for same probe power in two systems are also same. However, the strength of the coupling beam in two systems for same power (P_c) is different because of the difference in μ_{ij} for coupling transitions in two systems.

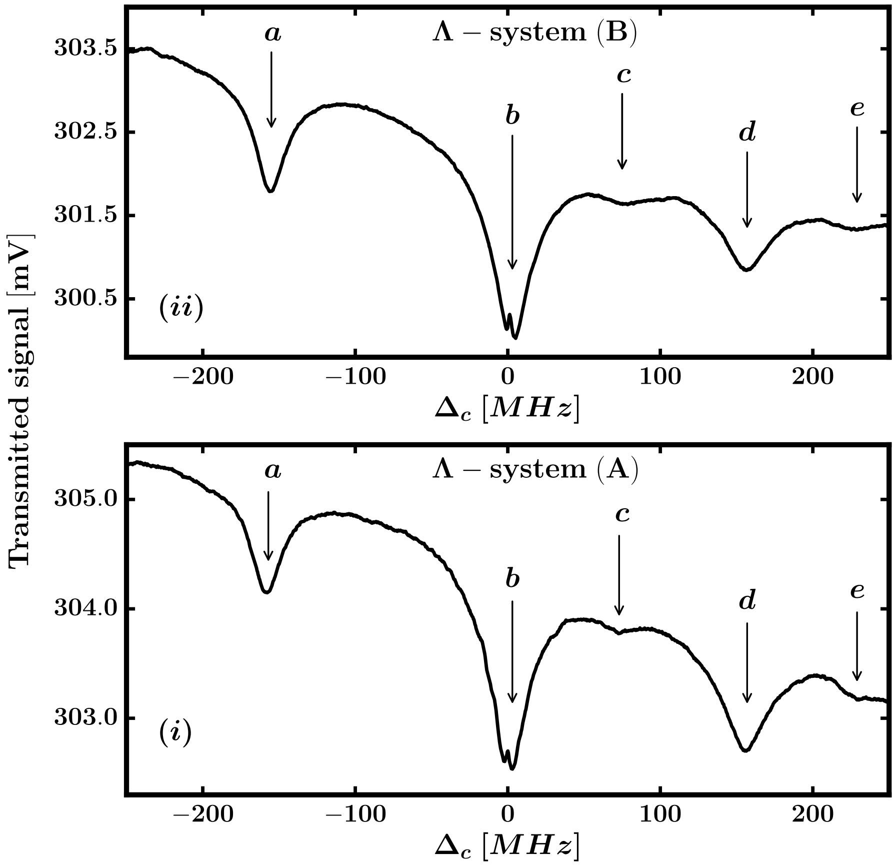

Figure 2.3: The transmitted probe signal as a function of coupling beam detuning. The velocity selective optical pumping (VSOP) absorption dips are labelled by a-e. EIT signal is observed in dip b at zero detuning of coupling beam where two photon resonance condition is satisfied. The probe power and the coupling beam power is P_p = 0.08 mW and P_c = 1 mW respectively.

Five absorption dips (a-e), spectral features which are also known as velocity selective optical pumping (VSOP) dips [69, 70, 71, 72, 73], have been observed for both the Λ-systems in the recorded probe transmission signal which is shown in Fig 2.3. The fulfilment of the two photon resonance condition at zero coupling beam detuning (*i.e.,* in dip 'b') results in a narrow EIT peak in the probe transmission spectrum. The effect of external parameters such as coupling beams strength and magnetic field strength on the EIT signal has been further studied, and results are discussed below.

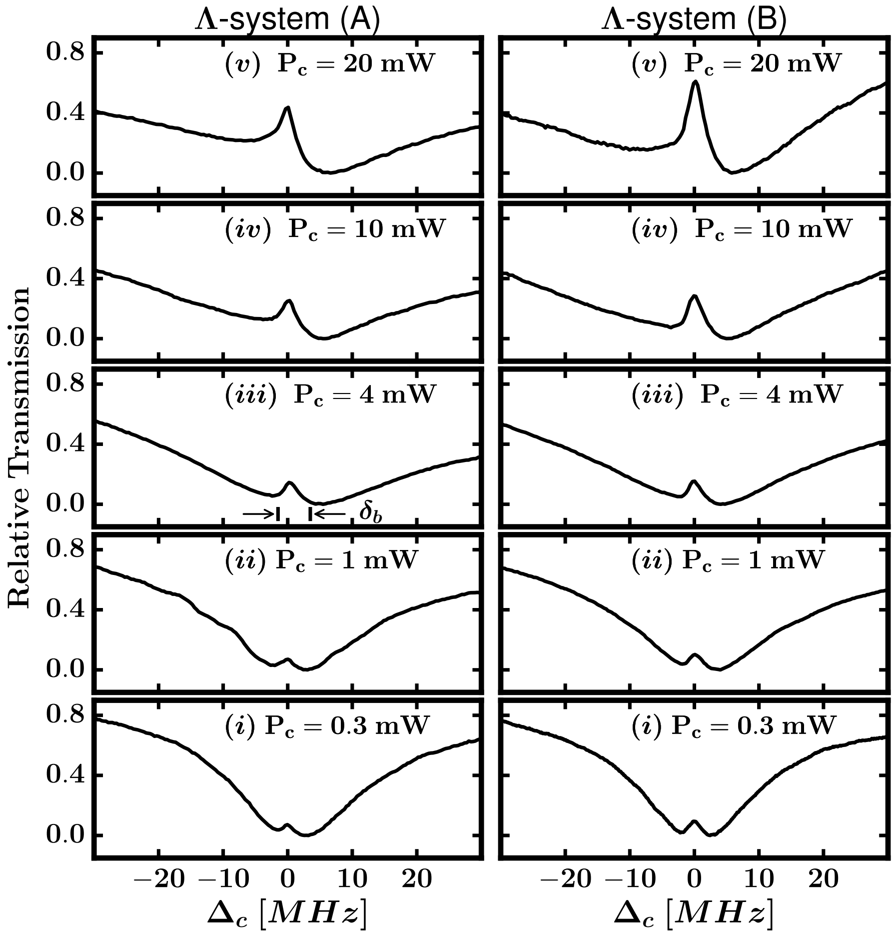

Figure 2.4: The relative probe transmission spectrum for both the Λ-systems (A) and (B) at different values of the coupling beam power, while keeping the probe beam power fixed at 0.08 mW. δ_b shown in figure is the separation between minima of the EIT peak.

2.3.1 Dependence of EIT on coupling beam power

To discern the effect of coupling beam power on the EIT feature in both the Λ-systems, the power of the coupling beam P_c was varied from 0.3 mW to 20 mW. From equation (2.1), the variation in the strength of the coupling beam for system (A) was from $\Omega_c = 2\pi \times 1.9$ MHz to $\Omega_c = 2\pi \times 15.5$ MHz, and for system (B) was from $\Omega_c = 2\pi \times 4.2$ MHz to $\Omega_c = 2\pi \times 34.7$ MHz. The measured relative probe transmissions for different coupling power are shown in Fig 2.4. The relative transmission in Fig. 2.4 is taken as ratio of the signal height from minimum of velocity selective optical pumping absorption (VSOP) dip to the total depth of the same VSOP dip. This transmission scale can directly indicate

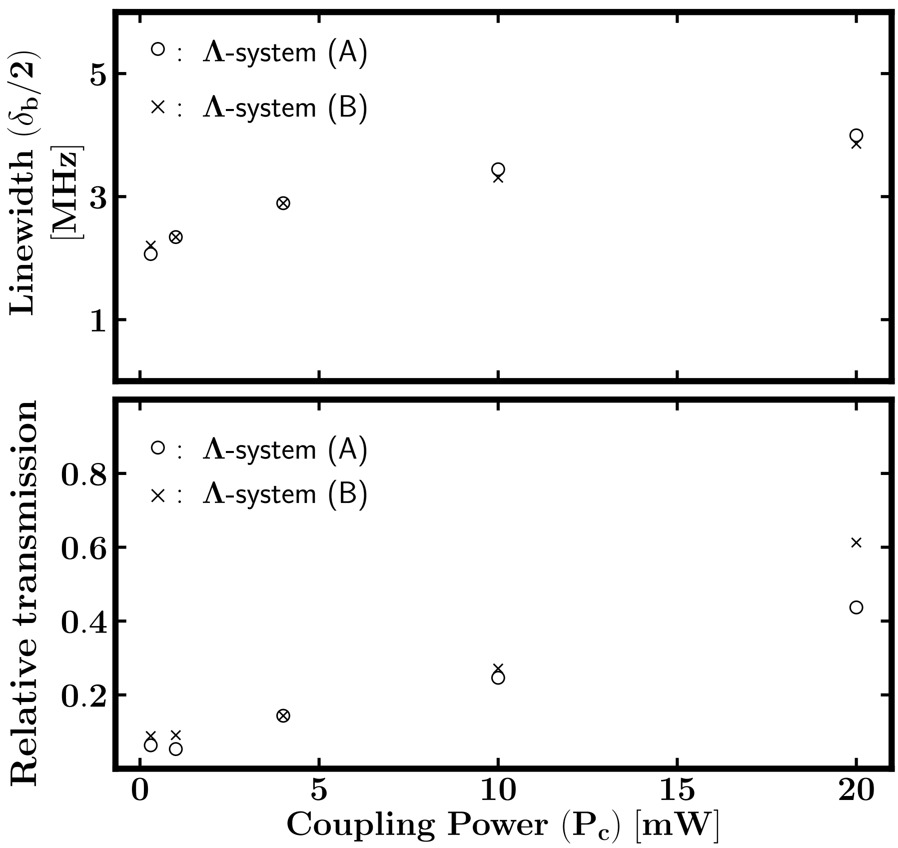

Figure 2.5: (a) The line-width of EIT signal as a function of coupling beam power. (b) The relative probe transmission for zero coupling beam detuning as a function of coupling beam power. The circle and cross marks in both the plots correspond to the Λ-system (A) and Λ-system (B) respectively.

the transmission recovery due to EIT effect in presence of VSOP absorption. The relative transmission (T_R) is written as $T_R = \frac{T - T_{VSOP}}{1 - T_{VSOP}}$, where T is measured transmission and T_{VSOP} is the minimum transmission at VSOP dip.

The effect of coupling beam power has been observed on the line-width, strength and lineshape of the EIT signal. With the increase in the coupling beam power, both the systems have shown increase in the line-width, strength and asymmetry in lineshape of the EIT signal. The strength refers to peak amplitude of EIT signal and asymmetry refers to difference in two minima values both sides of an EIT peak in the signal. In general, the line-width is defined as the full width at half maximum (FWHM) of the signal, but since the observed EIT signal is asymmetric in lineshape, it is difficult to measure the FWHM of the EIT signal. Therefore, for this case, half of δ_b could be considered as FWHM or line-width of the observed EIT signal. δ_b is defined as separation between two minima surrounding the EIT peak. The variation of linewidth of the EIT signal and relative transmission at zero coupling beam detuning as a function of coupling beam power for two systems is shown in Fig 2.5. The important feature in this study is observation of sub-natural linewidth even at higher coupling beam power for both the systems.

On comparing the EIT feature in two systems, the EIT signal for system (A) has shown more asymmetric lineshape than that in system (B). This asymmetry may be because of presence of neighbouring excited states [74, 75] which are more closer in case of system (A). The system (B) has shown stronger strength of EIT signal than that in system (A) for same coupling power. This is because of higher strength of coupling beam in system (B) due to its larger dipole matrix element μ_{ij}. Though the line-width of the EIT signal increases as the coupling power increases, for same power of coupling beam the line-width is nearly same for both the systems. Overall, system (B) exhibits stronger and more symmetric EIT signal than the system (A), which evince that system (B) could be a better choice for any EIT application purposes.

The experimentally observed results are also modelled theoretically considering all the hyperfine levels of D_2 line transition of ^{87}Rb atom. In Fig 2.1, the two possible six-level Λ-systems are shown, where two ground states are labelled as state $|0\rangle$ and $|1\rangle$, and rest of the excited states are labelled as state $|2\rangle$, $|3\rangle$, $|4\rangle$ and $|5\rangle$. The transitions involved in two Λ-systems (A) and (B) are $|0\rangle \rightarrow |3\rangle \leftarrow |1\rangle$ and $|0\rangle \rightarrow |4\rangle \leftarrow |1\rangle$ respectively. The Hamiltonian for the six-level Λ-system (B) interacting with the probe and coupling fields can be constructed after rotating-wave approximation as,

$$H = \begin{bmatrix} \Delta_p - kv & 0 & \Omega_p^{02} & \Omega_p^{03} & \Omega_p^{04} & 0 \\ 0 & \Delta_c - kv & 0 & \Omega_c^{13} & \Omega_c^{14} & \Omega_c^{15} \\ \Omega_p^{20} & 0 & -2\delta_{42} & 0 & 0 & 0 \\ \Omega_p^{30} & \Omega_c^{31} & 0 & -2\delta_{43} & 0 & 0 \\ \Omega_p^{40} & \Omega_c^{41} & 0 & 0 & 0 & 0 \\ 0 & \Omega_c^{51} & 0 & 0 & 0 & 2\delta_{45} \end{bmatrix}, \tag{2.2}$$

where Δ_p and Δ_c are the probe and coupling fields frequency detunings respectively. $\Omega_{p,c}^{ij}$ is the Rabi frequency for the transitions between states $|i\rangle$ and $|j\rangle$ with p and c showing the transitions of probe and coupling fields. δ_{ij} represents the energy separation between the states $|i\rangle$ and $|j\rangle$. The contribution of atomic and interaction Hamiltonian is considered in diagonal and off-diagonal elements of H. To incorporate the effect of thermal motion, term kv with v as the velocity of an atom and k as the wave vector of the electromagnetic fields is included with the detuning terms. In terms of the density matrix (ρ), the evolution of the atomic system can be obtained by solving the Liouville equation

$$\dot{\rho} = -\frac{i}{\hbar}[H, \rho] + \gamma\rho, \tag{2.3}$$

where $\gamma\rho$ incorporates the effect of the decay in the system. A set of thirty-six time dependent equations are obtained from this equation. From these equations, a steady state solution for density matrix elements was obtained numerically. Total sum of $Im(\rho_{02})$, $Im(\rho_{03})$ and $Im(\rho_{04})$) gives imaginary part of the linear susceptibility $Im(\chi^{(1)})$, which in turn provides the probe transmission. In order to include contributions of all atoms with different velocity, the imaginary part of the susceptibility was averaged over all the velocities using Maxwell Boltzmann velocity distribution ($W(v)$) [76] as,

$$Im(\chi^{(1)}) = \int dv W(v) A \sum_{j=2}^{4} \left(\frac{\mu_{0j}^2 \times Im(\rho_{0j})}{\Omega_p^{0j}} \right), \tag{2.4}$$

where A=$\frac{2n}{\epsilon_0 \hbar}$, ϵ_0 is vacuum permittivity, $\hbar$ is reduced Planck's constant, μ_{0j} is the dipole moment between states $|0\rangle$ and $|j\rangle$ and the number density of ^{87}Rb atoms inside the vapor cell is given by n. The probe beam transmission in the medium is given as,

$$T = \exp[-\alpha l], \tag{2.5}$$

where $\alpha = k\ Im(\chi^{(1)})$ is absorption coefficient, k is the wave vector $(2\pi/\lambda)$ of the electromagnetic field and length of the vapor cell is l. To plot the simulations results, we have used values of parameters n, l, Ω_p, Ω_c, δ_{ij} close to experimental values as given above and in section 2.2.

The results of the simulations are presented in Fig 2.6 for both the Λ-systems. The numerically obtained results have also shown velocity selective optical pumping transmission dips and EIT at resonance similar to experimental observations (Fig 2.3) for both the Λ-systems. With the increase in the coupling beam power, the numerical results have also shown an increment in the EIT signal strength as well as in the asymmetry of the line shape. However, the numerically obtained EIT is less assymetric than the experimentally observed EIT signal. This could be because simulations did not included effect of collisions and finite line width of the probe and coupling beam lasers along with the relaxation of the ground states as well as non-radiative decay of atoms within the hyperfine levels of the excited states. The better agreement between numerical and experimental results can be established by incorporating these effects in the simulations [77, 78, 79]. The numerical results in Fig 2.6 also manifest that for a given coupling power, the EIT strength is higher for system (B) than the EIT strength of the system (A). This is because of the higher strength of the coupling beam for system (B) due to its larger Clebsch Gordan coefficient.

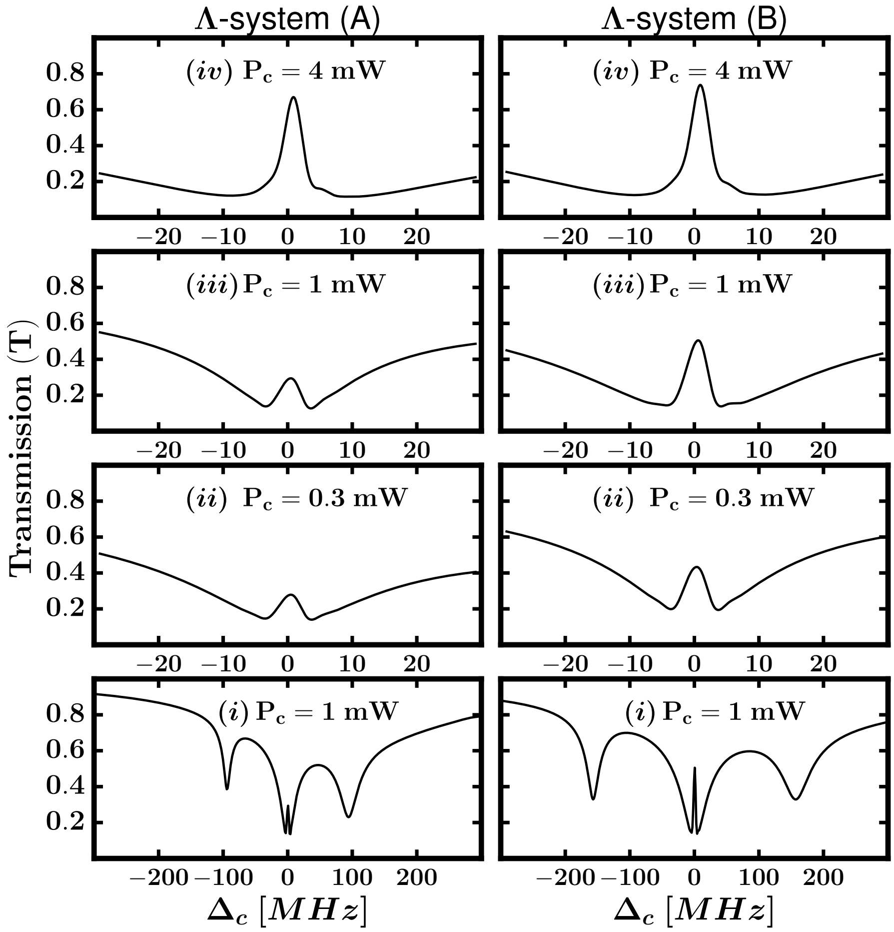

Figure 2.6: The calculated probe transmission spectrum for both the Λ-systems at different powers of coupling beam. Both the VSOP and EIT signals are visible in the probe transmission shown in plot (*i*), whereas a magnified view of the central EIT signal is shown in plots (*ii*) - (*iv*) for various coupling beam powers.

2.3.2 Dependence of EIT on magnetic field strength

The energy levels of an atom are sensitive to magnetic field, these gets split (called as Zeeman splitting) in the presence of magnetic field. The fine narrow resonance feature of EIT is a promising tool to sense these splittings and can be used to build EIT based magnetometer [38]. Also, the removal of degeneracy of Zeeman sublevels in presence of magnetic field distinguishes the two systems (A) and (B) further. Thus, study of dependence of EIT signal on magnetic field and comparison between two Λ-systems in this regard is necessary.

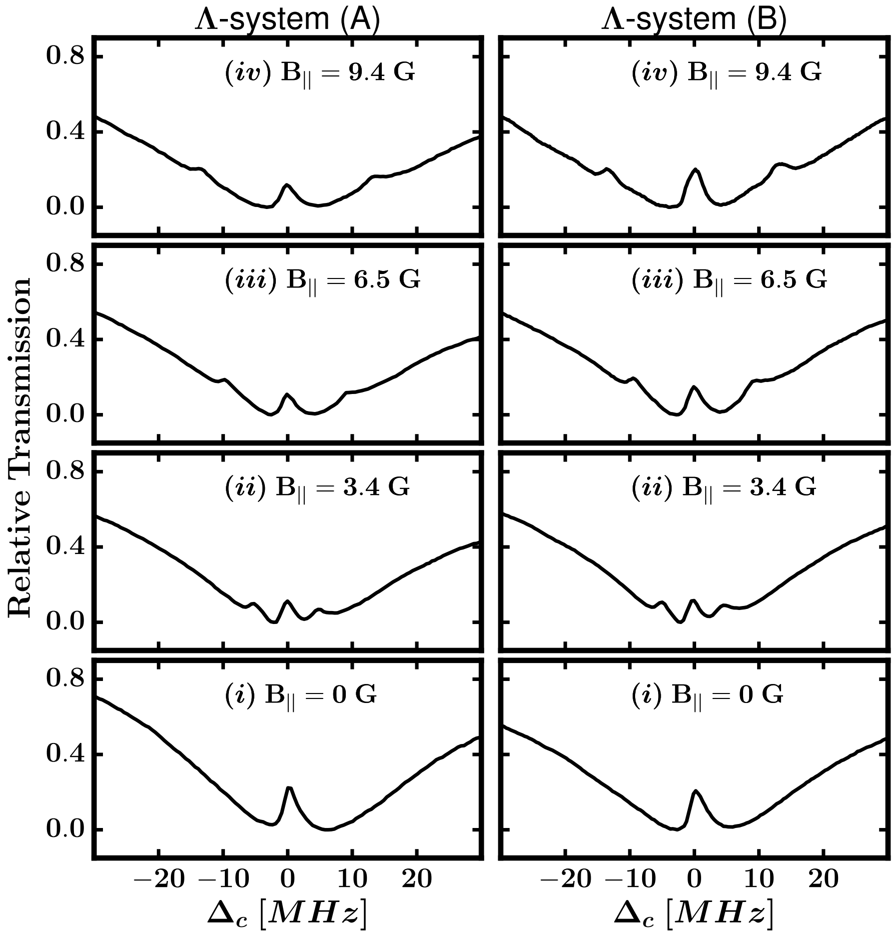

Figure 2.7: The relative probe transmission as a function of coupling beam detuning at different magnetic field strength ($B_{||}$) for both the Λ-systems. The probe beam power is fixed at 0.08 mW and coupling power is fixed at 4 mW.

In the experiments, a longitudinal magnetic field $B_{||}$ is applied by passing current in the circular coil wrapped over the vapor cell. The probe transmission was measured at different magnetic field strengths with the fixed probe beam power P_p =0.08 mW and the coupling beam power P_c =4 mW for both the Λ-systems. The measured relative probe transmissions are shown in Fig 2.7. In the presence of the magnetic field, the EIT signal splits into three peaks for both the systems. The removal of degeneracy of the Zeeman magnetic sublevels (m_F and $m_{F'}$) can be directly held responsible for this splitting of the EIT signal. The frequency separation between two adjacent Zeeman sublevels is given

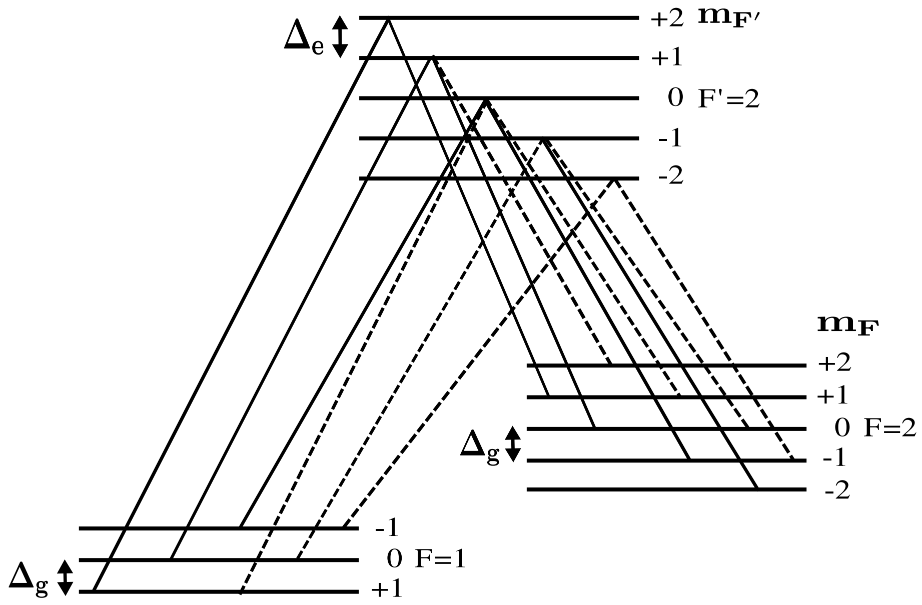

Figure 2.8: Schematic diagram showing different lambda systems resulting from Zeeman splitting of levels in presence of magnetic field. The dashed and continuous lines are for different polarizations (σ^- and σ^+) of light. The Δ_e and Δ_g denote the magnitude of splitting in excited and ground states respectively.

by,

$$\Delta\left(|g_F|, B_{\|}\right) = \frac{|g_F|\mu_B B_{\|}}{h}, \tag{2.6}$$

where μ_B is Bohr magneton and g_F is the hyperfine Landé g-factor.

In the presence of magnetic field, "linearly polarized" probe and coupling beams can be decomposed into two "opposite circularly polarized" beams with σ^+ and σ^- polarizations. These circularly polarized beams couple with different magnetic Zeeman sublevels according to the selection rule $\Delta m_F = \pm 1$. This leads to formation of multiple Λ-subsystems within each Λ-system. According to the two-photon resonance condition, each Λ-subsystem exhibits a EIT signal at the corresponding coupling beam detuning values. Among these Λ-subsystems, the two-photon resonance condition for few of them are degenerate which leads to only three unique coupling beam detunings where EIT signals can be emerged. This can be explained as following.

The separation between the magnetic sublevels of the ground and excited states, denoted as Δ_g (*i.e.* $\Delta(|g_F| = 1/2)$) and Δ_e (*i.e.* $\Delta(|g_F| = 2/3)$) respectively, are different due to the different values of Lande g-factors associated with these states (*i.e.* g_F values). The pictorial representation is shown in Fig 2.8. When we consider a Λ-subsystem of system (B) formed with transitions $(F = 1, m_F = 1) \rightarrow (F' = 2, m_{F'} = 2) \leftarrow (F = 2, m_F = 1)$, the probe and coupling beam detunings can be written as $\Delta_p = \Delta_g + 2\Delta_e$ and $\Delta_c = -\Delta_g + 2\Delta_e$ respectively, where Δ_e and Δ_g are excited and ground state splitting values. The two-photon resonance condition ($\Delta_p - \Delta_c = 2\Delta_g$) can result in EIT at $\Delta_c = -2\Delta_g$ for $\Delta_p = 0$ case. Three different values of coupling beam detuning $\Delta_c = 0, \pm 2\Delta_g$ are obtained for all the other Λ-subsystems for which the EIT resonance condition is satisfied. Similar calculation for Λ-system (A) has also been carried out which again has shown possible values of coupling beam detuning Δ_c for EIT to occur at $\Delta_c = 0, \pm 2\Delta_g$.

The measurements of probe transmission were done with the increase in the strength of the magnetic field (shown in Fig 2.7) and observed increase in separation between split EIT peaks. This increase in observed separation with the magnetic field strength $B_{||}$ is in accordance with the $2\Delta_g$ as per our analytical calculation. On comparing the EIT signals in two systems, it is clear from the Fig. 2.7 that the central EIT peak for system (B) is higher than the central EIT peak of system (A).

2.3.3 Dependence of EIT on coupling beam strength in presence of magnetic field

The behavior of the observed split EIT signals has also been studied with the variation in coupling beam power, while keeping the probe beam power fixed at $P_p = 0.08$ mW and magnetic field strength fixed at $B_{||}$ =3.4 G. The measured probe transmissions in this study are shown in Fig 2.9 for both the systems (A) and (B). One can readily interpret from Fig 2.9 that the peak separation between the split EIT signals remains invariant during the increase in the power of the coupling beam, while the magnitude of these peaks kept on increasing. One can also note that system (B) shows stronger EIT feature (central EIT

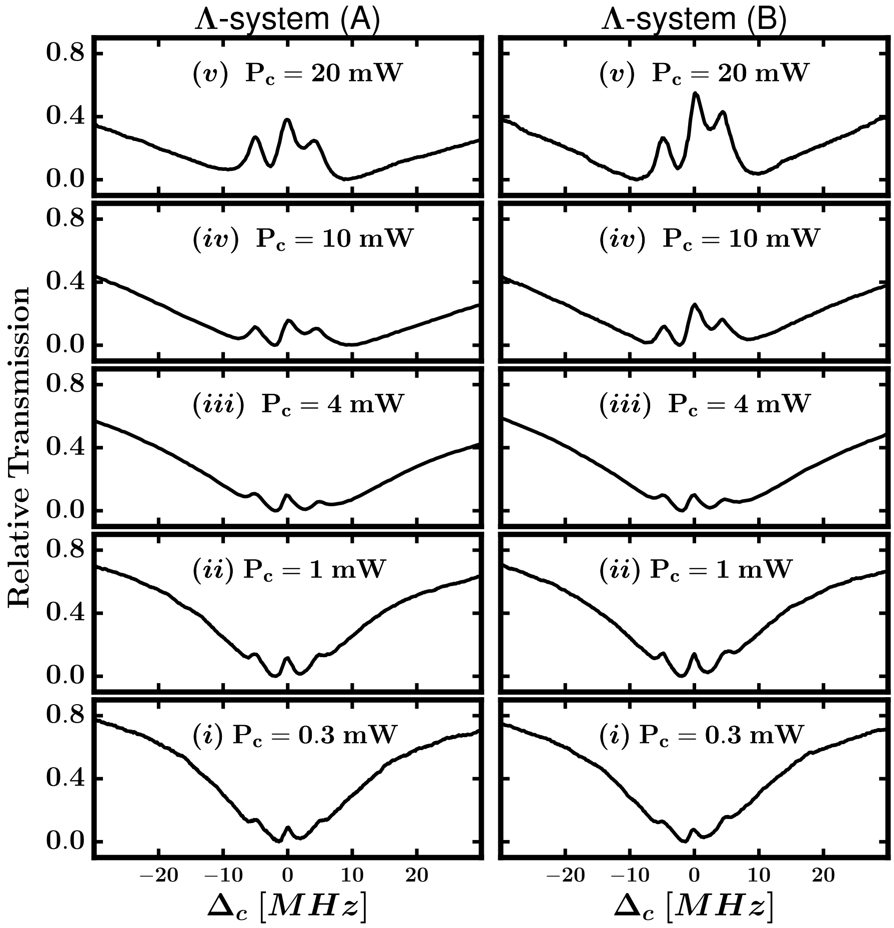

Figure 2.9: The relative probe transmission spectra for both the Λ-systems for different coupling beam powers *(i)-(v)*, in presence of the magnetic field, $B_{\parallel}$= 3.4 G and P_p =0.08 mW, as a function of coupling beam detuning.

peak) than system (A). When the coupling beam power was more than 4 mW , the central EIT peak in the presence of magnetic field showed larger amplitude and higher slope than the EIT signal in the absence of magnetic field. For a particular case, the EIT signal in absence and presence of magnetic field is shown in Fig 2.10 and slope of these signals is presented in inset of Fig 2.10. We compared the magnitude of slope of two signals at resonance and obtained that the central EIT peak in the presence of magnetic field exhibits more than two fold larger slope than that of the EIT peak in absence of magnetic field. Because of the higher slope, the split EIT signals in the presence of magnetic field could be a better choice for precise laser frequency locking. Also, side split peaks can be used for laser locking at frequencies controlled by the strength of the magnetic field.

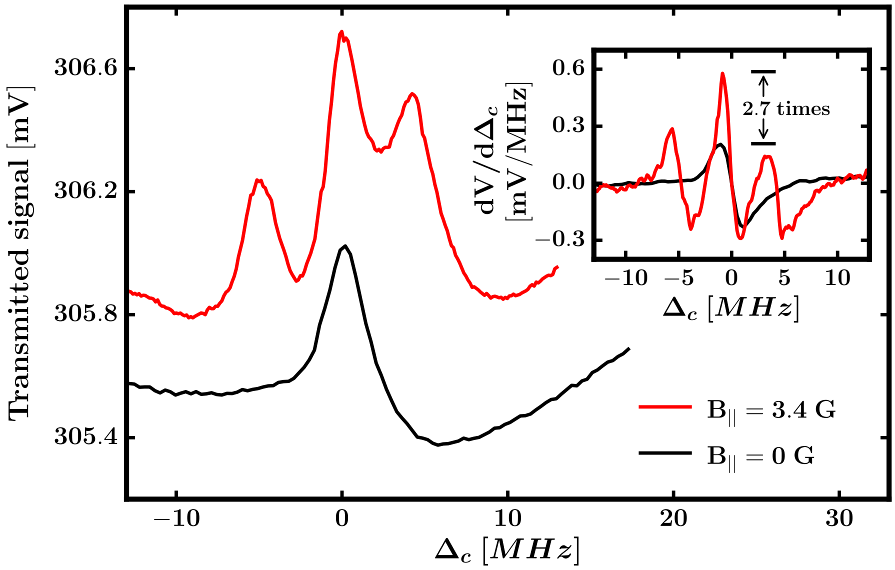

Figure 2.10: The transmitted probe signal versus coupling beam detuning for Λ-system (B) in the absence (*i.e.* $B_{||} = 0\ G$ with black curve) and in the presence of the magnetic field (*i.e.* $B_{||} = 3.4\ G$ with red curve). Here, the coupling power is P_c =20 mW and the probe power is P_p =0.08 mW. The EIT peak in absence of the magnetic field, shown in black color, is offset by -10 mV to increase the visibility. The slope of the transmitted signal, obtained by taking derivative with respect to the detuning of the coupling beam, is shown in the inset. The slope of the signal in the presence of magnetic field is 2.7 times larger than the slope of the signal in the absence of magnetic field

.

In order to model both the Λ-systems in the presence of magnetic field, the hyperfine splitting (*i.e.* 11 sublevels for system (A) and 13 sublevels for system (B)) due to Zeeman effect should also be considered. Considering all the 13 Zeeman sublevels of the Λ-system (B) interacting with the applied probe and coupling beams, the Hamiltonian can be written as,

$$H = \hbar \sum_{i=0}^{12} \omega_{ii} |i\rangle\langle i| + \frac{\hbar}{2} \sum_{i=0}^{i=2} \sum_{j=8}^{j=12} \Omega_p^{i,j} |i\rangle\langle j| + \frac{\hbar}{2} \sum_{i=3}^{i=7} \sum_{j=8}^{j=12} \Omega_c^{i,j} |i\rangle\langle j| + H.c. \quad (2.7)$$

Here, i and j represents the different Zeeman hyperfine ground states (m_F) and excited states ($m_{F'}$) respectively between which transition occurs following the dipole selection rule $m_{F'} - m_F = \pm 1$ (Fig 2.1(b)). $\hbar\omega_{ii}$ is the energy of state $|i\rangle$.

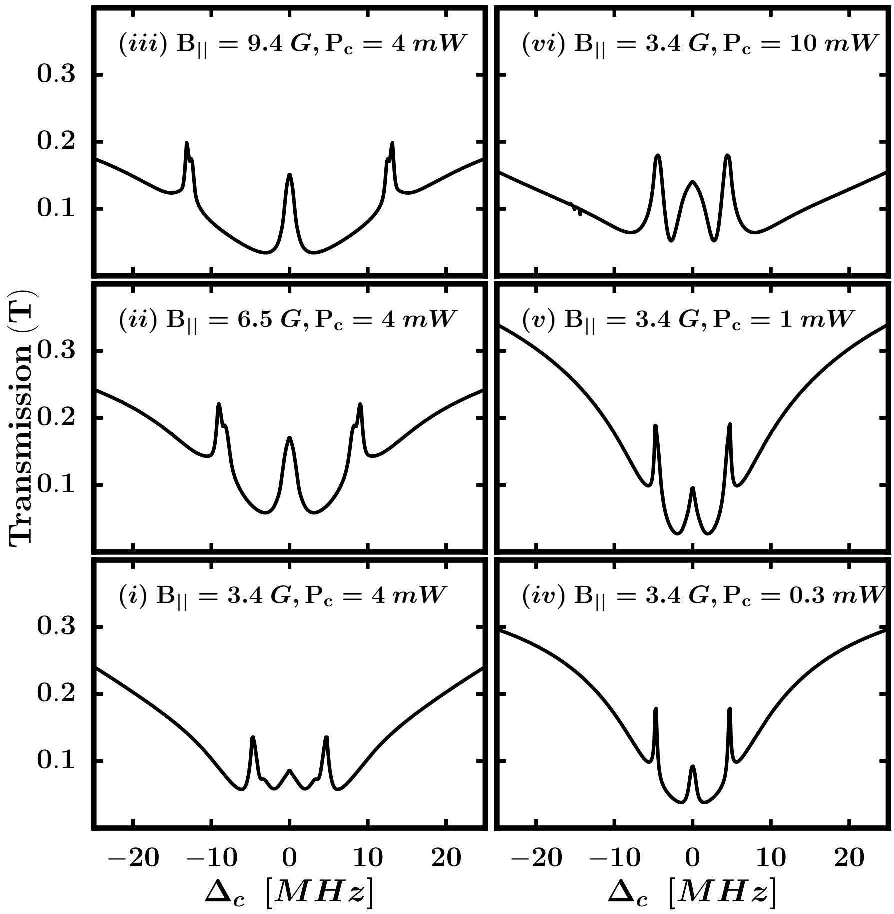

Figure 2.11: The calculated probe transmission spectra (for Λ-system B) for three different longitudinal magnetic field strengths with a fixed coupling power P_c =4 mW is shown in plots *(i)*-*(iii)*. The calculated spectra for three different coupling field powers with a fixed magnetic field strength of 3.4 G is shown in plots *(iv)*-*(vi)*. The left column shows change in separation between split EIT peaks with the strength of magnetic field whereas the right column shows the change in amplitude and line shape of split EIT peaks with the coupling beam power.

Using the above Hamiltonian in equation (2.7), the Liouvelli equation (2.3) has been solved from where all probe coherences have been used to obtain susceptibility. To incorporate the effects of thermal motions, susceptibility is averaged over Maxwell Boltzmann velocity distribution ($W(v)$). The probe transmission T was then calculated as a function of coupling beam detuning for different values of magnetic field strength (shown in Fig 2.11 (*i*)-(*iii*)) and for different coupling beam power (shown in Fig 2.11 (*iv*)-(*vi*)). The numerically obtained variation in the peak separation with the strength of applied magnetic field (Fig 2.11 (i)-(iii)) are in good agreement with the experimental observations (Fig 2.7 (ii)-(iv) for Λ-system (B)). The appearance of split EIT peaks in the numerical results is also in agreement with the analytical explanation provided in the earlier section, besides being in agreement with the experimental observations.

The calculated probe transmission with the variation in the coupling beam power at fixed magnetic field strength 3.4 G is shown in Fig 2.11 (curves (iv)-(vi)). With increase in the coupling power, broadening in all the three EIT peaks is obsevable in the calculated spectra. Qualitatively, the numerically obtained results agree with the experimentally observed results. However, a better matching may be obtained by incorporating various effects such as spin exchange relaxations [80], collisions [79], etc in the theoretical model. Nevertheless, the shown numerical results provide an insight into the EIT phenomenon in these multi-level systems and can be employed to investigate similar other systems.

2.3.4 Probe transmission in presence of standing wave coupling field

After obtaining consistently stronger EIT signal for the case of Λ-system (B), the study further proceeded with standing wave coupling field for Λ-system (B) only. To create the standing wave in the atomic medium, a zero degree mirror is placed after vapor cell as shown in Fig 2.2. The incident coupling beam on this mirror gets retro-reflected and forms standing wave inside the Rb vapor cell. The probe transmission is measured with transverse coupling beam (obtained by blocking retro-reflected coupling beam) and with standing wave coupling beam (obtained by allowing retro-reflected coupling beam). The observed result is shown in Fig 2.12. For the case of travelling wave coupling beam, the moving atoms interact with the probe beam and results in three VSOP dips [73]. The central absorption dip is corresponding to transition between $5^2S_{1/2}F = 1$ and $5^2P_{3/2}F' = 2$, where an EIT peak emerged with sub-natural line-width as shown in Fig 2.12 (a). The observed transmitted probe signal with the retro-reflected coupling beam inside the atomic medium (*i.e.* with a standing wave coupling field) is shown in Fig 2.12 (b). At resonance,

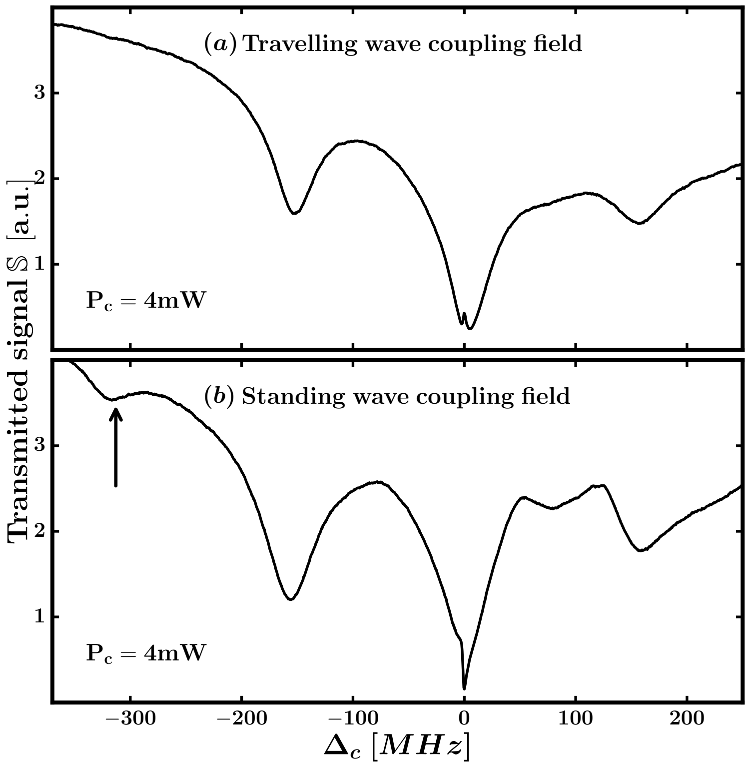

Figure 2.12: The transmitted probe beam signal as a function of coupling beam detuning for coupling field as a (a) travelling wave and (b) standing wave. The probe beam power and coupling beam power are ~0.08 mW ~4 mW respectively.

instead of EIT, an enhanced absorption signal is emerged. This enhanced absorption exhibits subnatural linewidth which suggests that this could be due to EIA effect. With the change in coupling beam from travelling wave to standing wave, the transformation of EIT into enhanced absorption has also been reported earlier [81]. In [81], the authors have attributed the enhanced absorption to losses due to Bragg reflection. However, in our experiment, we have not observed any Bragg reflected signal of the probe beam. So, because of the subnatural linewidth of the observed enhanced absorption, we attribute this absorption to the EIA effect.

Along with the conversion of EIT into EIA, the standing wave coupling beam has also modified the VSOP absorption dips. The VSOP dips obtained in the presence of standing wave coupling beam are deeper than the VSOP dips with travelling wave coupling beam. This may be due to contribution of more atoms to the process of velocity selective absorp-

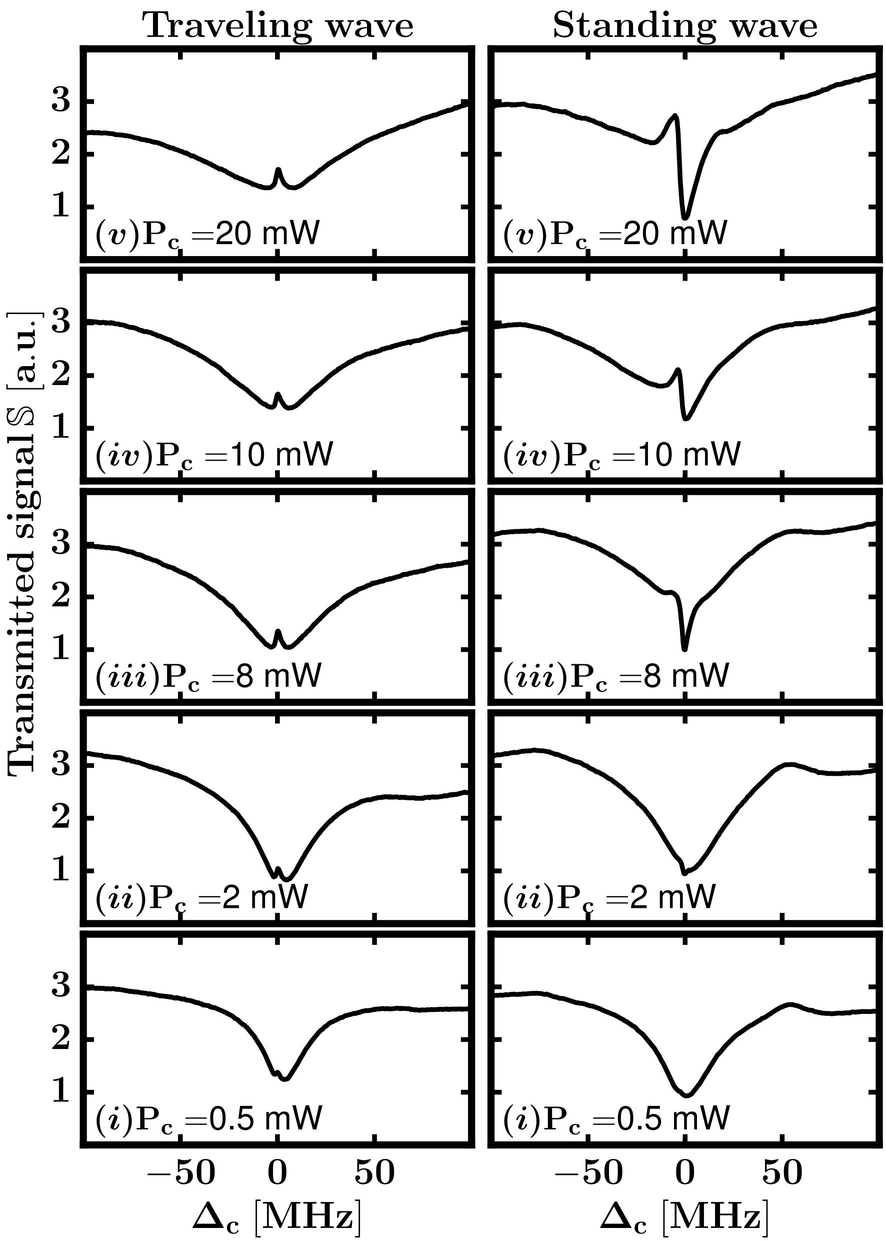

Figure 2.13: The transmitted probe beam signals (P_p =0.08 mW) for five (i-v) different coupling beam powers with travelling wave coupling beam configuration (left) and standing wave coupling beam configuration (right) are shown as a function of detuning of the coupling beam. The power mentioned in right plot (for standing wave coupling field) corresponds to power of only co-propagating coupling field.

tion. In the measured probe transmission spectrum, an additional VSOP absorption dip at coupling beam detuning $\Delta_c \sim -314$ MHz (marked by a black arrow in Fig. 2.12 (b)) has been observed with the standing wave coupling field configuration. This emergence of this additional VSOP dip is due to interaction of a particular velocity class of atoms with the probe beam and only counter-propagating coupling beam.

Subsequently, the dependence of EIT and EIA signal on coupling beam power is investigated. The probe transmitted signals as a function of the coupling beam detuning for different values of coupling beam powers are shown in Fig. 2.13. With increase in the coupling beam power, in case of the travelling wave, the amplitude of the EIT signals increases. Similarly, for the case of standing wave coupling beam, the increase in the coupling beam power above $P_c = 2$ mW resulted in increase in EIA depth in the transmitted probe signal. It is observed that, for travelling wave coupling power as low as $P_c = 0.5$ mW, the EIT signal observed with the travelling wave disappears as retro-reflected coupling beam is introduced.

Previously, several groups [82, 83] have dealt the change in quantum interference effect with the standing wave coupling field. In a Λ scheme, the interaction of atom with a standing wave coupling field has been presented earlier by [84]. They have shown that the standing wave coupling field influences the weak probe absorption via three different processes. The first process is known as the population effect, which accounts for the modification in the velocity distribution of populations in different levels via multi-photon processes induced by coupling beam. The second process involves the modification in the spectral response of an atom due to velocity dependent multi-photon interaction and ac-stark shift effects. The last process considers the stationary atoms where the spectral response of these atoms depend upon its position due to spatial variation in intensity in the standing wave field. Later on, results of this dressed state picture were used by several groups to analyze the quantum interference effects in these multi-level atomic systems [85, 81, 86]. Following the model presented by Erkki Kyr**öl**ä and Rainer Salomaa in [83], where the periodicity in time (t) as well as space (z) has been considered, a numerical model can also be developed for the lambda system with the standing wave coupling beam [9] to obtain an in depth understanding of the measured spectral features (Fig 2.13).

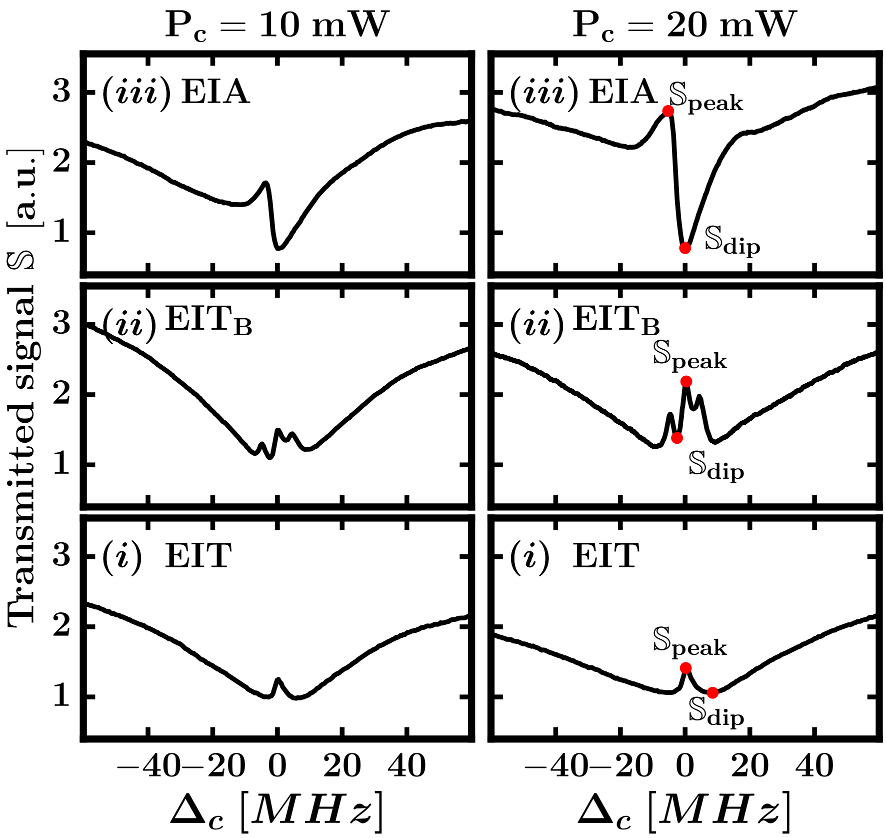

Figure 2.14: Plots show the measured signals: (i) EIT without magnetic field, (ii) EIT with magnetic field and (iii) EIA signal. The left and right columns are for different coupling beam powers of 10 mW and 20 mW. Red dots are kept to evaluate the slope of the signals.

One of the prominent features of the obtained EIA signal is the higher amplitude and slope as compared to the observed EIT signals in the travelling wave coupling beam configuration. A comparison of the EIA and EIT signals both in absence and in presence of a magnetic field is shown in Fig 2.14 for two different coupling beam powers. As discussed in above studies that the slope of central EIT peak in the presence of axial magnetic field is two fold higher [87], therefore, EIT in presence of magnetic field has also been included in this comparitive study.

With the increase in coupling beam power, the amplitude and slope of the signal increases. To quantify the comparison, the slope of the signals has been calculated as the ratio of the difference between the transparency values at peak and dip with the difference in

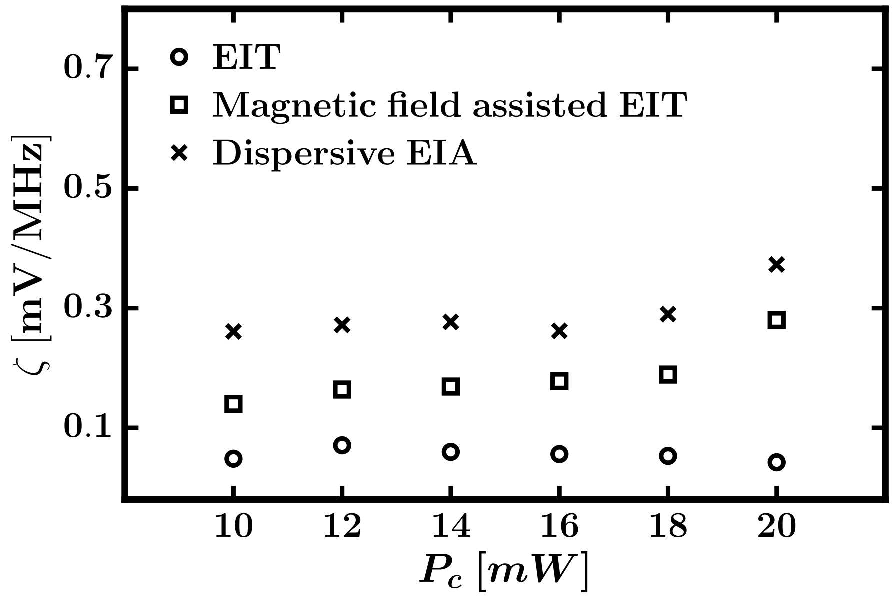

Figure 2.15: The variation in ζ (eq. 2.8) for EIT in absence (circle) and in presence (square) of a longitudinal magnetic field and EIA (cross) are plotted as a function of the coupling beam power.

the corresponding detuning values at all coupling beam powers. Mathematically, this is defined as,

$$\zeta = \left| \frac{\mathbb{S}^{peak} - \mathbb{S}^{dip}}{\Delta_c^{peak} - \Delta_c^{dip}} \right|, \tag{2.8}$$

where $\mathbb{S}^{peak/dip}$ is transparency value of peak/dip and $\Delta_c^{peak/dip}$ is corresponding value of coupling beam detuning as shown by red dot in Fig 2.14.

As the higher value of ζ gives reduced relative frequency uncertainty, the signals with larger ζ values are preferably useful for applications like precise locking of laser frequencies and optical switching devices with the higher stability and performance. The calculated values of ζ are shown in Fig 2.15 for the three specific configurations studied and one can readily interpret that the EIA signal is more advantageous than both the EIT cases for application purposes due to its higher slope and larger amplitude. The application of these EIA signals in the field of precise laser frequency locking can be promising over often used EIT signal.

2.4 Conclusion

In this chapter, a comparative study of EIT has been carried out at room temperature. Initially, the comparison of EIT signal in two Λ-systems in D_2 line transition of ^{87}Rb atom has been made at different conditions. The EIT is investigated with the variation in coupling beam power in absence and presence of a longitudinal magnetic field and with the variation in the strength of the magnetic field. In absence of magnetic field, it is observed that one of the Λ-system exhibit stronger and more symmetric EIT signal than that of other system. Another peculiar feature observed is that EIT for both the system exhibit narrow linewidth even at high coupling power. In presence of a longitudinal magnetic field, there exist three split-EIT peaks for both the systems. In the presence of magnetic field and higher coupling beam power, again earlier established prevailed Λ-system has shown larger amplitude and slope of central EIT peak than that in other Λ-system. The slope of the central EIT peak in the presence of magnetic field is found to be ~ 2.7 times larger than the slope of EIT in absence of magnetic field. This study suggests that the prevailed Λ-system and EIT in presence of magnetic field is suitable for any application purpose.

Thereafter, the supreme Λ-system has been investigated with a standing wave coupling beam, where EIA signal has been observed. A comparison of slope of this EIA signal with the slope of the EIT signal in absence and presence of a magnetic field for diffrent coupling beam power has been made. For all coupling power, the EIA signal has shown larger slope than the other two signals. Thus, it is concluded that the EIA signal can be preferably chosen for tight laser locking application as this signal provides higher stability for locking.

Chapter 3

Electromagnetically induced transparency in N-systems of cold ^{87}Rb atoms

3.1 Introduction

This chapter presents the study of EIT in two N-systems in cold ^{87}Rb atoms. The ensemble of cold atoms effectively reduces the collisional dephasing rate in the medium and also removes the Doppler effect in the spectral feature. N-system is an extension of a three-level Λ-system, where an additional field (named as control field) interacts with one of the ground states of the Λ-system to another excited state. The two N-systems are prepared with the probe, coupling and control beams with transitions in D_2 line of ^{87}Rb atom. At the begining of this chapter, a theoretical model of these two N-systems using density matrix approach is presented. Thereafter, the experimental details and the experimental and numerical results have been discussed. A dual EIT structure in the probe transmission spectrum of both the N-systems has been observed, which is explained using a semi-classical dressed state approach. The manipulation of dual EIT spectral features depending on the strength and detuning of the coupling and control beams have been shown in this chapter.

3.2 Theoretical modeling

Table 3.1: Transitions involved in various systems

system	coupling ($5^2S_{1/2} \rightarrow 5^2P_{3/2}$)	probe ($5^2S_{1/2} \rightarrow 5^2P_{3/2}$)	control ($5^2S_{1/2} \rightarrow 5^2P_{3/2}$)
Λ_A	$F = 1 \rightarrow F' = 1$	$F = 2 \rightarrow F' = 1$	-
Λ_B	$F = 1 \rightarrow F' = 2$	$F = 2 \rightarrow F' = 2$	-
N_A	$F = 1 \rightarrow F' = 1$	$F = 2 \rightarrow F' = 1$	$F = 1 \rightarrow F' = 2$
N_B	$F = 1 \rightarrow F' = 2$	$F = 2 \rightarrow F' = 2$	$F = 1 \rightarrow F' = 1$

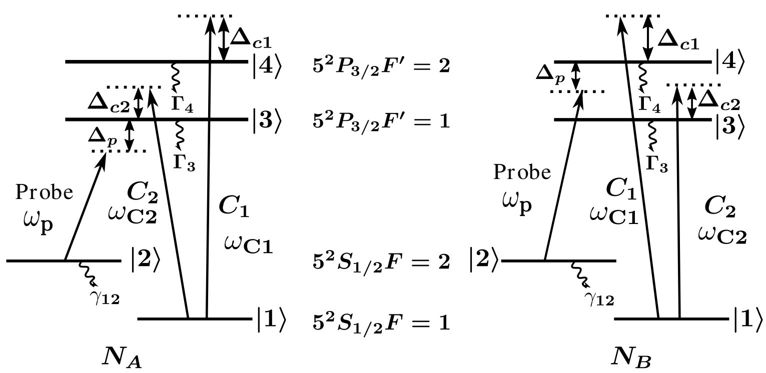

Figure 3.1: The energy level diagram of ^{87}Rb atom showing two N-systems N_A and N_B.

The N-systems, considered in our study, are shown in Fig 3.1. These N-systems are prepared by applying a control field in Λ-systems. The first Λ-system (referred as Λ_A), formed by the probe field at transition $5^2S_{1/2}$ $F = 2 \rightarrow 5^2P_{3/2}$ $F' = 1$ and coupling field at transition $5^2S_{1/2}$ $F = 1 \rightarrow 5^2P_{3/2}$ $F' = 1$. This Λ_A-system is converted to a N-system N_A by applying a control field C_1 to excite the transition $5^2S_{1/2}$ $F = 1 \rightarrow 5^2P_{3/2}$ $F' = 2$. Similarly, the atomic system Λ_B formed by the probe field with transition $5^2S_{1/2}$ $F = 2 \rightarrow 5^2P_{3/2}$ $F' = 2$ and coupling field at transition $5^2S_{1/2}$ $F = 1 \rightarrow 5^2P_{3/2}$ $F' = 2$ is converted to another N-system N_B in presence of control field C_2 exciting the $5^2S_{1/2}$ $F = 1 \rightarrow 5^2P_{3/2}$ $F' = 1$ transition. It should be noted that the drive fields C_1 and C_2 play he role of control and coupling fields respectively for system N_A, while for system N_B, these fields play the role of coupling and control fields respectively . The coupling, probe and control fields transitions for different systems (Λ_A, Λ_B, N_A and N_B) are shown in table 3.1. In the Fig 3.1, the detuning of the fields are defined as $\Delta_p = \omega_{32} - \omega_p$ for system N_A, $\Delta_p = \omega_{42} - \omega_p$ for system N_B, $\Delta_{c1} = \omega_{41} - \omega_{c1}$ and $\Delta_{c2} = \omega_{31} - \omega_{c2}$ for both the systems N_A and N_B. Here, ω_p, ω_{c1}, and ω_{c2} are frequencies of probe field and drive fields C_1 and C_2.

The light-atom interaction in the above N-systems are modeled by solving the Liouville equation, which can be written in terms of density matrix ρ and the Hamiltonian H and as,

$$\frac{\partial \rho}{\partial t} = -\frac{i}{\hbar}[H, \rho] + \Gamma \rho. \tag{3.1}$$

In right side of equation (3.1), the first term shows unitary evolution and second term represents decay of the atomic system. The total Hamiltonian is composed of atomic Hamiltonian H_0 and interaction Hamiltonian H_I, *i.e.*

$$H = H_0 + H_I. \tag{3.2}$$

The atomic Hamiltonian for system N_A can be written as,

$$H_0 = \hbar(\omega_{11}|1\rangle\langle 1| + \omega_{22}|2\rangle\langle 2| + \omega_{33}|3\rangle\langle 3| + \omega_{44}|4\rangle\langle 4|), \tag{3.3}$$

where, $\hbar\omega_{ii}$ is energy of state $|i\rangle$ with $i \in \{1, 2, 3, 4\}$. For system N_A, the interaction Hamiltonia can be written as,

$$H_I = -(\mu_{13} \cdot E_{c2}|1\rangle\langle 3| + \mu_{14} \cdot E_{c1}|1\rangle\langle 4| + \mu_{23} \cdot E_p|2\rangle\langle 3| + h.c.), \tag{3.4}$$

where μ_{ij} is dipole moment operator corresponding to transition between states i and j, and E_k with $k \in \{p, c_1, c_2\}$ is the electric field associated with the probe and drive beams

C_1 and C_2. The E_k can be expressed as,

$$E_k = \mathcal{E}_k cos(\omega_k t).$$

The total Hamiltonian in interaction picture is obtained using the time evolution operator $U = e^{-\frac{iH_0 t}{\hbar}}$ and the rotating wave approximation (RWA) is applied. The transformed Hamiltonian in rotating frame under RWA can be written as (derivation is provided in Appendix C)

$$\tilde{H} = \frac{\hbar}{2}\begin{bmatrix} -2\Delta_{c2} & 0 & \Omega_{c2} & \Omega_{c1} \\ 0 & -2\Delta_p & \Omega_p & 0 \\ \Omega_{c2} & \Omega_p & 0 & 0 \\ \Omega_{c1} & 0 & 0 & 2(\Delta_{c1} - \Delta_{c2}) \end{bmatrix}. \tag{3.5}$$

Here, Ω_k with $k\epsilon\{p, c_1, c_2\}$ are Rabi frequencies representing the coupling strengths of the interacting fields, and can be expressed as $\Omega_k = -\frac{\mu_{ij}\cdot\mathcal{E}_k}{\hbar}$.

Using the transformed Hamiltonian from equation (3.5) in the Liouville equation (equation (3.1)), a set of the density matrix evolution equations for atomic system N_A (in unit $\hbar = 1$) can be obtained as,

$$\begin{aligned}
\frac{\partial\rho_{11}}{\partial t} &= -\frac{i}{2}\Omega_{c2}(\rho_{31} - \rho_{13}) \\
&\quad - \frac{i}{2}\Omega_{c1}(\rho_{41} - \rho_{14}) + \Gamma_4\rho_{44} + \frac{\Gamma_3}{2}\rho_{33} \\
\frac{\partial\rho_{22}}{\partial t} &= -\frac{i}{2}\Omega_p(\rho_{32} - \rho_{23}) + \frac{\Gamma_3}{2}\rho_{33} \\
\frac{\partial\rho_{33}}{\partial t} &= -\frac{i}{2}\Omega_{c2}(\rho_{13} - \rho_{31}) - \frac{i}{2}\Omega_p(\rho_{23} - \rho_{32}) - \Gamma_3\rho_{33} \\
\frac{\partial\rho_{44}}{\partial t} &= -\frac{i}{2}\Omega_{c1}(\rho_{14} - \rho_{41}) - \Gamma_4\rho_{44}
\end{aligned}$$

$$
\begin{aligned}
\frac{\partial\rho_{12}}{\partial t} &= \Big(-i(\Delta_p - \Delta_{c2}) - \gamma_{12}\Big)\rho_{12} - \frac{i}{2}\Omega_{c2}\rho_{32} \\
&+ \frac{i}{2}\Omega_p\rho_{13} - \frac{i}{2}\Omega_{c1}\rho_{42} \\
\frac{\partial\rho_{13}}{\partial t} &= \left(i\Delta_{c2} - \frac{\Gamma_3}{2}\right)\rho_{13} - \frac{i}{2}\Omega_{c1}\rho_{43} \\
&+ \frac{i}{2}\Omega_{c2}(\rho_{11} - \rho_{33}) + \frac{i}{2}\Omega_p\rho_{12} \\
\frac{\partial\rho_{14}}{\partial t} &= \left(i\Delta_{c1} - \frac{\Gamma_4}{2}\right)\rho_{14} \\
&- \frac{i}{2}\Omega_{c2}\rho_{34} + \frac{i}{2}\Omega_{c1}(\rho_{11} - \rho_{44}) \\
\frac{\partial\rho_{23}}{\partial t} &= \left(i(\Delta_p) - \frac{\Gamma_3}{2}\right)\rho_{23} \\
&+ \frac{i}{2}\Omega_p(\rho_{22} - \rho_{33}) + \frac{i}{2}\Omega_{c2}\rho_{21} \\
\frac{\partial\rho_{24}}{\partial t} &= \left(i\Delta_p - \Delta_{c2} + \Delta_{c1} - \frac{\Gamma_4}{2}\right)\rho_{24} \\
&- \frac{i}{2}\Omega_p\rho_{34} + \frac{i}{2}\Omega_{c1}\rho_{21} \\
\frac{\partial\rho_{34}}{\partial t} &= \left(i(\Delta_{c1} - \Delta_{c2}) - \frac{\Gamma_3 + \Gamma_4}{2}\right)\rho_{34} \\
&- \frac{i}{2}\Omega_p\rho_{24} + \frac{i}{2}\Omega_{c1}\rho_{31} - \frac{i}{2}\Omega_{c2}\rho_{14}
\end{aligned}
$$

with,

$$
\frac{\partial\rho_{ij}}{\partial t} = \frac{\partial\rho^*_{ji}}{\partial t}. \tag{3.6}
$$

Γ_i is spontaneous decay rate of i^{th} state and γ_{12} is dephasing rate.

Similarly, set of density matrix equations for atomic system N_B can also be obtained. Using matrix method, the set of equations in equation (**??**) are solved at steady state condition by substituting $\dot{\rho} = 0$.

3.3 Experimental Setup

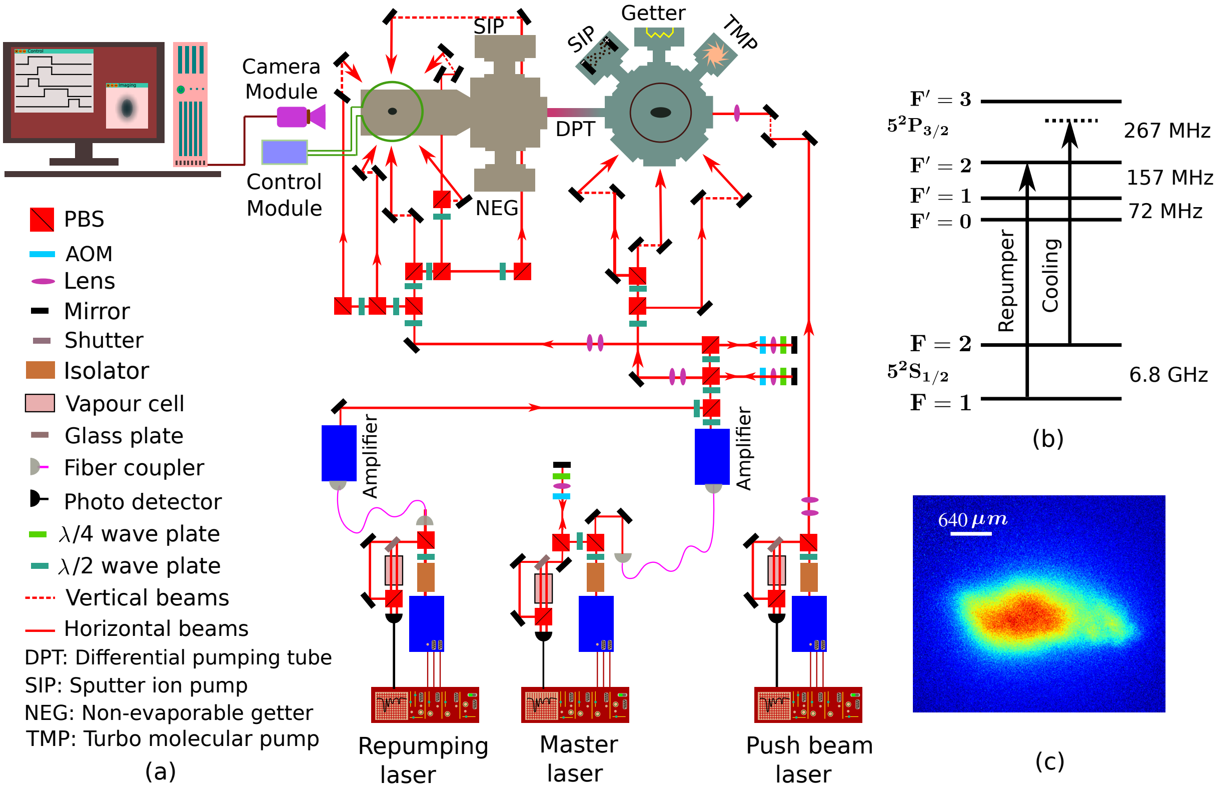

Figure 3.2: (a) The schematic diagram of double MOT setup showing vacuum chambers, laser beams, optical layout and controller systems. (b) The energy level diagram of D_2 line transition of ^{87}Rb showing transitions of cooling and repumping beams. (c) Fluorescence image of cold-atom cloud in UHV-MOT.

A double magneto-optical trap setup has been used for experiments. The schematic diagram of this experimental setup is shown in Fig 3.2. The setup includes the major systems like vacuum systems, lasers and optical systems and EIT measurements. A detailed description of the different segments is provided as following.

3.3.1 Vacuum system

The vacuum system comprises of an octagonal stainless steel chamber (vapor chamber (VC)) and a quartz glass cell (ultra high vacuum (UHV) cell) connected through a differential pumping tube (DPT). The vapor chamber has two faces with size NW63CF and eight faces with size NW35CF. One of the faces with size NW63CF is connected to a turbo molecular pump (TMP) of 70 liter/sec capacity (Turbo-V70LP, Varian) through a pneumatic gate valve (Fillunger Gate valve 63CF). The TMP provides the inital pumping to a pressure of 10^{-3} Torr. For pumping the chamber to a pressure of 10^{-8} Torr, a sputter ion pump (SIP) of capacity 20 liter/sec (VacIon starcell) is connected to this vapor chamber. A Bayerd-Alpert gauge is used to monitor the pressure inside the chamber. The Rubidium vapor inside the chamber was supplied by heating the Rb-getters (Rb/NF/3.4/12 FT10+10, SAES getters) connected through a T-joint of NW35CF dimension. This getter module provides sufficient Rb vapor for formation of first MOT, called as VC-MOT.

Another part of the vacuum system is a quartz glass cell (Optiglass, UK) attached to a hollow cube. This hollow cube is made of stainless steel (SS) and has six ports of dimension NW35CF. One port of the cube connects glass cell and opposite port connects a differential pumping tube (DPT) of length 122 mm whose another end is attached with the octagonal vapor chamber. A sputter ion pump (SIP) with capacity 300 liter/sec (VacIon plus 300 liter/sec starcell) is connected to one of the ports of SS cube. A non-evaporable getter (NEG) pump (GP-100 MK5, SORB-AC MK5 type cartridge pump from SAES getters, Italy) is connected to the other port of the SS cube. These pumps are used to attain a very low pressure of $\sim 5 \times 10^{-11}$ Torr in the glass cell, which is essential if magnetic trapping and evaporating cooling experiments are to be performed. The second MOT, called UHV-MOT, is prepared in this glass cell. The pressure inside the glass cell is monitored by an extractor type gauge (Oerlikon leybold). The pressure gradient between vapor chamber and the glass cell is maintained due to use of DPT. The inner diameter of DPT is 2.25 mm upto 60 mm length and the inner diameter of rest 62 mm length is 5 mm. The diameter of 2.25 mm side of tube is kept towards VC-MOT side and diameter of 5 mm side is kept towards glas cell side. This helps in accomodating the expanding beam of atoms during the transfer of atoms from VC-MOT to UHV-MOT.

To reach the desired vacuum in vapor chamber and glass cell, a sequence of procedure is followed. A brief description of the procedure is as follows. Initially, a rotary pump and the TMP connected to the vapor chamber is switched on for nearly 24 hours. These pumps reduce the pressure in the vapor chamber to 10^{-7} Torr. Thereafter, the complete setup is baked at 200^0C for a week. For baking, the whole system is covered by Aluminium foil, which helps in uniform heating throughout the chamber, and then heating tapes are wrapped over it. Since glass cell is fragile, heating is done using a hot-blower type heater. Special care is followed to avoid overlapping of heating tapes during the whole process. At the final stage of the baking, SIP is activated to eliminate adsorbed gas particles from the inner parts of the pump. At this stage, the NEG pump is also activated repeatedly by passing a current in range of 6 to 8 A. Rb-getters are activated by flow of current from 6 A to 8 A for 4 to 5 seconds multiple times in the inerval of 1 minute. At the end, the TMP is isolated from the vacuum chamber by closing the gate valve and the system is allowed to cool to room temperature (which was kept 20^0C) to reach the required pressure.

3.3.2 Optical systems

The double MOT setup is prepared using three extended cavity diode lasers (ECDLs), two amplifiers and numerous optical elements like polarizing beam splitters (PBS), mirrors, half and quarter wave plates, acousto optical modulators (AOMs) and lenses. All the lasers are operated at the D_2 line transition of ^{87}Rb *i.e.* 780 nm. The ECDL system provides narrow line-width less than 1 MHz with a wide tunability of wavelength. To avoid the entrance of backscattered light from optical elements into ECDL, a Faraday isolator is kept after ECDL.

One of the ECDL (Toptica, DL 100, Germany) is used to derive cooling beam with fixed frequency at $\sim$ 15 MHz red detuned from cooling transition frequency $5^2S_{1/2}\ F = 2 \rightarrow 5^2P_{3/2}\ F' = 3$ of ^{87}Rb atom for both the MOTs. The laser output is fed into a tapered amplifier (TABoosta, Toptica, Germany) to obtain the amplified output power $\sim$ 550 mW. A repumping beam for both the MOTs is derived from another ECDL, where output is fed into a different amplifier (TABoosta, Toptica, Germany) to obtain amplified power of

$\sim$ 260 mW. The frequency of repumping beam is kept fixed at the resonance frequency corresponding to transition $5^2S_{1/2}\ F = 1\ \rightarrow 5^2P_{3/2}\ F' = 2$. The cooling and repumping beams are mixed and then split into two parts using polarizing beam splitter. One part is used for VC-MOT and other is used for UHV-MOT. The beam for VC-MOT is split into three beams each having power 9 mW (6 mW for cooling beam and 3 mW for repumping beam) which are incident in the vacuum chamber from three directions in retro-reflection mode. The trapped atoms in the VC-MOT are then transferred to the quartz glass cell using a red detuned push beam. The push beam is obtained from another ECDL (Sacher, Germany) and its frequency is kept 1 GHz red detuned from the cooling transition. The push beam is focused to a diameter of 35 μm on the VC-MOT cloud with a 300 mm lens. The push beam transfers the atom flux from the VC-MOT to the glass cell, where the atoms are captured in the UHV-MOT.

The UHV-MOT is prepared using six independent laser beams each having 7 mW of power (5 mW in cooling beam and 2 mW in repumping beam). The $1/e^2$-radius of cooling and repumping beams for both the MOTs is 6 mm and the magnetic field gradients are kept $\sim$ 10 $G\ cm^{-1}$ and $\sim$ 15 $G\ cm^{-1}$ for VC-MOT and UHV-MOT respectively. The fluoresence image of the UHV-MOT cloud is captured using a CCD camera (Pixelfly model USB) with the help of an appropriate 2f-imaging optics. One of the fluoresence images is shown in Fig 3.2 (c).

During the MOT preparation, the frequency of lasers are controlled using the saturation absorption spectroscopy (SAS) technique. This technique removes Doppler broadening from transmission probe spectrum and results in resolved hyperfine transition peaks. In SAS, two beams are generated from same source and made to counter-propagate inside an atomic medium. One of the beam is strong which serves as a pump beam and other beam is weak which serves as a probe beam and collected by photo-diode. The strong pump beam depletes the population from the ground state due to which probe absorption corresponding to hyperfine transition frequency reduces for zero velocity class atoms. Thus, peaks appear at probe frequencies corresponding to hyperfine transition frequencies in the probe transmission spectrum. For the laser frequency at half of two atomic transition frequencies, a particular non-zero velocity class of atom see same and opposite Doppler shifted frequency of pump and probe beam which again result in transmission peak due to depletion of the ground state population. These peaks are known as crossover peaks. These resolved transmission peaks in probe transmission spectrum serve as a reference signal and allows side lock of laser frequency.

A required shift in laser frequency for MOT preparation is achieved using AOM in a double pass configuration. In the AOM, a radio frequency drive creates acoustic wave which diffracts the incident beam and give output of zeroth and higher order beams. In double pass configuration, the obtained first order beam is retro-reflected to enter the AOM again from exit end and gets diffracted again. This way the frequency of the incident laser beam is shifted twice. In double pass configuration, we are able to obtain a shift in frequency of first-order diffracted beam from 120 MHz to 200 MHz.

3.3.3 Electromagnetically induced transparency measurements setup

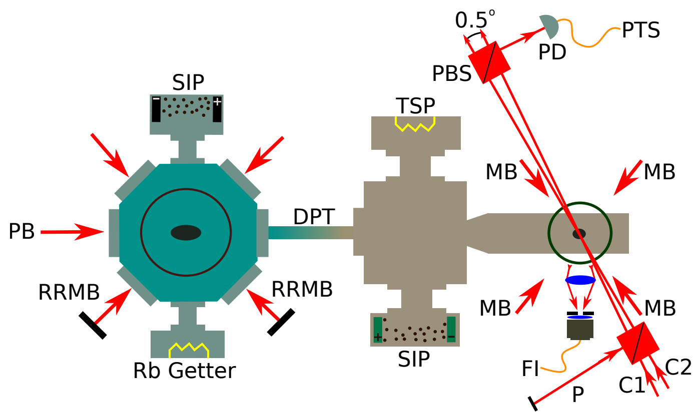

Figure 3.3: The schematic of the experimental setup for EIT measurements. PB: push beam, RRMB: retro-reflected MOT beams, DPT:differential pumping tube, SIP: sputter-ion pump, TSP: titanium sublimation pump, PBS: polarizing beam splitter, MB: MOT beams, FI: fluorescence imaging, SASS: saturated absorption spectroscopy signal, ECDL: extended cavity diode laser, P: probe beam, C1, C2: coupling beams, PD: photo diode, PTS: probe transmission signal.

The EIT experiment was performed in the UHV-MOT atom cloud with number $\sim 5\times10^7$ and temperature $\sim$ 300 μ K. In EIT measurements, two drive beams and a probe beam was passed through the UHV-MOT atom cloud. The drive beams were obtained from the tapered amplifier (TABoosta, Toptica, Germany) which was used to deliver the repumping transition in the magneto optical traps. The repumping beam has frequency corresponding to the transition $5^2S_{1/2}F = 1 \rightarrow 5^2P_{3/2}F' = 2$. Using a half-waveplate and a polarizing beam splitter this obtained beam was then split into two. Hereafter, one splitted part is referred as drive beam C_1, and the frequency of other one is shifted corresponding to the frequency of transition $5^2S_{1/2}F = 1 \rightarrow 5^2P_{3/2}F' = 1$ by passing this part of beam through another AOM in double pass configuration. This beam is referred as drive beam C_2. A separate diode laser (Toptica, DL 100, Germany, with sub MHz linewidth and $\sim$ 3 mm $1/e^2$-radius) delivered the probe beam. The probe beam and drive beam C_1 were overlapped to make them co-propagating while the drive beam C_2 was kept at a relative angle of $\sim$ 0.5 degree with respect to the probe beam. The beam alignment for EIT experiment is shown in the Fig 3.3. The probe beam polarization was linear orthogonal with respect to the drive beams (C_1 and C_2) polarization. After UHV-MOT cloud, using a half-waveplate and a polarizing beam splitter the probe beam was separated out from the drive beams and a photodiode connected with a digital oscilloscope was employed to display and record the probe signal. For system N_A, the probe beam frequency was scanned across the transition $5^2S_{1/2}F = 2 \rightarrow 5^2P_{3/2}F' = 1$, and for system N_B, the scan was across the transition $5^2S_{1/2}F = 2 \rightarrow 5^2P_{3/2}F' = 2$. For both the systems, the drive beams frequencies were kept at resonance. The measurement was done in the presence of MOT beams. The effect of MOT beams on the EIT spectra was considered negligible due to low intensity of MOT beams.

3.4 Results and discussion

In this section, the experimental and theoretical investigation of the probe transmission spectrum depending on the drive fields (coupling and control) strength and detuning has been presented. Since the Clebsch-Gordan (CG) coefficient governs the strength of a transition between two states, the probe beam transition strength is larger for atomic system N_B than that of system N_A for a given power in probe beam. Whereas, the strength of both the drive beams transitions are same due to the equal CG coefficients of both the drive beams. In the experiments, the probe beam power was fixed at $\sim 30\ \mu$ W, and the drive beams powers were varied to study their effect on the probe transmission.

Normalization along with averaging over multiple records has been used to display the experimentally obtained individual transmission spectra and the error bar over the measured transmission data is shown by the grey shade in all the figures. The normalization of probe transmission is carried out using the expression $T = \frac{S - S_{min}}{S_{max} - S_{min}}$ with S being the transmitted probe signal and S_{max} and S_{min} being the far off resonant and minimum value of the transmitted probe signal respectively.

3.4.1 Transmission spectrum of Λ and N-system

The probe transmission spectrum for both the N-systems and Λ-systems (*i.e.* by removing control beam of N-system) were measured. During the experiments, the power in both the drive beams were fixed at 12 mW and the drive beams frequencies were kept at resonance. Fig 3.4 (i) and (ii) show the observed spectral features of systems (A) and (B) respectively. The probe transmission spectrum exhibits the expected EIT features for the Λ-systems (*i.e.* in absence of control beams, C_1 for system (A) and C_2 for system (B)). As has been shown in previous chapter as well as reported earlier [87], the EIT signal of system Λ_B is stronger than the EIT signal of system Λ_A. The transmission for system Λ_A is ~ 30 % and for system Λ_B is ~ 50 %. At the location of these EIT signals (*i.e.,* at line center), a

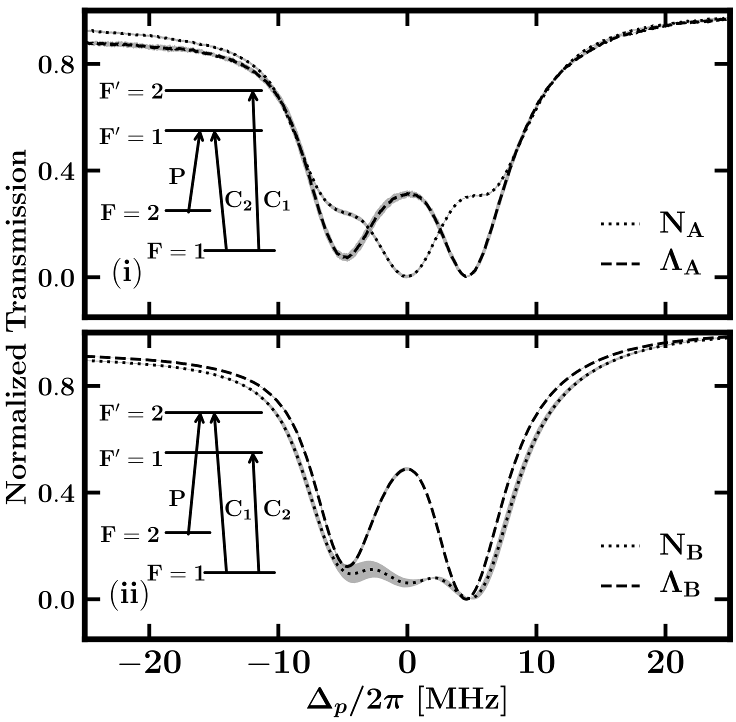

Figure 3.4: The experimentally measured normalized probe transmission spectrum at probe beam power of ~ 30 μW and both drive beams (C_1 and C_2) power of 12 mW for (i) system (A) and (ii) system (B). The dashed curves represent Λ-system, and dotted lines stand for N-system.

transmission dip appears on applying the control beam forming systems N_A and N_B. This central transmission dip gives a dual EIT structure in the probe transmission spectrum of N-systems (dotted curves in Fig 3.4 (i) and (ii)).

In the presence of control beam, the emergence of central transmission dip can be explained using a semi-classical dressed state formalism. In the dressed state approach, we consider a three-level atomic system where two drive beams C_1 and C_2 interacts resonantly. The effect of probe beam is negligible due to its weak strength and hence it has not been considered for the dressed state approach. The Hamiltonian of this system can be written as,

$$\tilde{H}_1 = \frac{1}{2}\begin{bmatrix} 0 & \Omega_{c2} & \Omega_{c1} \\ \Omega_{c2} & 0 & 0 \\ \Omega_{c1} & 0 & 0 \end{bmatrix}. \tag{3.7}$$

The energy of dressed states can be obtained by diagonalizing the Hamiltonian $\tilde{H}_1$. The obtained eigen values are 0, $-\frac{1}{2}\sqrt{\Omega_{c1}^2 + \Omega_{c2}^2}$, and $\frac{1}{2}\sqrt{\Omega_{c1}^2 + \Omega_{c2}^2}$ and corresponding eigen states are $|0\rangle_{DN}$, $|-\rangle_{DN}$ and $|+\rangle_{DN}$ respectively, where,

$$|0\rangle_{DN} = -\frac{\Omega_{c1}}{\Omega_c'}|3\rangle + \frac{\Omega_{c2}}{\Omega_c'}|4\rangle, \tag{3.8}$$

$$|-\rangle_{DN} = \frac{1}{\sqrt{2}}\left(|1\rangle - \frac{\Omega_{c2}}{\Omega_c'}|3\rangle - \frac{\Omega_{c1}}{\Omega_c'}|4\rangle\right), \tag{3.9}$$

$$|+\rangle_{DN} = \frac{1}{\sqrt{2}}\left(|1\rangle + \frac{\Omega_{c2}}{\Omega_c'}|3\rangle + \frac{\Omega_{c1}}{\Omega_c'}|4\rangle\right), \tag{3.10}$$

where $\Omega_c' = \sqrt{\Omega_{c1}^2 + \Omega_{c2}^2}$, with Ω_{c1} and Ω_{c2} as coupling strengths of the drive beams C_1 and C_2 respectively. These dressed states are illustrated in Fig 3.5. In the absence of control beam, *i.e.* for Λ-system, the strong coupling field creates two dressed states $|+\rangle_{D\Lambda}$ and $|-\rangle_{D\Lambda}$ with eigen-energies $\pm\Omega_c/2$ respectively. The transition of probe field from ground state to these two dressed states gives Autler-Townes splitting (ATS) in the probe transmission spectrum (shown by dashed curve in Fig 3.4). The additional beam of N-System, *i.e.* the control beam, shifts the energy of two dressed states (as calculated and shown before equation (3.8)) which further broadens the Autler-Townes splitting. In addition to this, an additional dressed state $|0\rangle_{DN}$ with zero eigen-energy is created by the control beam. The probe transition from ground state to this dressed state results in transmission dip at the line center. From this dressed state approach, it is clear that the

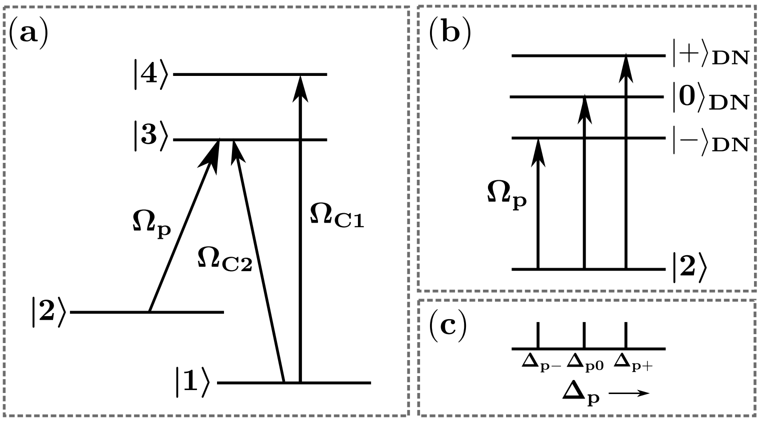

Figure 3.5: (a) shows the bare states of four-level N-system interacting with two strong drive fields of strength Ω_{c1} and Ω_{c2} and a probe field of strength Ω_p. (b) shows the formation of dressed-states due to interaction of strong fields Ω_{c1} and Ω_{c2}. (c) shows the probe transition probability in frequency space. The allowed probe transitions exist at probe detunings $\Delta_{p-} = -\frac{1}{2}\sqrt{\Omega_{c1}^2 + \Omega_{c2}^2}$, $\Delta_{p0} = 0$, $\Delta_{p+} = \frac{1}{2}\sqrt{\Omega_{c1}^2 + \Omega_{c2}^2}$.

side transmission dips (referred hereafter as AT dips) in the probe transmission spectrum is due to the coupling field and central transmission dip is due to the control field. The conversion of transparency into absorption at line centre in the presence of control beam finds the place for application in optical switching devices.

The dual EIT structure in N-system has been investigated with the variation in the strength and detuning of the coupling and control beam, and the probe transmission spectrum is measured. For better visibility of peaks, each of the measured probe transmission spectrum has been processed using a peak sharpening convolution algorithm [88]. The average of the measured transmission spectra is shown by dotted curve and the average of processed spectra is shown by continuous curve in the experimental plots in Figs (3.6)-(3.8). For clear visibility, the transmission spectra for different parameters are plotted with suitable vertical shift.

3.4.2 Dependence on coupling and control beam strength

To see the effect of strength of drive beams on N-system, we varied the power in drive beam C_2 and kept the power in drive beam C_1 fixed at 12 mW. As the drive beam C_2 acts

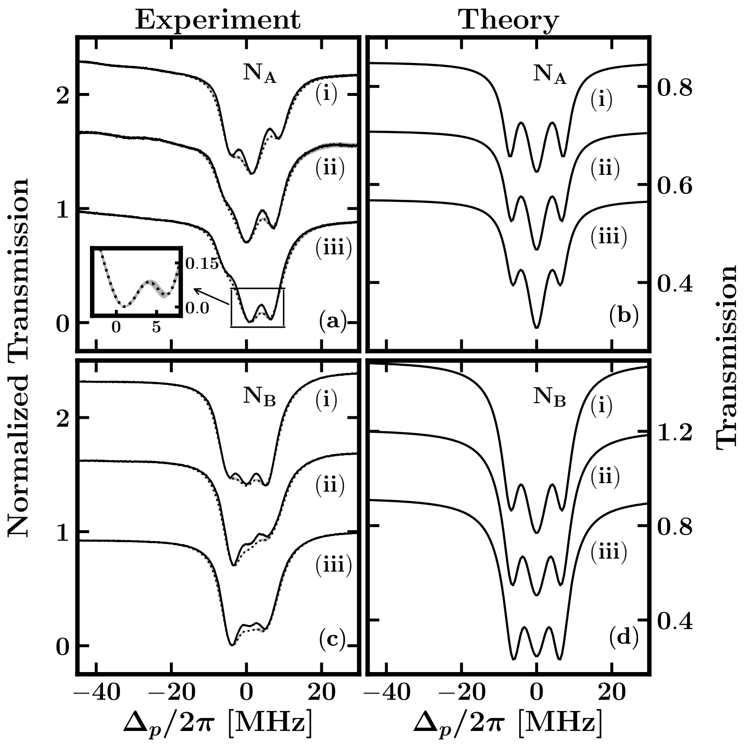

Figure 3.6: Plots (a) and (c) correspond to the normalized experimental probe transmission spectrum for systems N_A and N_B at different drive beam power P_{c2}. The curves corresponding to different power values P_{c2} are : *(i)* 12 mW, *(ii)* 10 mW, and *(iii)* 8 mW. The power in beam C_1 is fixed, *i.e.,* P_{c1} = 12 mW. Dotted curves are for average of measured probe transmission and continuous curves are for the average of processed transmission data. Inset in plot (a) presents the enhanced view of curve *(iii)* for better visualization of error bar shown by grey shade. Plots (b) and (d) correspond to the calculated probe transmission spectrum with strength $\Omega_{c2}/2\pi$ as: *(i)* 10 MHz, *(ii)* 9 MHz, and *(iii)* 8 MHz. The strength of other coupling field kept fixed,*i.e.,* $\Omega_{c1}/2\pi$= 10.0 MHz, for both the systems N_A and N_B. The other parameters used in the numerical simulations for plot (b) and (d) are $\Omega_p/2\pi$= 0.6 MHz and $\Omega_p/2\pi$= 1.3 MHz respectively. Δ_{c1} and Δ_{c2} are same for both plots and set to be zero.

as a coupling beam for system N_A, we can gain an insight on the effect of variation in strength of coupling beam on N-system by observing the results for system N_A. Similarly, the effect of control beam strength on N-system can be obtained by observing the results of system N_B as beam C_2 is control beam for system N_B. The experimentally measured and numerically calculated probe transmission spectra are shown in Fig 3.6. For system N_A, it is observed that the strength of the AT transmission dips reduces as the power of the drive beam C_2 decreases, whereas the depth of central dip is nearly unaffected (as manifested in Fig 3.6 (a) and (b)). The reason behind this maybe that the drive beam

C_2 plays role of coupling beam for system N_A and its effect on AT transmission dips is higher compared to that on the central transmission dip. The spectral features of system N_B shows reduction in the strength of the central transmission dip as the power in drive beam C_2 decreases (as shown in Fig 3.6 (c)). This may be because the beam C_2 plays a role of control beam for system N_B and is responsible for the emergence of central transmission dip. The probe transmission spectrum for system N_B has been numerically obtained which shows similar behaviour to that of experimental spectrum and is shown in Fig 3.6 (d). Similar observations were made with the change in the power in the drive beam C_1, while keeping fix the C_2 drive beam power. In this case, the system N_A has shown reduction in central transmission dip and system N_B has shown reduction in AT transmission dips, with decrease in the power of the drive beam C_1. In the numerical calculations, the field's Rabi frequencies were kept close to the experimental one and decay rates were $\Gamma_3 = \Gamma_4 = 2\pi \times 6\ MHz$ *i.e.* decay rate of excited states in D_2 line of ^{87}Rb atom and $\gamma_{12} = 2\pi \times 1\ MHz$ for incorporating laser linewidth. In the experimentally measured probe transmission spectrum, some asymmetries has been noted in comparison to the theoretically calculated transmission. This may be because of several aspects not considered in the simulations, such as, Zeeman splitting of energy levels due to magnetic field of MOT, presence of neighbouring levels in the excited transition and spatial inhomogeneity in coupling strength of the fields.

3.4.3 Dependence on coupling and control beam detuning

For detuning dependent study, the frequency detunings of both the drive beams were varied simultaneously (*i.e.,* $\Delta_{c1} = \Delta_{c2}$) from -$2\pi\times$ 9 MHz to $2\pi\times$ 10 MHz, while keeping the powers in both the drive beams fixed at ~ 12 mW. The experimental and numerical results of this study are shown in Fig 3.7. For the case of far detuned drive beams, the probe transmission spectra has shown two asymmetric transmission dips for both the systems (curves *(i)* and *(iii)* of Fig 3.7) which is a typical signature of detuned Λ system. This

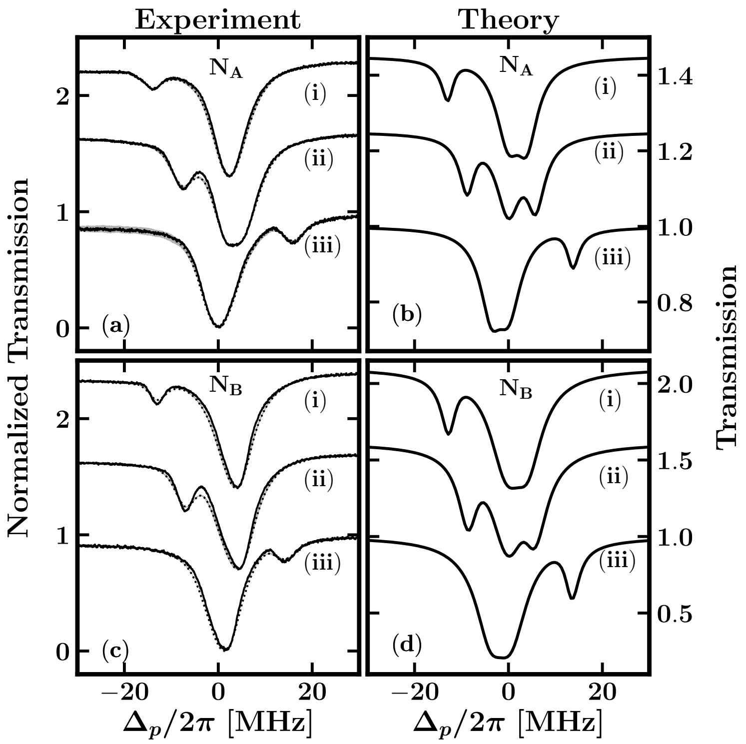

Figure 3.7: Plots (a) and (c) depict the measured normalized probe transmission spectrum for systems N_A and N_B and plots (b) and (d) depicts the calculated probe transmission spectrum for systems N_A and N_B, with the variation in detuning of both the drive beams. The $\Delta_{c1}/2\pi$ and $\Delta_{c2}/2\pi$ values corresponding to different curves are: *(i)* ~ - 9 MHz, *(ii)* ~ - 3 MHz, *(iii)* ~ 10 MHz. The Powers in both the drive beams are 12 mW and corresponding coupling strength, *i.e.,* $\Omega_{c1}/2\pi$ = $\Omega_{c2}/2\pi$= 10 MHz, is used in numerical simulation. The probe field strength considered for simulations are $\Omega_p/2\pi$= 0.6 MHz for systems N_A (plot (b)) and 1.3 MHz for system N_B (plot (d)). In plots (a) and (c), continuous and dotted curves correspond to the average of processed transmission data and measured probe transmission respectively.

is because when both the drive beams are far detuned, the systems N_A and N_B becomes detuned Λ-systems with corresponding detuned control beam. This far detuned control beam acts as a perturbation and cause asymmetry in the transmission spectrum. For near detuning value ($- \sim 2\pi{\times}3$ MHz) of both the drive beams, a weak splitting in the transmission dip have been observed in the numerical results, visible in Fig 3.7 (b) *(ii)* and (d) *(ii)* around the zero probe detuning, showing a recovery towards the transmission spectrum usually obtained for the N-systems. The experimental results however have not shown any visible splitting in Fig 3.7 (a) *(ii)* and (c) *(ii)*.

Further, to see the independent effect of the coupling and control beam detuning on the

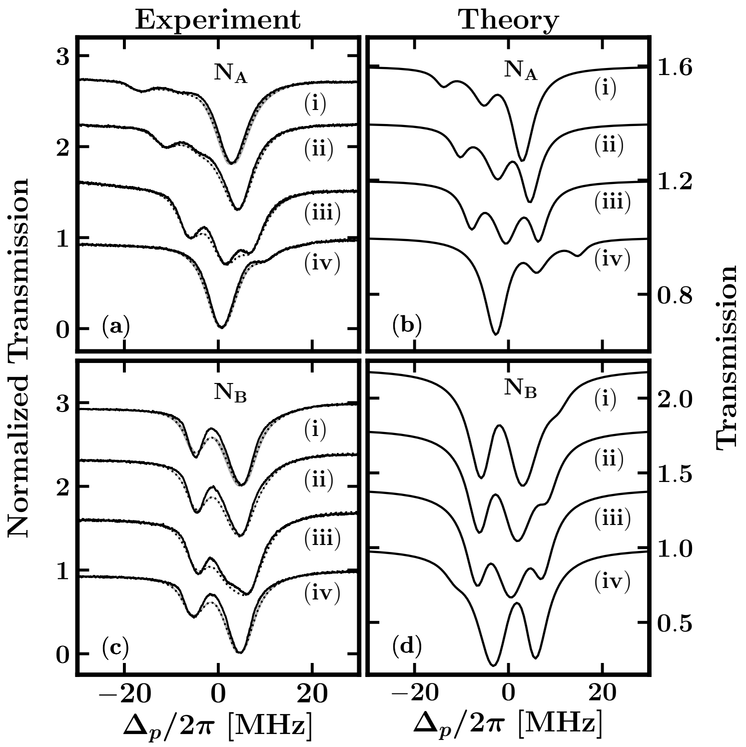

Figure 3.8: Plots (a) and (c) show the measured normalized probe transmission versus the probe beam detuning Δ_p for systems N_A and N_B respectively. The different curves is for different detuning values of the drive beam C_2 (Δ_{c2}). During the measurement, detuning Δ_{c1} was kept zero and drive beam powers were $P_{c1} = P_{c2} = 12$ mW. Dotted and continuous curves correspond to the average of measured probe transmission and processed transmission data respectively. Plots (b) and (d) show the calculated transmission as a function of probe beam detuning $\Delta_p/2\pi$ for different coupling field detunings $\Delta_{c2}/2\pi$ while $\Delta_{c1}/2\pi = 0$ and field strengths $\Omega_{c1}/2\pi = \Omega_{c2}/2\pi = 10$ MHz. Corresponding detuning values $\Delta_{c2}/2\pi$ for all the plots are kept around *(i)* - 8 MHz, *(ii)* - 4 MHz, *(iii)* 1 MHz, *(iv)* 9 MHz. Here $\Omega_p/2\pi$= 0.6 MHz and 1.3 MHz for systems N_A and N_B respectively.

probe transmission spectrum of N-system, the detuning of the drive beam C_2 has been varied and the other drive beam C_1 kept fixed at resonance. In this study, the effect of detuning of the coupling beam can be obtained from the transmission spectrum of system N_A, while the effect of detuning of the control beam can be observed from the transmission spectrum of system N_B. The results of experiment and numerical calculations for system N_A are shown in Fig 3.8 (a) and (b). For the case of far red detuned coupling field, the two transmission dips appear at red detuned positions and one transmission dip appears at resonance in the probe transmission spectrum (curve (*i*) in Fig 3.8 (a) and (b)). For the case of blue detuned coupling field C_2, similar spectral features appear in the probe transmission spectrum with positions of transmission dips swapped towards blue side (curve (*iv*) in Fig 3.8 (a) and (b)). The presence of resonant control and detuned coupling fields in the N-system shift all the three dressed states $|+\rangle_{DN}$, $|-\rangle_{DN}$ and $|0\rangle_{DN}$ (refer Fig 3.5), which eventually shifts the three transmission dips in the N-system. For the case of near resonant coupling field (curve (*iii*) in Fig 3.8 (a) and (b)), the spectral features recover to three transmission dips forming dual EIT structure at the resonant probe beam frequency. For system N_B, the variation in detuning of beam C_2 will reveal the effect of variation in the detuning of the control beam on the probe transmission spectrum of N-system. This effect is shown in Fig 3.8 (c) and (d). The far detuned control field has resulted in a single EIT peak at resonance (shown by curves (*i*),(*ii*) and (*iv*) in Fig 3.8 (c) and (d)). This EIT peak is the feature of a Λ-system (i.e. Λ_B) with some asymmetry, possibly due to perturbation of the control beam. The inter-conversion between absorption and transmission at probe resonance with the variation of control beam detuning is an interesting observation in the N-system. The results in Fig 3.8 suggest that the spectral features of N-system can be manipulated considerably by tuning the frequencies of drive beams. The control beam detuning can either produce dual EIT peak or single EIT peak in the probe transmission spectrum of N-system.

3.5 Conclusion

In this chapter, a theoretical and experimental investigation of two N-systems in D_2 line transition of cold ^{87}Rb atoms have been carried out. A density matrix formalism has been used in the theoretical study and the experiments were performed in cold ^{87}Rb atoms trapped in a magneto-optical trap. A dual EIT structure has been observed in the probe transmission spectrum of N-system due to emergence of a transmission dip at center of Autler-Townes splitting. The explanation of these transmission dips has been presented using a semi-classical dressed state approach.

The probe transmission spectrum of N-systems have further been investigated depending on the strength and detuning of the coupling and control beams. The obtained probe spectrum has shown that the central transmission dip is affected by the control beam of N-system and side transmission dips are dependent on the coupling beam of N-system. For a far detuning of coupling and control beam, the dual EIT structure disappears and two asymmetric dips in transmission are obtained. The position of these dips vary with sign and magnitude of control and coupling beams detuning. With the variation in the detuning of one drive beam while keeping the other drive beam fixed at resonance, the individual effect of coupling and control beams detuning has been obtained by observing the results of two N-systems. If beam of varying detuning acts as coupling beam for a given N-system, three transmission dips appear in probe transmission. But if varying detuning beam acts as a control beam for the N-system, a single EIT peak of Λ-type system is obtained. This type of dual EIT structure obtained with resonant coupling and control beams of equal power provides opportunity to explore these N-systems for optical communication and switching applications. Also, the two drive beams in N-system offers more degree of freedom to control and manipulation of spectral features depending on strength and detuning parameters of the drive beams.

Chapter 4

Theoretical modelling of EIT in modified inverted-Y system

4.1 Introduction

This chapter presents a theoretical study of EIT in a five-level modified inverted Y-system, hereafter denoted as IY^+-system, for cold atoms. The IY^+-system consists of three basic systems (Λ, ladder and Vee) and two basic derived systems (inverted-Y and N) that can exhibit EIT feature. Although these systems have been studied by several groups [3, 23, 24, 25, 26, 27, 28, 49, 52, 54, 87, 89, 90, 91, 92, 93, 94, 95, 96, 97, 98, 99], an insight into interdependence of these basic systems can be gained by investigating the IY^+-system. In addition to this, the IY^+-system requires three strong coupling fields (along with one weak probe field) which provides an opportunity to control and manipulate the spectral features to a larger extent. For example, in our study, we have obtained inter-conversion, shifting and splitting of the absorption and transparency peaks in the absorption spectrum.

The IY^+-system, for experimental studies, can be prepared by using hyperfine states of ^{87}Rb atom as shown in Fig 4.1, where hyperfine state $5^2S_{1/2}F = 1$ can be used as state

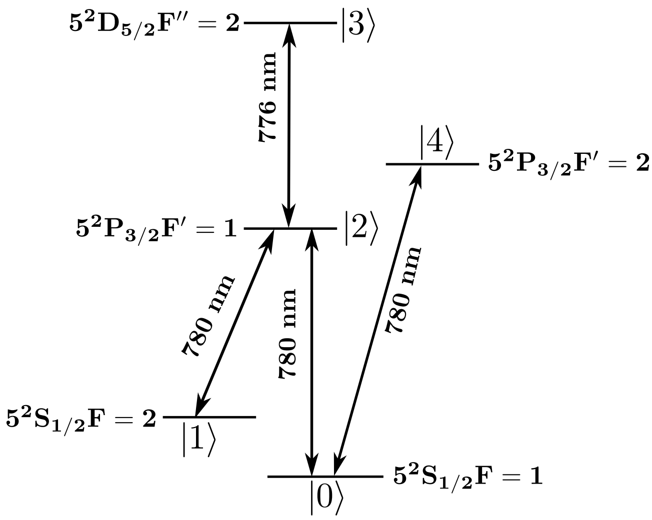

Figure 4.1: The experimentally possible energy-level diagram of IY^+-system in ^{87}Rb atom.

$|0\rangle$, $5^2S_{1/2}F = 2$ as state $|1\rangle$, $5^2P_{3/2}F' = 1$ as state $|2\rangle$, $5^2D_{5/2}F'' = 2$ as state $|3\rangle$ and $5^2P_{3/2}F' = 2$ as state $|4\rangle$. The theoretical prediction made in this chapter can be investigated experimentally in future.

In general, to obtain the dynamics of the atomic system on interaction with electromagnetic fields in steady-state, the rotating wave approximation (RWA) is employed. But, in case of strong off resonant fields interacting with atomic states, results obtained through RWA differ considerably from the actual observations. To investigate the spectral features of the IY^+-system, a numerical matrix propagation method has been used. In this method, the "transient characteristics" as well as the "steady state condition" for a probe field absorption can be obtained by considering the propagation of the complete density matrix in time. The numerical approach to solve the Liouville equation as described in detail in [100, 101], is implemented here to find the solutions of required density matrix elements.

In the beginning, the description of the implemented numerical matrix propagation (NMP) method is presented. Thereafter, the transient characteristics of an inverted-Y system are studied to reach the steady state condition. The spectral features of the inverted-Y system obtained through the NMP method as well as RWA are compared in order to establish the equivalence of NMP method with the conventional RWA method. An additional coupling field connecting one of the ground states in the inverted-Y system with another excited state creates the IY^+-system. The spectral characteristics of IY^+-system depending on all coupling fields strength and detuning has been discussed. The obtained results are explained using dressed and doubly dressed state approach. The conversion of transparency into absorption and vice versa, shifting and splitting of transparency are major outcomes of this study, which opens the path for IY^+-system to be useful for designing of devices like optical switches and multi-channel optical communications.

4.2 Numerical Matrix Propagation method

A brief description of the numerical solution technique employed for this study has been outlined in this section. The generalized electromagnetic field composed of M individual field components can be expressed as,

$$\mathcal{E}(t) = \sum_{p}^{M} \varepsilon_p(\omega_p)\cos(\omega_p t), \tag{4.1}$$

where ω_p and ε_p are angular frequency and field strength for p^{th} field component. For the composite atom-field system, the total Hamiltonian can be written as,

$$H(t) = H_0 + H_I(t), \tag{4.2}$$

where H_0 is the atomic Hamiltonian described in the atomic basis states $\{|\alpha\rangle\}$ as,

$$H_0|\alpha\rangle = \epsilon_i|\alpha\rangle. \tag{4.3}$$

The electromagnetic interaction Hamiltonian H_I under the dipole approximation, can be expressed as,

$$H_I(t) = -\mu.\mathcal{E}(t). \tag{4.4}$$

The evolution of the density matrix ($\rho = \sum_\alpha |\alpha\rangle\langle\alpha|$) for all the atomic levels can be obtained by solving the Liouville equation, which can be expressed as,

$$\frac{\partial}{\partial t}\rho(t) = -\frac{i}{\hbar}\left[H(t), \rho(t)\right] - \frac{1}{\hbar}[R, \rho(t)]. \tag{4.5}$$

In right side of the Liouville equation, the first term is the unitary evolution and the other term represents the decay of the system. The decay term can be explicitly written in terms of the population decay of particular state as well as coherence decay rates between different states as,

$$\left[R, \rho(t)\right]_{\alpha\alpha} = -\Gamma_{\alpha\alpha}\rho_{\alpha\alpha} + \sum_{\beta\neq\alpha} \gamma_{\beta\alpha}\rho_{\beta\beta} \tag{4.6}$$

and,

$$\left[R, \rho(t)\right]_{\alpha\beta} = -\Gamma_{\alpha\beta}\rho_{\alpha\beta}\ (\alpha \neq \beta). \tag{4.7}$$

The decay rates are defined as,

$$\Gamma_{\alpha\beta} = \frac{1}{2}\left(\Gamma_{\alpha\alpha} + \Gamma_{\beta\beta}\right) + \Gamma'_{\alpha\beta} \tag{4.8}$$

with the property

$$\Gamma_{\alpha\beta} = \Gamma_{\beta\alpha} \tag{4.9}$$

and

$$\Gamma_{\alpha\alpha} = \sum_{\beta\neq\alpha}^{N} \gamma_{\alpha\beta}, \tag{4.10}$$

where $\gamma_{\alpha\beta}$ represents the inelastic transition rate and $\Gamma'_{\alpha\beta}$ is dephasing factor due to phase changing collisions which is considered zero in this study. In order to solve the Liouville equation (4.5), the diagonal and off-diagonal elements of the density matrix elements, denoted by complex variables ρ_{ii} and ρ_{ij} respectively, are separated. The evolution of population of state i can be obtained by solving following equation,

$$\begin{aligned}\Re(\dot{\rho_{ii}}) &= \frac{1}{\hbar}\sum_{p}^{M}\sum_{k}^{N}(\Im(\rho_{ik})\mu_{ki} - \mu_{ik}\Im(\rho_{ki}))\varepsilon_p\cos(\omega_p t) \\ &+ \sum_{k\neq i}^{N}\gamma_{ki}\Im(\rho_{kk}) - \Gamma_{ii}\Re(\rho_{ii}).\end{aligned} \tag{4.11}$$

and the evolution of off-diagonal density matrix elements can be obtained by solving following equations,

$$\begin{aligned}\Re(\dot{\rho_{ij}}) &= \frac{\epsilon_{ij}}{\hbar}\Im(\rho_{ij}) \\ &+ \frac{1}{\hbar}\sum_{p}^{M}\sum_{k}^{N}(\Im(\rho_{ik})\mu_{kj} - \mu_{ik}\Im(\rho_{kj}))\varepsilon_p\cos(\omega_p t) \\ &+ \Gamma_{ij}\Re(\rho_{ij})\end{aligned} \tag{4.12}$$

and

$$\begin{aligned}\Im(\dot{\rho_{ij}}) &= \frac{\epsilon_{ij}}{\hbar}\Re(\rho_{ij}) \\ &+ \frac{1}{\hbar}\sum_{p}^{M}\sum_{k}^{N}(\mu_{ik}\Re(\rho_{kj}) - \Re(\rho_{ik})\mu_{kj})\varepsilon_p\cos(\omega_p t) \\ &+ \Gamma_{ij}\Im(\rho_{ij}).\end{aligned} \tag{4.13}$$

Here, $\Re(\rho_{ij})$ and $\Im(\rho_{ij})$ denotes real and imaginary parts of complex density matrix element respectively. The above equations can be solved using fourth-order Runge-Kutta method. The resulting time dependent real element of diagonal density matrix ($\Re(\rho_{ij})$) gives the populations of individual states and time dependent imaginary element of off-diagonal density matrix ($\Im(\rho_{ij})$) gives the absorption between states i and j.

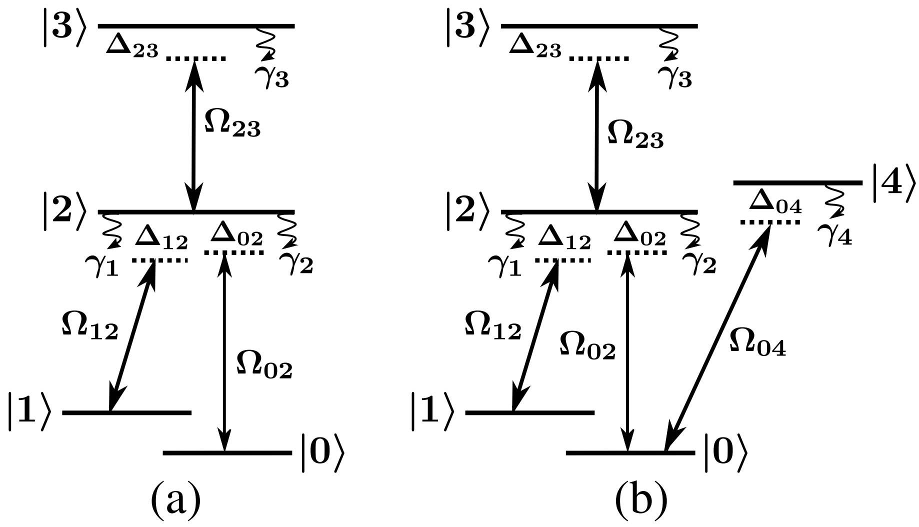

Figure 4.2: Atomic states and field configurations for (a) inverted-Y (IY) system and (b) modified inverted-Y system with $\alpha \in 0, 1, 2, 3, 4$ as atomic energy levels. Ω_{ij} represents the coupling strength of interacting field connecting states i and j and Δ_{ij} is the detuning from corresponding transition between states i and j.

4.3 Transient characteristics and comparison of matrix propagation method with RWA

In order to obtain the numerical stability of the matrix propagation method, the transient response of an inverted-Y (IY) system, shown in Fig 4.2(a), is characterized. The IY-system consists of four levels $|\alpha\rangle$, $\alpha \in \{0, 1, 2, 3\}$ interacting with three electromagnetic fields of strengths Ω_{ij} connecting states i and j, with $i, j \in 0, 1, 2, 3$. Here, Ω_{12} and Ω_{23} are the strengths of two coupling fields and probe field strength is Ω_{02}. In Fig 4.3 (a) and (b), the population of the ground state $|0\rangle$ and the coherence of the probe transition (*i.e.,* $\Im(\rho_{02})$) of the inverted-Y system as a function of scaled time γt is shown respectively. Initially rapid oscillation occurs and then after $\gamma t = 4\pi$ steady state is reached. The system continues to be in the steady state condition without any external perturbation.

To establish the equivalence of both the formalisms (RWA and NMP) in the atomic system, the evolution of the density matrix equations using both the NMP and the RWA method in the low field strength and small detuning regime has been obtained at steady

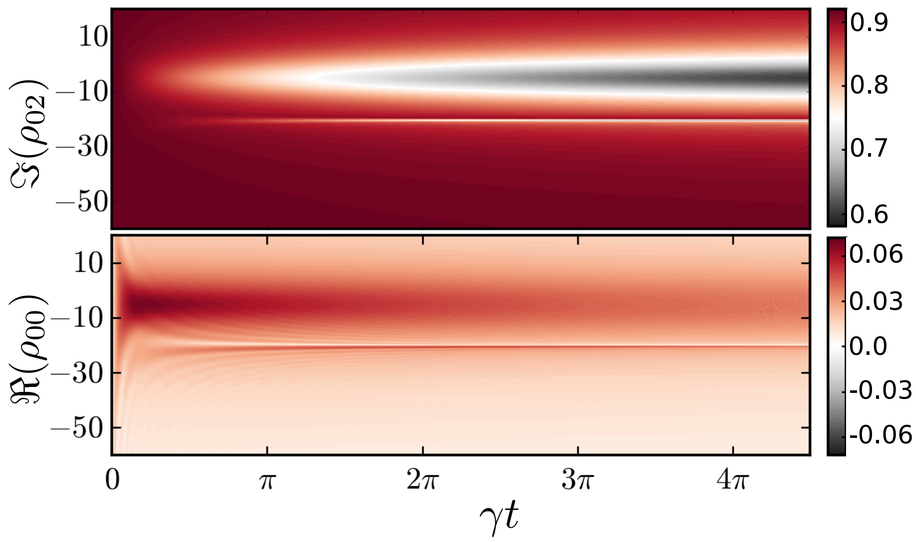

Figure 4.3: Amalgamated spectrum of (a) ground state population $\Re(\rho_{00})$ and (b) probe coherence $\Im(\rho_{02})$ as a function of the dimensionless time γt. The transient characteristics show that the atomic system achieves the "steady state condition" at $\gamma t \sim 4\pi$. The other parameters used in this simulations are $\Omega_{02} = 1.0\gamma$, $\Omega_{12} = 5.0\gamma$, $\Omega_{23} = 5.0\gamma$, $\Delta_{12} = -20\gamma$, $\Delta_{23} = 0$.

state condition. The density matrix evolution equations of the inverted-Y system (Fig. 4.2(a)) under rotating wave approximations can be explicitly written as,

$$
\begin{aligned}
\frac{\partial \rho_{00}}{\partial t} &= 2\gamma_2\rho_{22} - 2\gamma_0\rho_{00} + i\Omega_{02}(\rho_{02} - \rho_{20}) \\
\frac{\partial \rho_{11}}{\partial t} &= 2\gamma_1\rho_{22} + 2\gamma_0\rho_{00} + i\Omega_{12}(\rho_{12} - \rho_{21}) \\
\frac{\partial \rho_{22}}{\partial t} &= -2(\gamma_1 + \gamma_2)\rho_{22} + 2\gamma_3\rho_{33} - i\Omega_{12}(\rho_{12} - \rho_{21}) \\
&\quad - i\Omega_{02}(\rho_{02} - \rho_{20}) + i\Omega_{23}(\rho_{23} - \rho_{32}) \\
\frac{\partial \rho_{33}}{\partial t} &= -2\gamma_3\rho_{33} - i\Omega_{23}(\rho_{23} - \rho_{32}) \\
\frac{\partial \rho_{01}}{\partial t} &= -(\gamma_0 + i(\Delta_{12} - \Delta_{02}))\rho_{01} + i\Omega_1\rho_{02} - i\Omega_{02}\rho_{21} \\
\frac{\partial \rho_{02}}{\partial t} &= -(\gamma_1 + \gamma_2 - i\Delta_{02})\rho_{02} + i\Omega_{12}\rho_{01} \\
&\quad + i\Omega_{23}\rho_{03} + i\Omega_{02}(\rho_{00} - \rho_{22})
\end{aligned}
$$

$$\frac{\partial\rho_{03}}{\partial t} = -(\gamma_0 + \gamma_3 - i(\Delta_{02} + \Delta_{23}))\rho_{03} + i\Omega_{23}\rho_{02}$$
$$- i\Omega_{02}\rho_{23}$$
$$\frac{\partial\rho_{12}}{\partial t} = -(\gamma_1 + \gamma_2 - i\Delta_{12})\rho_{12} + i\Omega_{02}\rho_{10}$$
$$+ i\Omega_{23}\rho_{13} + i\Omega_{12}(\rho_{11} - \rho_{22})$$
$$\frac{\partial\rho_{13}}{\partial t} = -(\gamma_3 - i(\Delta_{12} + \Delta_{23}))\rho_{13} + i\Omega_{23}\rho_{12} - i\Omega_{12}\rho_{23}$$

$$\frac{\partial\rho_{23}}{\partial t} = -(\gamma_1 + \gamma_2 + \gamma_3 - i\Delta_{23})\rho_{23} - i\Omega_{02}\rho_{03} -$$
$$i\Omega_{12}\rho_{13} + i\Omega_{23}(\rho_{22} - \rho_{33})$$

and

$$\frac{\partial\rho_{ij}}{\partial t} = \frac{\partial\rho^*_{ji}}{\partial t}, \tag{4.14}$$

where Δ_{ij} is frequency detuning of the applied electromagnetic fields connecting states i and j. γ_1 and γ_2 are the decay rates of the excited state $|2\rangle$ corresponding to decay of atoms into states $|1\rangle$ and $|0\rangle$ respectively. γ_3 is decay rate from excited state $|3\rangle$ to state $|2\rangle$. Since, the total population is conserved, therefore $\sum_i \rho_{ii} = 1$. For this closed system, the non-radiative relaxation rate of the ground state, i.e. γ_0, is considered to be zero . The above set of equation have been solved using the matrix method in the steady-state condition as,

$$\dot{\rho} = \mathcal{L}\rho = 0. \tag{4.15}$$

$\mathcal{L}$ is the Liouvillian super-operator and its eigenvector corresponding to the 'zero' eigenvalue gives the steady-state value of the density matrix ρ.

To compare the outcomes of two methods, *i.e.* NMP and RWA, the probe coherence

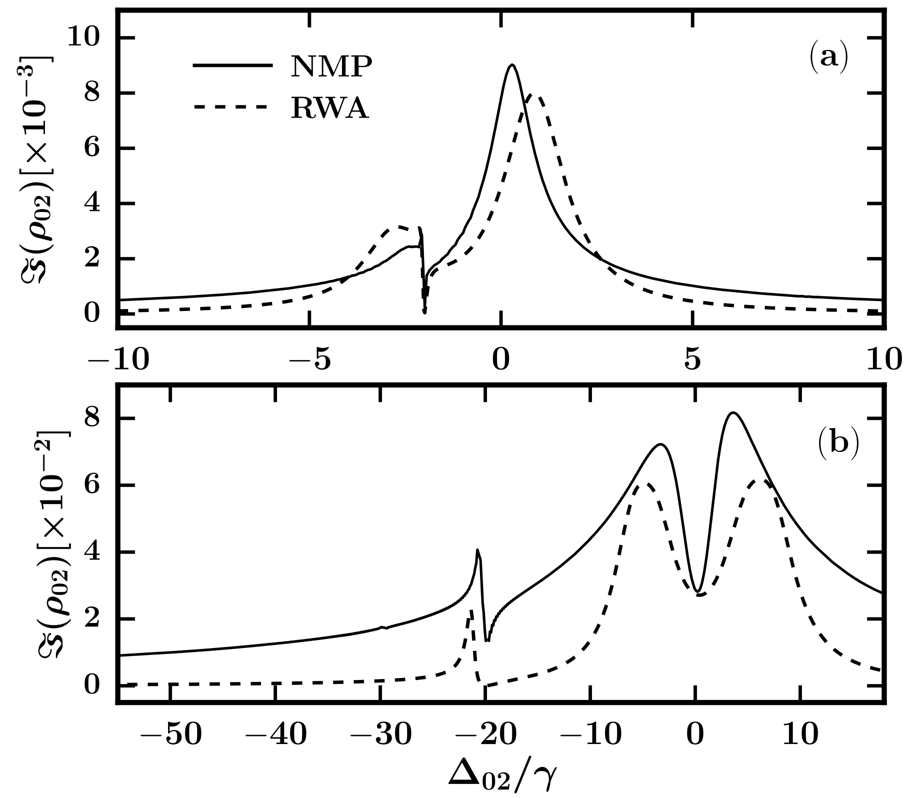

Figure 4.4: The coherence of probe transition $\Im(\rho_{02})$ as a function of scaled probe detuning Δ_{02}. The parameters in plot (a) are $\Omega_{02} = 0.01\gamma$, $\Omega_{12} = 0.5\gamma$, $\Omega_{23} = 1.5\gamma$, $\Delta_{23} = 2\gamma$, $\Delta_{12} = -2\gamma$ and in plot (b) are $\Omega_{02} = 1.0\gamma$, $\Omega_{12} = 5.0\gamma$, $\Omega_{23} = 5.0\gamma$, $\Delta_{23} = 0$, $\Delta_{12} = -20\gamma$.

at steady state condition is obtained using both the methods for different coupling field strengths and detuning regimes, which are shown in Fig 4.4. The spectrum in Fig 4.4 (a) corresponds to the weak coupling field strength *i.e.,* $\Omega_{02} = 0.01\gamma$, $\Omega_{12} = 0.5\gamma$ and $\Omega_{23} = 1.5\gamma$, and low detuning regime *i.e.,* $\Delta_{12} = -2\gamma$ and $\Delta_{23} = 2\gamma$. The other parameters used in the NMP method is $\gamma\delta t = 10^{-5}$ and $\gamma t_{max} = 2\pi \times 15$. The results obtained using RWA (shown by dashed curve) and NMP (shown by continuous curve) methods in weak field strength clearly depicts the equivalence of two methods. The slight shift in the peak of the probe coherence can be attributed to the counter rotating terms neglected in the RWA method.

However, when the field strength is large and fields are far-detuned (Fig 4.4 (b)), the difference between the results of both the methods grow further even though the spectral features remain same. For this case, the field strengths are $\Omega_{02} = 1.0\gamma$, $\Omega_{12} = 5.0\gamma$ and $\Omega_{23} = 5.0\gamma$ with detuning values $\Delta_{12} = -20\gamma$ and $\Delta_{23} = 0$.

4.4 Results and discussions

After establishing the validity of the NMP method and comparing it with the RWA method in the previous section, it is clear that the NMP method can be employed to deal with frequency regimes and field strength regimes which are not usually accessible using RWA. In this section of chapter, the dependence of probe absorption of IY^+-system on different coupling field strengths and detunings is presented.

The IY^+-system (Fig 4.2 (b)) is an extension of inverted-Y system where the ground state ($|0\rangle$) couples with another excited state ($|4\rangle$) via an additional coupling field. This particular atomic system serves the purpose of integrating all the primitive three level atomic systems, *i.e.*, Λ, ladder and vee, along with two of the basic four level atomic system, namely, inverted-Y system and N-system. The proposed atomic system is shown in Fig. 4.2 (b). The parametrs of applied electromagnetic fields are their coupling strength Ω_{ij}, and detuning Δ_{ij}, where i and j represent the states i and j coupled via an electromagnetic field. In the IY^+-system, the transitions forming Λ system are $|0\rangle \longleftrightarrow |2\rangle \longleftrightarrow |1\rangle$, ladder system are $|0\rangle \longleftrightarrow |2\rangle \longleftrightarrow |3\rangle$ and vee system are $|2\rangle \longleftrightarrow |0\rangle \longleftrightarrow |4\rangle$. The involving transitions to form inverted-Y system are $|0\rangle \longleftrightarrow |2\rangle \longleftrightarrow |3\rangle$ and $|1\rangle \longleftrightarrow |2\rangle \longleftrightarrow |3\rangle$ and the formation of N-system is via the transitions $|1\rangle \longleftrightarrow |2\rangle \longleftrightarrow |0\rangle \longleftrightarrow |4\rangle$. The field with strength Ω_{02} and detuning Δ_{02} for the transition $|0\rangle \longleftrightarrow |2\rangle$ is a probe field, which can simultaneously probe the response of all the above systems. To identify the key spectral features of the IY^+-system, the coherence $\Im(\rho_{02})$ of the density matrix is calculated under different conditions. If not explicitly described, the field values used in calculation are: $\Omega_{02} = 1.0\gamma$, $\Omega_{12} = 5.0\gamma$, $\Omega_{23} = 5.0\gamma$ and $\Omega_{04} = 5.0\gamma$. The detuning of probe field Δ_{02} has been varied in a wide range $-100\gamma \longleftrightarrow 100\gamma$, and the relevant part of

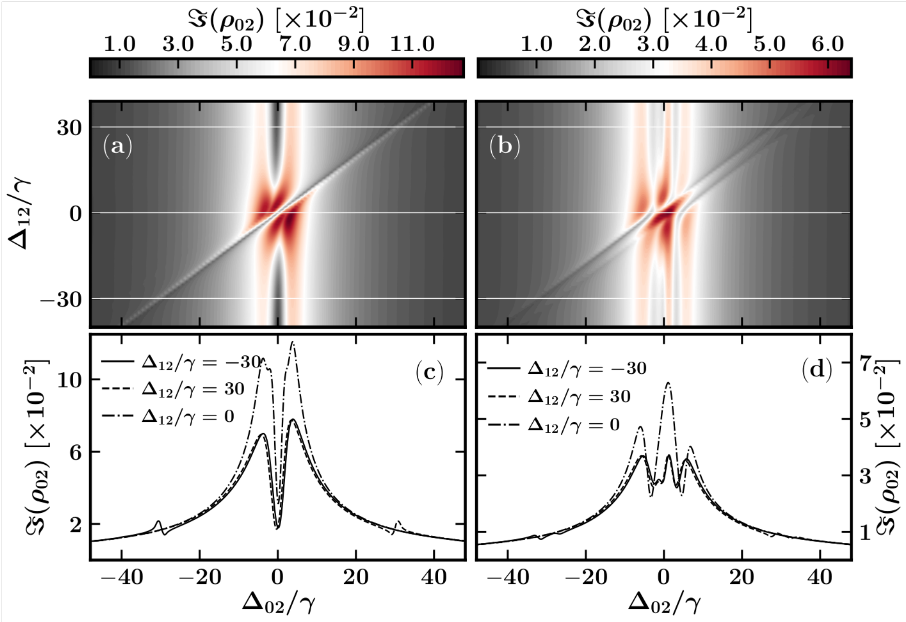

Figure 4.5: Amalgamated probe absorption spectrum (*i.e.* probe absorption versus detuning Δ_{02}) as a function of the scaled detuning Δ_{12} for (a) inverted-Y system with $\Omega_{02} = 1.0\gamma$, $\Omega_{12} = 5.0\gamma$, $\Omega_{23} = 5.0\gamma$, $\Delta_{23} = 0$ and (b) IY^{+}-system with $\Omega_{02} = 1.0\gamma$, $\Omega_{12} = 5.0\gamma$, $\Omega_{23} = 5.0\gamma$, $\Omega_{04} = 5.0\gamma$, $\Delta_{23} = 0$, $\Delta_{04} = 0$. (c) and (d) show spectra corresponding to white lines drawn in plots (a) and (b) respectively, *i.e.,* for $\Delta_{12} = -30\gamma, 0, 30\gamma$
.

the spectral response are depicted in the various plots.

4.4.1 Dependence on detuning Δ_{12} and comparison of IY^{+} system with IY-system

To begin with, the spectral features of the inverted-Y system and the IY^{+}-system are compared to see the effect of additional coupling field connecting ground state $|0\rangle$ and excited state $|4\rangle$ in IY^{+}-system. For this comparative study, the detuning Δ_{12} has been varied in a range of -40γ to 40γ for both the inverted-Y and IY^{+} systems. The obtained results are depicted in Fig 4.5. Fig 4.5 (a) and (b) presents the amalgamated probe transmission spectrum for inverted-Y and IY^{+} systems respectively. Plots (c) and (d) show the individual spectrum corresponding to the white lines drawn in plots (a) and (b) respectively. For the inverted-Y system (Fig 4.2 (a)), the spectral response has shown two EIT features at the detuning positions where the two-photon resonance condition of the Λ-system ($|0\rangle \longleftrightarrow |2\rangle \longleftrightarrow |1\rangle$) and ladder-system ($|0\rangle \longleftrightarrow |2\rangle \longleftrightarrow |3\rangle$) are satisfied. A similar feature is reported in the earlier studies [25]. For the case of resonant coupling fields, these two EIT features merge and gives a single sharp EIT at resonance. The coupling of a field with strength Ω_{04} connecting the ground state $|0\rangle$ and excited state $|4\rangle$ in the IY^{+}-system (Fig 4.2 (b)) has shown different spectral features than that of inverted-Y system.

For detuning $\Delta_{12} = 0$, Fig 4.5 (b) shows larger value of $\Im(\rho_{02})$ (encoded by red color) at resonant probe field frequency, indicating the existence of an absorption peak rather than a transparency dip as obtained for the case of inverted-Y system.

A qualitative understanding of such change in behavior of spectral features from inverted-Y to IY^{+}-system can be obtained using a semi-classical dressed state approach as explained in the following discussion. In this approach, a new atom-photon basis state (*i.e.,* dressed state) forms when a strong field coupled with the bare states. The dressed states can be obtained by diagonalizing the interaction Hamiltonian. Considering the case of resonant driving fields, the Hamiltonian of the inverted-Y system after RWA and dipole approximation can be written as,

$$H_1 = \frac{1}{2}\begin{bmatrix} 0 & 0 & \Omega_{02} & 0 \\ 0 & 0 & \Omega_{12} & 0 \\ \Omega_{02} & \Omega_{12} & 0 & \Omega_{23} \\ 0 & 0 & \Omega_{23} & 0 \end{bmatrix}. \tag{4.16}$$

Since the probe field strength Ω_{02} is weaker than all other coupling fields strengths, we can neglect the probe field while obtaining the eigen states (*i.e.,* dressed states) of the Hamiltonian H_I in equation (4.16). The resulting three eigen-energies and their corresponding dressed states are

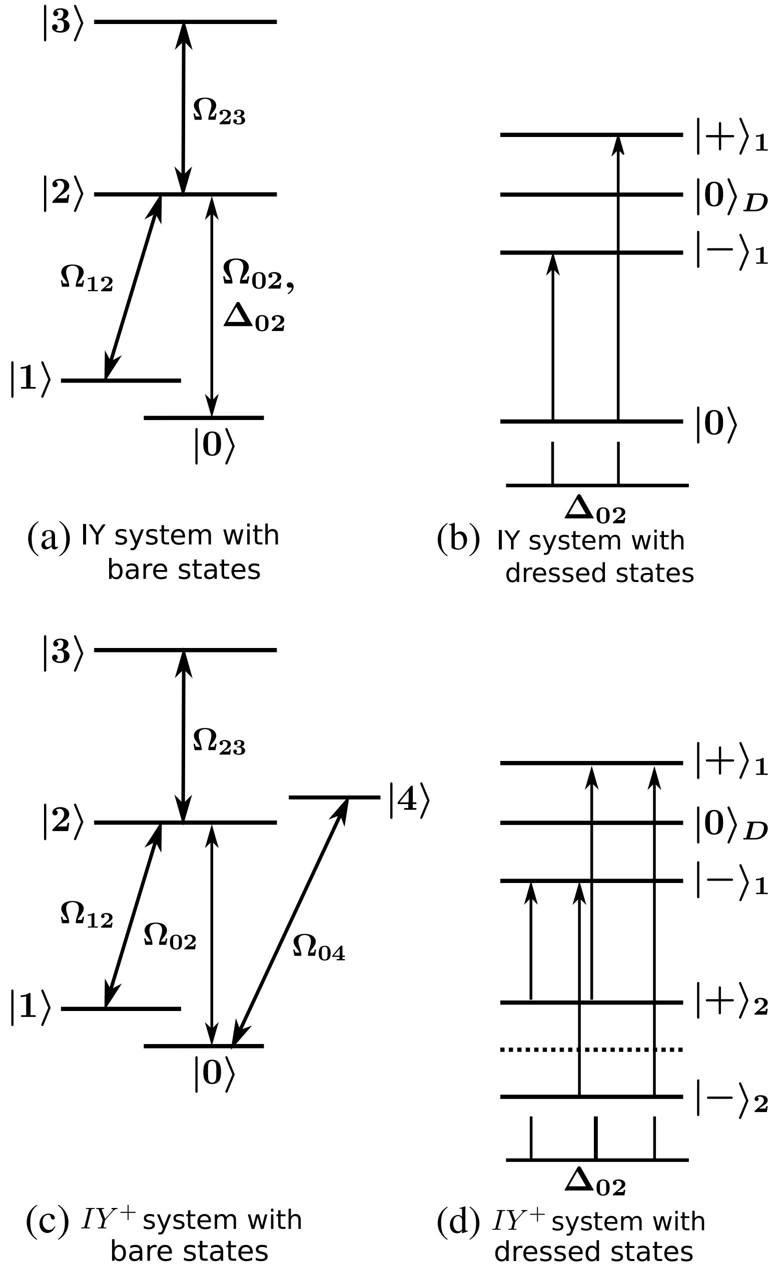

Figure 4.6: (a) and (c) show bare states interacting with resonant coupling fields. (b) and (d) show dressed states of inverted-Y (IY) and IY^{+}-systems.

$$\lambda_{0,\pm} = 0, \pm\frac{1}{2}\sqrt{\Omega_{12}^2 + \Omega_{23}^2}$$

$$|0\rangle_D = \frac{\Omega_{23}}{\sqrt{\Omega_{12}^2+\Omega_{23}^2}}|1\rangle - \frac{\Omega_{12}}{\sqrt{\Omega_{12}^2+\Omega_{23}^2}}|3\rangle$$

$$|+\rangle_1 = \frac{\Omega_{12}}{\sqrt{2(\Omega_{12}^2+\Omega_{23}^2)}}|1\rangle + \frac{1}{\sqrt{2}}|2\rangle + \frac{\Omega_{23}}{\sqrt{2(\Omega_{12}^2+\Omega_{23}^2)}}|3\rangle$$

$$|-\rangle_1 = \frac{\Omega_{12}}{\sqrt{2(\Omega_{12}^2+\Omega_{23}^2)}}|1\rangle - \frac{1}{\sqrt{2}}|2\rangle + \frac{\Omega_{23}}{\sqrt{2(\Omega_{12}^2+\Omega_{23}^2)}}|3\rangle.$$

The transition probabilities of probe transition from ground state $|0\rangle$ to upper dressed states $|+\rangle_1$ and $|-\rangle_1$ should be determine in order to understand the process of absorption in this approach. The transition probability can be expressed as,

$$T_{\alpha\to\beta} = |\langle\alpha|\vec{d}\cdot\vec{E_0}|\beta\rangle|^2, \tag{4.17}$$

where α is ground state, and $\beta \in \{|-\rangle_1, |0\rangle_D, |+\rangle_1\}$. This is schematically shown in Fig 4.6 (a) and (b). Due to zero transition probability of transition between states $|0\rangle$ and $|0\rangle_D$ (*i.e.* $|\langle 0|\vec{d}\cdot\vec{E_0}|0\rangle_D|^2 = 0$), there is no absorption possible at resonant probe detuning (*i.e.* $\Delta_{02} = 0$). However, the transition probabilities of other transitions (*i.e.* between states $|0\rangle$ and $|\pm\rangle_1$) are non-zero. As a result, the inverted-Y system exhibits EIT at zero probe detuning (*i.e.,* line center) along with the two absorption peaks surrounding the line center as shown in Fig 4.5 (c).

In the IY^+-system, a strong field Ω_{04} couples the ground state $|0\rangle$ with a state $|4\rangle$ which results in conversion of the bare ground state into dressed states as shown in Fig 4.6 (d). Thus, the total dressed states for IY^+-system are three upper dressed states $|-\rangle_1, |0\rangle_D, |+\rangle_1$ similar to the case of inverted-Y system, and two lower dressed states $|-\rangle_2, |+\rangle_2$ formed due to strong field Ω_{04} interacting with states $|0\rangle$ and $|4\rangle$. Considering the case of two-level system interacting with a resonant coupling field of strength Ω_{04}, the lower dressed states can be obtained by diagonalizing Hamiltonian of this system. The Hamiltonian after applying RWA and dipole approximation is,

$$H_2 = \frac{1}{2}\Omega_{04}|0\rangle\langle 4| + h.c.$$

The eigen-energies are $\lambda_2 = \pm\frac{1}{2}\Omega_{04}$ and corresponding eigen dressed states are

$$|+\rangle_2 = \frac{1}{\sqrt{2}}|0\rangle + \frac{1}{\sqrt{2}}|4\rangle.$$

$$|-\rangle_2 = \frac{1}{\sqrt{2}}|0\rangle - \frac{1}{\sqrt{2}}|4\rangle.$$

As there is no component of bare state $|2\rangle$ in the upper dressed state $|0\rangle_D$, the transition probabilities of transition to state $|0\rangle_D$ (*i.e.,* $T_{|+\rangle_2\rightarrow|0\rangle_D}$ and $T_{|-\rangle_2\rightarrow|0\rangle_D}$) are zero. Whereas, the other transitions have non-zero transition probabilities as shown in Fig 4.6 (d). The position of each transitions are calculated where the existence of absorption peaks in the frequency space are expected. These locations are at $\Delta_{02} = -6.0\gamma, -1.0\gamma, 1.0\gamma, 6.0\gamma$.

Among four absorption peaks, the absorption peaks at $\Delta_{02} = -1\gamma$ and 1γ are very close to each other which merges and results in a single broad absorption peak. Hence, there exist three absorption peaks in the probe absorption spectrum as shown in Fig 4.5 (d). The non-zero detuning Δ_{12} leads to a detuned Λ-system. This detuned Λ-system gives EIT dip at position where two-photon resonance condition is satisfied along with an additional absorption peak near zero probe field detuning [102]. Consequently, there exist an EIT feature at off resonant probe detuning and four absorption peaks at resonance. As the eigenvalues and dressed states are actually function of strengths and detuning of all the coupling fields, their variations can result in a change in location of spectral features and their strength as well.

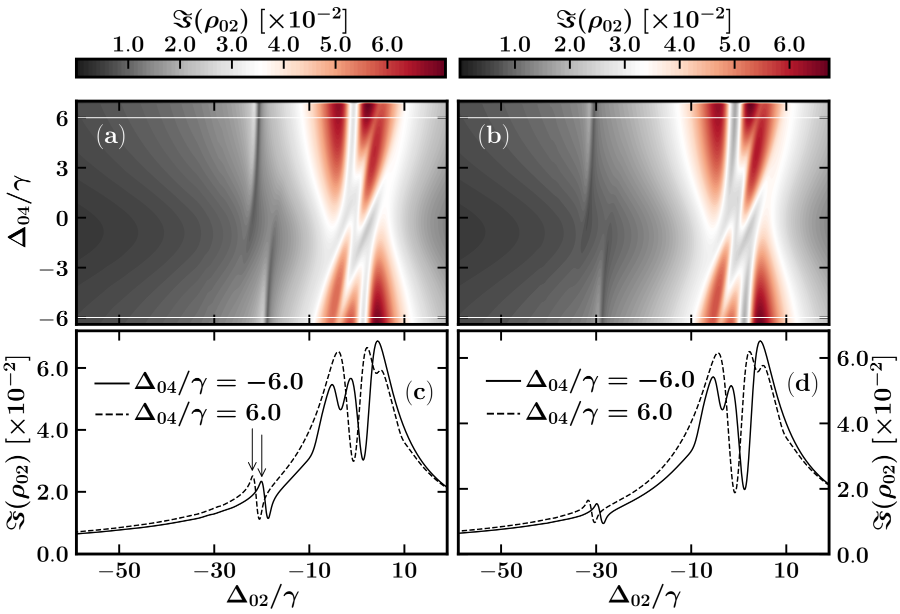

Figure 4.7: Amalgamated probe absorption spectrum (*i.e.* probe absorption versus detuning Δ_{02}) versus detuning Δ_{04} for (a) $\Delta_{12} = -20\gamma$ and (b) $\Delta_{12} = -30\gamma$. The other parameters used in simulations are $\Omega_{02} = 1.0\gamma$, $\Omega_{12} = 5.0\gamma$, $\Omega_{23} = 5.0\gamma$, $\Omega_{04} = 5.0\gamma$, $\Delta_{23} = 0$. The plots (c) and (d) show the probe absorption spectra corresponding to white lines drawn in plots (a) and (b), *i.e.,* for values of $\Delta_{04} = -6.0\gamma$ and 6.0γ.

4.4.2 Dependence on detuning Δ_{04}

For the rest of studies, the value of detuning Δ_{12} was kept large so that the Λ-system becomes far detuned and its effect can be separated while investigating the effect of other systems on the spectral response. The spectral features of IY^+-system were further investigated with the variation in detuning Δ_{04} of another coupling field, and the corresponding absorption spectra for $\Delta_{12} = -20\gamma$ and -30 are shown in in left and right column of Fig 4.7 respectively. The EIT feature of far-detuned Λ-system shows shift with the change in detuning Δ_{04} (as indicated by arrows in Fig 4.7 (c)). This may be because the coupling field with strength Ω_{04} directly couples the ground state $|0\rangle$ with the excited state $|4\rangle$ and can modify the coherence between the two ground states $|0\rangle$ and $|1\rangle$. Similarly, the dependence of the field detuning Δ_{04} on the resonant spectral features is also obtained. For non-zero values of Δ_{04}, there exist three absorption peaks with sharp transparencies between them near the probe resonance frequency, in contrast to the four absorption peaks for resonant case of Δ_{04}. For zero detuning Δ_{04}, the emergence of absorption peak at resonance could be result of constructive quantum interference in the vee sub-system [103, 104]. As the detuning Δ_{04} increases, the effective coupling of strong field between states $|0\rangle$ and $|4\rangle$ reduces which consequently reduce the constructive quantum interference effect. This results in the appearance of transparency with far detuned Δ_{04} cases in Figs 4.7 (c) and (d). On comparing Figs 4.7 (a) and (b) or (c) and (d), one can obtain the effect of detuned Λ-system the IY^{+}-system. The detuned Λ-system affects the spectral features only in terms of its strength. This detuning Δ_{04} dependent study suggests that the probe absorption features can be considerably tailored and transparency can be obtained.

4.4.3 Dependence on detuning Δ_{23}

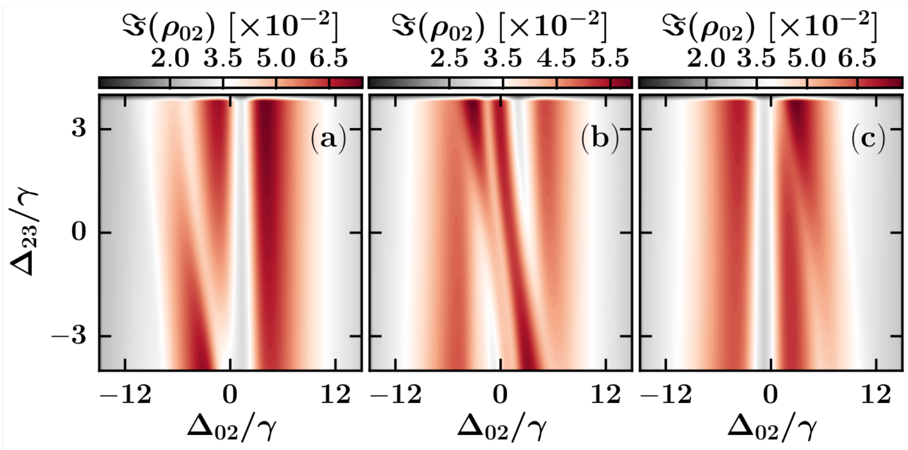

Figure 4.8: Amalgamated probe absorption spectrum with different scaled detuning Δ_{23} for (a) $\Delta_{04} = -6\gamma$, (b) $\Delta_{04} = 0$ and (c) $\Delta_{04} = 6\gamma$. The other parameters used in simulation are $\Omega_{02} = 1.0\gamma$, $\Omega_{12} = 5.0\gamma$, $\Omega_{23} = 5.0\gamma$, $\Omega_{04} = 5.0\gamma$ and $\Delta_{12} = -20\gamma$.

The spectral response of IY^{+}-system is further investigated with the variation in the detuing of another coupling field Δ_{23} in three different conditions, *i.e.,* with detuning parameter $\Delta_{04} = -6\gamma, 0$ and 6γ. As in previous study (Fig 4.7), a contrasting specral features for these detuning values have been observed, hence a Δ_{23} dependent study is performed with $\Delta_{04} = -6\gamma, 0$ and 6γ. The obtained results are shown in Fig 4.8. Due to no decay channel from excited state $|3\rangle$ to ground state $|0\rangle$ directly, the coherence between two ground states

$|0\rangle$ and $|1\rangle$ (which is responsible for detuned EIT feature) does not significantly change with the variation in Δ_{23}. This results in negligible change in EIT dip at detuned position with the variation in Δ_{23} and hence this part of spectral response is not shown in Fig 4.8. Whereas, a significant change in the resonant spectral features with the change in detuning Δ_{23} has been obtained under all the three conditions *i.e.,* $\Delta_{04} = -6\gamma, 0$ and 6γ.

Fig 4.8 (a), (b) and (c) shows the spectrum for $\Delta_{04} = -6\gamma, 0$ and 6γ respectively. In the previous study, a non-zero Δ_{04} has resulted in three absorption peaks. In this study, two of the absorption peaks exhibit variation in its strength with detuning Δ_{23}, while the third absorption peak has been observed to be independent of detuning Δ_{23}. The location of these peaks depends on positive or negative values of detuning Δ_{04}. This is clearly visible in Fig 4.8 (a) and (c), where the position of these peaks are swapped in plots (a) and (c). For the far detuned values of Δ_{04}, *i.e.* $\Delta_{04} = \pm 6\gamma$ (Fig 4.8 (a) and (c)), a single transparency dip appears at a particular probe field frequency which does not change with the values of detuning Δ_{23}. The independency of this transparency with the detuning Δ_{23} shows that this is not the consequence of interference effect of ladder sub-system but may be result of vee sub-system as it shifts with the change in sign of Δ_{04}. This is the same transparency which has been observed in Fig 4.7 near zero probe field detuning and discussed previously. In Fig 4.8 (a) and (c), there also exists a second transparency at detuned position which shifts with change in detuning Δ_{23}. This shows that this transparency is due to EIT effect of ladder system. Due to weak coupling of fields with Rabi frequencies Ω_{12} and Ω_{04}, the system is dominated by ladder system and Double resonance optical pumping (DROP) could be effective in such case [105]. But, for our choice of parameter, the two transparancies seems to be dominated by quantum interference effect than the DROP effect. For the case of $\Delta_{04} = 0$ (Fig 4.8 (b)), four absorption peaks appears when $\Delta_{23} = 0$. As the detuning Δ_{23} varies, central peak shifts in its position and another central peak changes its strength and position as well. Along with this, a sharp transparency window begins to appear as the detuning Δ_{23} value is increased in either positive or negative side. This transparency shifts in negative side as the coupling field of ladder sub-system (*i.e.* Δ_{23}) changes towards positive side and vice-versa. This shows that the transparency could be consequence of destructive quantum interference due to ladder sub-system prepared by $|0\rangle \rightarrow |2\rangle \leftarrow |3\rangle$. This study concludes that with the appropriate value of Δ_{23}, the strength of the absorption peaks can be tailored. In addition, a strong transparency can be attained with non-zero value of detuning Δ_{04}. These spectral features of the IY^+-system can be utilized for developing optical switching devices.

4.4.4 Dependence of probe absorption on strength Ω_{12} in IY^+-system

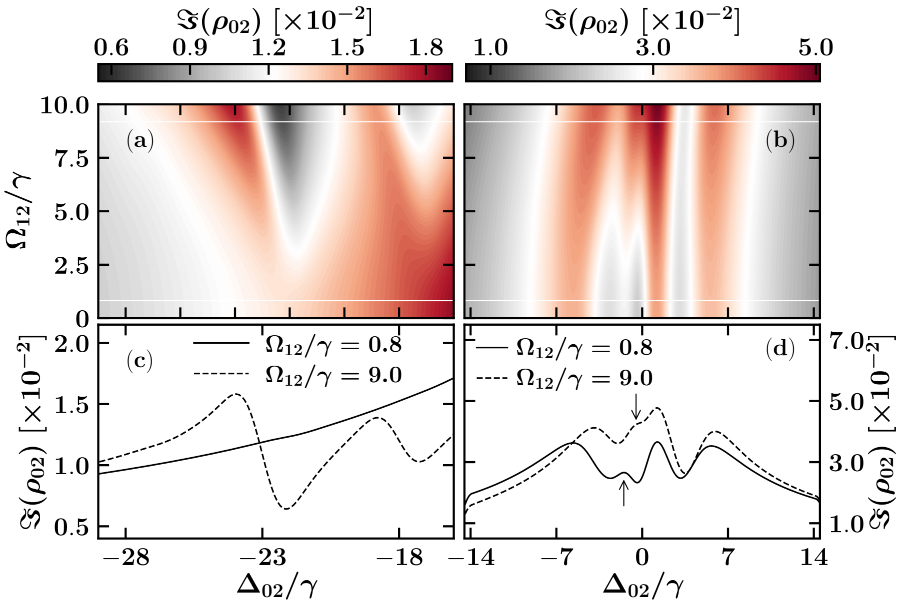

Figure 4.9: Amalgamated probe absorption spectrum for different values of coupling field strength Ω_{12}. The other parameters are $\Omega_{02} = 1.0\gamma$, $\Omega_{23} = 5.0\gamma$, $\Omega_{04} = 5.0\gamma$, $\Delta_{12} = -20\gamma$, $\Delta_{23} = \Delta_{04} = 0$. The left plot correspond to the negative detuning case and right plots show resonant spectral features respectively. Plots (c) and (d) presents spectra for strengths Ω_{12} marked by the white lines in plots (a) and (b).

After the studies on effect of detuning, the dependence of spectral features on the strength of all the coupling fields have also been studied. The probe absorption spectrum of IY^+-system with the coupling field strength Ω_{12} is presented in Fig 4.9. The EIT dip corresponding to the detuned Λ-system (*i.e.,* at $\Delta_{02} = -20\gamma$) does not appear for weak field strength Ω_{12}. It appears to emerge with increase in field strength Ω_{12}. Also, the spectral features near resonance depends on the strength Ω_{12}. With increase in coupling field strength Ω_{12}, the small central absorption peak (shown by an arrow in Fig 4.9 (d)) that appears due to the detuned Λ-system, merges with the other peaks as shown in Fig 4.9 (b) and (d).

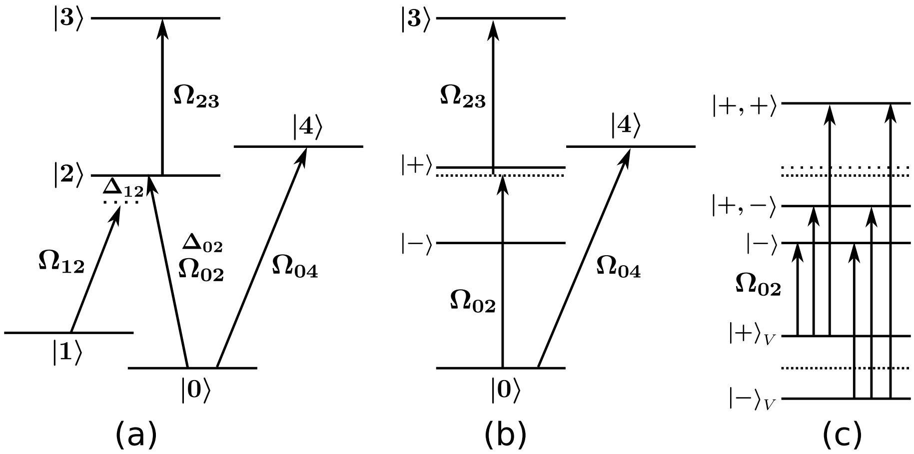

Figure 4.10: The double dressing of IY^+-system. (a) Bare states of IY^+-system. (b) Due to strong coupling of Ω_{12}, the formation of primary dressed states. (c) The formation of secondary dressed states and the allowed transitions from ground states to excited states.

The obtained results, for the case of $\Omega_{ij} > \Omega_{lm}$ where $ij, lm \in \{12, 23\}$, can be explained using the doubly dressed approach [46]. In this approach, initially, the bare atomic states coupled with strongest coupling field generates primary dressed states. One of these primary dressed states get further dressed due to its coupling with another bare state through a strong coupling field. Considering a particular case for $\Omega_{12} = 9\gamma, \Omega_{23} = \Omega_{04} = 5\gamma, \Omega_{02} = 1\gamma, \Delta_{12} = -20\gamma$ and $\Delta_{23} = \Delta_{04} = 0$ (Fig 4.9 (d)). The strong field of strength Ω_{12} coupling states $|1\rangle$ and $|2\rangle$ creates primary dressed states $|-\rangle$ and $|+\rangle$ (as shown in Fig 4.10 (b)) with energies $\frac{1}{2}(\Delta_{12} - \Omega_{12}^{'})$ and $\frac{1}{2}(\Delta_{12} + \Omega_{12}^{'})$ respectively, where $\Omega_{12}^{'} = \sqrt{\Delta_{12}^2 + \Omega_{12}^2}$. The bare state $|3\rangle$ couples with the dressed state $|+\rangle$ via the strong field Ω_{23} which produce secondary dressed states $|+,-\rangle$ and $|+,+\rangle$ with energy $\frac{1}{2}(\Delta^{'} - \sqrt{\Delta^{'2} + \Omega_{23}^2})$ and $\frac{1}{2}(\Delta^{'} + \sqrt{\Delta^{'2} + \Omega_{23}^2})$ respectively, where $\Delta^{'} = \frac{1}{2}(\Delta_{12} + \Omega_{12}^{'})$ as shown in Fig 4.10 (c). As observed in Fig 4.10 (c), a total of six transitions are possible via probe field Ω_{02} between the dressed states formed by the ground state manifold and the excited state manifold resulting in transitions at $\Delta_{02} = -23.4\gamma, -18.4\gamma, -3.7\gamma, 1.3\gamma, 1.4\gamma$ and 6.4γ, which are in agreement with the results obtained through the NMP method [shown by dashed line in Fig 4.9 (c) and (d)].

4.4.5 Dependence of probe absorption on strength Ω_{04} in IY^{+}-system

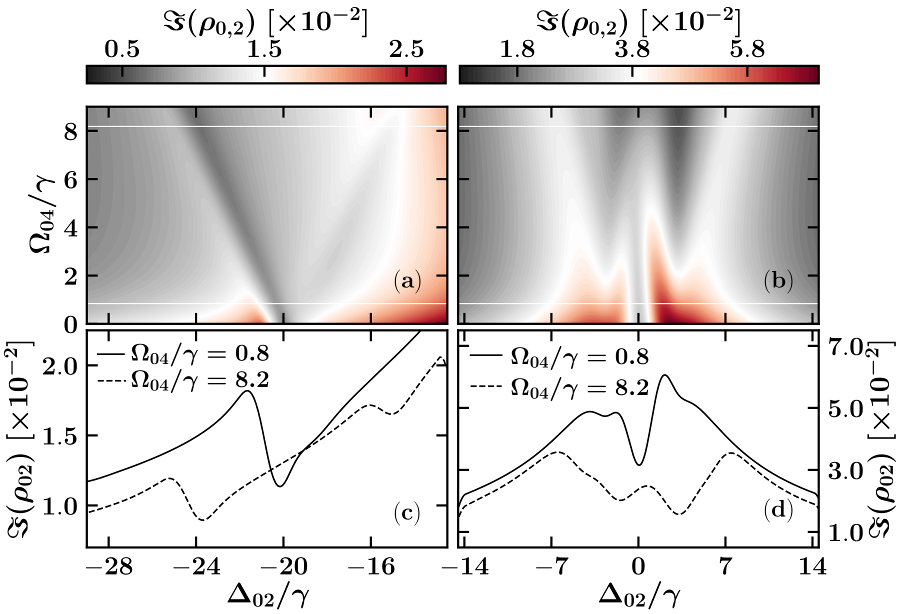

Figure 4.11: Amalgamated probe absorption spectrum as a function of scaled coupling strength Ω_{04}. (a) shows far detuned spectral features and (b) shows resonant spectral features. Plots (c) and (d) represents spectrum corresponding to the specific field strengths marked by the white lines in plots (a) and (b). The other parameters used in simulation are $\Omega_{02} = 1.0\gamma$, $\Omega_{12} = 5.0\gamma$, $\Omega_{23} = 5.0\gamma$, $\Delta_{04} = \Delta_{23} = 0$ and $\Delta_{12} = -20\gamma$.

The probe absorption characteristics depending on the variation in coupling field strength Ω_{04} has also been investigated and the corresponding spectrum is plotted in Fig 4.11. For a weak coupling field strength Ω_{04}, *i.e.* $\Omega_{04} = 0.8\gamma$, a large dispersive EIT feature emerges at the detuned position fixed by the detuning value Δ_{12}. As the field strength Ω_{04} is increased, this large EIT feature splits into two smaller EIT features and the separation between these two EIT increases with further increase in the field strength Ω_{04} (Fig 4.11 (a) and (c)). The effect of strength Ω_{04} on the EIT feature at detuned location shows that the coherence between two ground states $|0\rangle$ and $|1\rangle$ is modified by the field strength

Ω_{04}. This is possible because this field is directly coupled with the ground state $|0\rangle$. The increase in the separation can be attributed to a shift in the location of the allowed transitions in the dressed state approach due to increase in the coupling strength Ω_{04}.

On considering the resonance spectra of the probe absorption, a considerable modification has been observed with the variation in the strength of the coupling field. As visible from the Fig 4.11 (d), a large transparency at weak strength of coupling field is transformed into the absorption peak at strong coupling field strength Ω_{04}. This is consistent with the results obtained during the study of effect of detuning Δ_{04} on probe spectral features in Fig 4.7, where the absorption existing for strongly coupled case (at $\Delta_{04} = 0$) got converted into transparency for weakly coupled case (at large value of Δ_{04}). The observed broad transparency, within which this absorption peak emerges, could be a result of saturation effect, *i.e.,* the population from the ground state $|0\rangle$ gets depleted due to the strong coupling Ω_{04}.

4.4.6 Dependence of probe absorption on strength Ω_{23}

The dependence of probe absorption on the coupling strength Ω_{23} has been investigated for two different cases, *i.e.* resonant and off resonant detuning values of Δ_{04}. The results of this study are shown in Fig 4.12. For the case of $\Delta_{04} = 0$, splitting of absorption peaks in the central region of probe absorption spectrum is observed with increase in strength Ω_{23}. When coupling strength Ω_{23} is weak, this coupling field acts as a perturbation and the IY^+-system becomes perturbed N-system. The probe absorption spectrum of this perturbed N-system is shown by the black continuous curve in Fig 4.12 (c). Similar spectral feature is reported earlier for the case of N-system [106]. When the coupling strength Ω_{23} is comparable to the strengths of other coupling fields, this perturbed N-system converts into IY^+-system and show four absorption peaks in the probe absorption spectrum(shown in Fig 4.12 (a)) as obtained earlier (shown by solid curve in Fig 4.5 (d)).

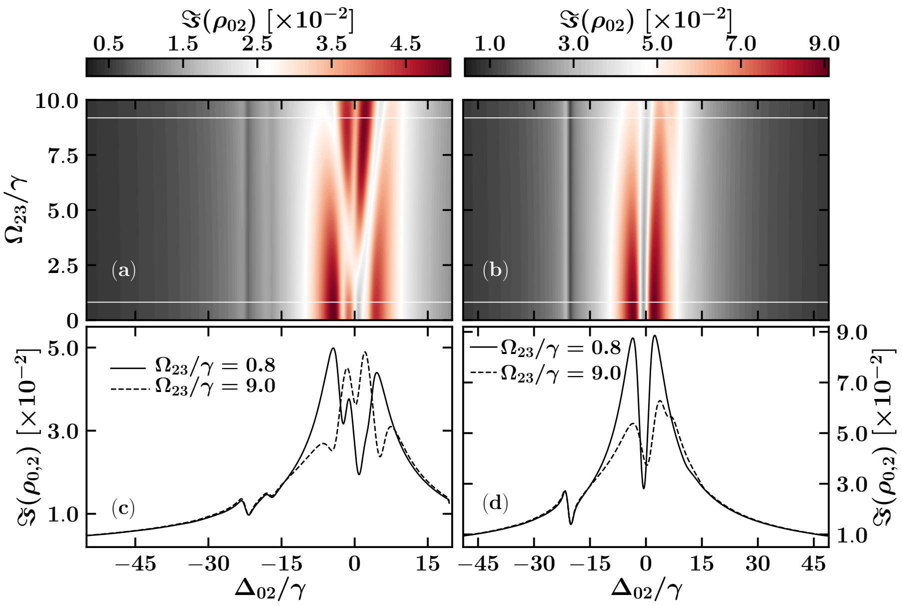

Figure 4.12: Amalgamated probe absorption spectrum for different coupling strength Ω_{23}. (a) shows spectral fetures for case $\Delta_{04} = 0$ and (b) shows spectral features for case $\Delta_{04} = 10\gamma$. The other parameters used in simulations are $\Omega_{02} = 1.0\gamma$, $\Omega_{12} = 5.0\gamma$, $\Omega_{04} = 5.0\gamma$, $\Delta_{12} = -20\gamma$ and $\Delta_{23} = 0$.

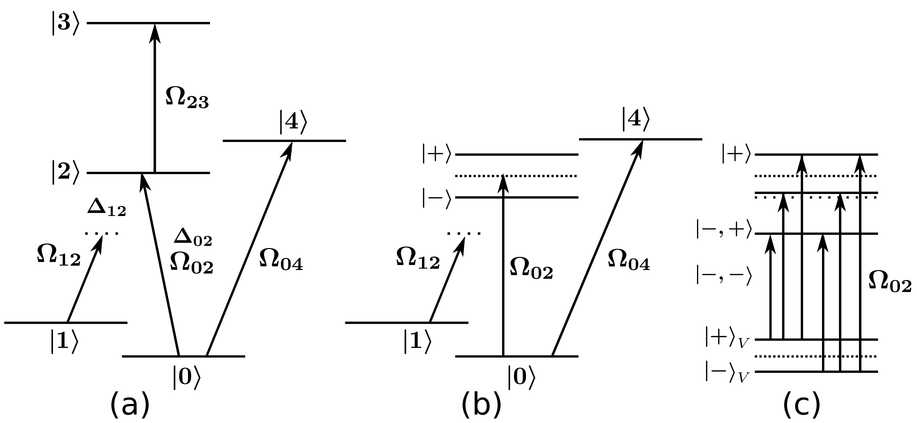

Figure 4.13: Depiction of doubly dressed approach. Plot a) displays a level diagram of the IY^+ system. Plot (b) correspond to the formation of primary dressed states due to strong coupling of Ω_{23} with states $|2\rangle$ and $|3\rangle$. (c) The formation of secondary dressed states and the allowed transitions between the ground and excited dressed states.

For the case of Ω_{23} greater than the strength of the other coupling fields, the obtained spectral features can be explained using the doubly dressed state approach. In this case, the strongest field strength is Ω_{23} coupling the bare states $|2\rangle$ and $|3\rangle$. The primary dressed states are created by field Ω_{23} with eigen-energies $\pm\Omega_{23}/2$. The dressed state with energy $-\Omega_{23}/2$ gets doubly dressed due to its interaction with the strong field Ω_{12}. The energy of these doubly dressed states are $\frac{\Delta_{12}+\Omega_{23}/2}{2} \pm \frac{\sqrt{(\Delta_{12}+\Omega_{23}/2)^2+\Omega_{12}^2}}{2}$ (see Fig 4.13). The location of the allowed transitions between two lower dressed states and three upper dressed states in the frequency space is calculated and are expected to be at $\Delta_{02} = -22.8\gamma, -17.8\gamma, -6.6\gamma, -1.5\gamma, 2.0\gamma, 7.0\gamma$. These locations of transitions are in agreement with the obtained results using NMP method (Fig 4.12 (c)). The structure of central spectral feature does not change with the change in strength Ω_{23} for the case of off-resonant detuning condition $\Delta_{04} = 10\gamma$. In this case, the effect of strength Ω_{23} is only on the amplitude of absorption peaks. Due to the far detuned Δ_{04} value, the effective coupling of the field with strength Ω_{04} become weak and the IY^+-system becomes closer to inverted-Y system. The obtained results for this case are similar to that of inverted-Y system, *i.e.* one EIT is corresponding to detuned Λ-system and another EIT is corresponding to ladder system at resonance. When strength Ω_{23} is increased, the EIT due to ladder system broadens and results in reduced strength of surrounding peaks.

4.5 Conclusion

In this chapter, spectral features of a five-level modified inverted-Y system, *i.e.* IY^+-system, is investigated. The IY^+-system comprises of basic three-level sub-systems, *i.e.* Λ-, ladder- and vee-systems, and two basic four-level sub-systems, *i.e.* N and inverted-Y, all of which can exhibit EIT feature. The investigation of probe absorption characteristics of this system has been carried out using a numerical matrix propagation (NMP) method. The supremacy of NMP method over RWA method has been established by comparing the spectral features of inverted-Y system calculated using NMP and RWA methods for the validity and beyond validity regimes of RWA. The presence of a strong coupling field connecting the ground state $|0\rangle$ to another state $|4\rangle$ in the IY^+ atomic system leads to conversion of resonant probe transparency (obtained in the inverted-Y system) into absorption. With the off-resonant frequency of the aforementioned coupling field or its weak strength, the transparency in IY^+-system is recovered.

Along with this, the splitting in the transparency depending on the coupling field detuning and shifting and splitting of the absorption depending on the coupling field strength have also been obtained for the IY^+-system. The dressed and doubly dressed state approach explains the numerically obtained results. The obtained spectral features of the IY^+-system can be utilized to design multi-channel optical communication and optical switching devices.

Appendix A

Derivation of Hamiltonian under Rotating Wave Approximation

In this appendix, the derivation of the Hamiltonian for two-level atomic system interacting with a probe field (as shown in Fig 1.2) under rotating-wave approximation is carried out. To begin with, the total Hamiltonian of a two-level system is expressed in matrix form in the basis of ground state $|1\rangle$ and excited state $|2\rangle$ as,

$$\mathcal{H} = \begin{pmatrix} \hbar\omega_1 & -\mu_{12}E \\ -\mu_{21}E & \hbar\omega_2 \end{pmatrix}. \tag{A.1}$$

Here μ_{ij} is the element of dipole moment and E represents the electric field of the probe field in the medium. The diagonal terms show unperturbed Hamiltonian and off-diagonal term shows interaction Hamiltonian. The electric field E can be expressed as,

$$E = \frac{E_p}{2}(e^{i\omega_p t} + e^{-i\omega_p t}). \tag{A.2}$$

We should transform the Hamiltonian into interaction picture using a time evolution operator $U(t)$,

$$U(t) = e^{i\mathcal{H}_0 t/\hbar} = \begin{bmatrix} e^{i\omega_1 t} & 0 \\ 0 & e^{i\omega_2 t} \end{bmatrix}, \tag{A.3}$$

where $\mathcal{H}_0$ is the unperturbed Hamiltonian of the system. The transformation of Hamiltonian can be obtained as,

$$U\mathcal{H}U^{+} = \begin{bmatrix} \hbar\omega_1 & -\mu_{12}Ee^{-i(\omega_2-\omega_1)t} \\ -\mu_{21}Ee^{i(\omega_2-\omega_1)t} & \hbar\omega_2 \end{bmatrix}. \tag{A.4}$$

Using equation (A.2) in the above transformed Hamiltonian, we obtain,

$$U\mathcal{H}U^{+} = \frac{1}{2}\begin{bmatrix} 2\hbar\omega_1 & -\mu_{12}E_p[e^{-i(\omega_2-\omega_1+\omega_p)t} + e^{-i(\omega_2-\omega_1-\omega_p)t}] \\ -\mu_{21}E[e^{i(\omega_2-\omega_1+\omega_p)t} + e^{i(\omega_2-\omega_1-\omega_p)t}] & 2\hbar\omega_2 \end{bmatrix}. \tag{A.5}$$

The term $e^{\pm i(\omega_2-\omega_1+\omega_p)t}$ oscillates very fast such that it averages to zero rapidly. According to rotating wave approximation, such term can be ignored and keeping other term we get,

$$\mathcal{H}' = U\mathcal{H}U^{+} = \frac{1}{2}\begin{bmatrix} 2\hbar\omega_1 & -\mu_{12}E_p e^{-i(\omega_2-\omega_1-\omega_p)t} \\ -\mu_{21}E_p e^{i(\omega_2-\omega_1-\omega_p)t} & 2\hbar\omega_2 \end{bmatrix} \tag{A.6}$$

The above Hamiltonian is in interaction picture which should be transferred in Schrödinger picture with definition $\Omega = \frac{E_p|\mu_{12}|}{\hbar}$, as

$$\mathcal{H} = U^{+}\mathcal{H}'U = \frac{\hbar}{2}\begin{bmatrix} 2\omega_1 & -\Omega e^{i\omega_p t} \\ -\Omega^{*}e^{-i\omega_p t} & 2\omega_2 \end{bmatrix} \tag{A.7}$$

With a new rotating basis, *i.e.* transforming the Hamiltonian in corotating frame, the time dependence in the above Hamiltonian can be removed. The new basis and old basis are related by $|\tilde{n}\rangle = \tilde{U}(t)|n\rangle$, where $\tilde{U}$ is the unitary matrix given by,

$$\tilde{U(t)} = \begin{bmatrix} e^{-i\omega_p t} & 0 \\ 0 & 1 \end{bmatrix}. \tag{A.8}$$

The Hamiltonian in corotating frame should satisfy the Schrödinger equation, *i.e.,*

$$\begin{aligned}
\tilde{\mathcal{H}}|\tilde{n}\rangle &= i\hbar\frac{\partial}{\partial t}|\tilde{n}\rangle \\
&= i\hbar\frac{\partial}{\partial t}(\tilde{U}|n\rangle) \\
&= i\hbar(\frac{\partial \tilde{U}}{\partial t}|n\rangle + \tilde{U}\frac{\partial|n\rangle}{\partial t}) \\
&= i\hbar(\frac{\partial \tilde{U}}{\partial t}|n\rangle + \frac{-i}{\hbar}\tilde{U}\mathcal{H}|n\rangle) \\
\tilde{\mathcal{H}}|\tilde{n}\rangle &= (\frac{\partial \tilde{U}}{\partial t}\tilde{U}^{\dagger}|n\rangle + \tilde{U}\mathcal{H}\tilde{U}^{\dagger})\tilde{U}|n\rangle.
\end{aligned} \tag{A.9}$$

Following the above relation and using unitary matrix $\tilde{U}$ from equation (A.8) and Hamiltonian from equation (A.7), the Hamiltonian for two-level system in corotating frame is

$$\tilde{\mathcal{H}} = \frac{\hbar}{2}\begin{bmatrix} 2(\omega_1 + \omega_p) & -\Omega \\ -\Omega^* & 2\omega_2 \end{bmatrix} \tag{A.10}$$

A multiple of identity can be added to the Hamiltonian $\tilde{\mathcal{H}}$ without any change in physical results. On adding $-2\hbar\omega_2 I$ in the above Hamiltonian, we obtain the Hamiltonian for two-level system as,

$$\tilde{\mathcal{H}} = -\frac{\hbar}{2}\begin{bmatrix} 2\Delta_p & \Omega \\ \Omega^* & 0 \end{bmatrix}, \tag{A.11}$$

where $\Delta_p = \omega_2 - \omega_1 - \omega_p$ is detuning of the probe field.

Appendix B

Probe coherence for three-level Λ-system

This section of appendix calculates the coherence of probe field in the presence of an strong electromagnetic field, both forming three-level Λ-system. The optical Bloch equations for three-level Λ-system (shown in the Fig 1.3) is given in equation (1.41). For steady state condition, making the time derivative of density matrix element set to zero, *i.e.* $\dot{\rho_{ij}} = 0$ in equation (1.41), we obtain the following set of equations,

$$\frac{i}{2}\Omega_p(\rho_{31} - \rho_{13}) + \Gamma_1\rho_{33} = 0 \tag{B.1}$$
$$\frac{i}{2}\Omega_c(\rho_{32} - \rho_{23}) + \Gamma_2\rho_{33} = 0 \tag{B.2}$$
$$\frac{i}{2}\Omega_p(\rho_{13} - \rho_{31}) + \frac{i}{2}\Omega_c(\rho_{23} - \rho_{32}) - \Gamma\rho_{33} = 0 \tag{B.3}$$
$$(i\Delta_p + \Gamma/2)\rho_{13} + \frac{i}{2}\Omega_p(\rho_{33} - \rho_{11}) - \frac{i}{2}\Omega_c\rho_{12} = 0 \tag{B.4}$$
$$(i(\Delta_p - \Delta_c) + \gamma)\rho_{12} + \frac{i}{2}\Omega_p\rho_{32} - \frac{i}{2}\Omega_c\rho_{13} = 0 \tag{B.5}$$
$$(i\Delta_c + \Gamma/2)\rho_{23} - \frac{i}{2}\Omega_p\rho_{21} + \frac{i}{2}\Omega_c(\rho_{33} - \rho_{22}) = 0. \tag{B.6}$$

Assuming that initially all atoms reside in ground state $|1\rangle$, *i.e.* $\rho_{11} = 1, \rho_{22} = \rho_{33} = 0$. From equation (B.4), it can be written as,

$$\rho_{13} = \frac{\frac{i}{2}\Omega_p + \frac{i}{2}\Omega_c\rho_{12}}{i\Delta_p + \Gamma/2}. \tag{B.7}$$

Next, using equation (B.5) and complex conjugate of equation (B.6), we obtain

$$\rho_{12} = \frac{\frac{i}{2}\Omega_c\rho_{13}}{[i(\Delta_p - \Delta_c) + \gamma] + \frac{\Omega_p^2}{4(-i\Delta_c + \Gamma/2)}} \tag{B.8}$$

Using equation (B.8) in equation (B.7) and ignoring higher order of Ω_p as probe field is very weak, we obtain the expression of probe coherence as,

$$\rho_{13} = \frac{i\Omega_p/2}{(i\Delta_p + \Gamma/2) + \frac{\Omega_c^2}{4[i(\Delta_p - \Delta_c) + \gamma]}} \tag{B.9}$$

Appendix C

Derivation of Hamiltonian under Rotating Wave Approximation for N-system

The Hamiltonian for N-system, shown in Fig 3.1 (a), under rotating-wave approximation is derived in this section. For system N_A, the total Hamiltonian in the basis of atomic states involving the levels of the system N_A can be written in matrix form as,

$$\mathcal{H} = \begin{pmatrix} \hbar\omega_1 & 0 & -\mu_{13}E_{C_2} & -\mu_{14}E_{C_1} \\ 0 & \hbar\omega_2 & -\mu_{23}E_p & 0 \\ -\mu_{31}E_{C_2} & -\mu_{32}E_p & \hbar\omega_3 & 0 \\ -\mu_{41}E_{C_1} & 0 & 0 & \hbar\omega_4 \end{pmatrix}, \tag{C.1}$$

where μ_{ij} is the dipole moment matrix element and $E_{C_1/C_2/p}$ represents electric field corresponding to drive beam C_1, drive beam C_2 and probe beam (p). The expression of different electric fields can be written as

$$
\begin{aligned}
E_{C_2} &= \frac{\epsilon_{C_2}}{2}(e^{i\omega_{C_2}t} + e^{-i\omega_{C_2}t}) \\
E_{C_1} &= \frac{\epsilon_{C_1}}{2}(e^{i\omega_{C_1}t} + e^{-i\omega_{C_1}t}) \\
E_p &= \frac{\epsilon_p}{2}(e^{i\omega_p t} + e^{-i\omega_p t}).
\end{aligned}
\tag{C.2}
$$

The Hamiltonian of the system is to be transformed in interaction picture, for which a time evolution operator $U(t)$ is defined as,

$$
U(t) = e^{i\mathcal{H}_0 t/\hbar} = \begin{bmatrix} e^{i\omega_1 t} & 0 & 0 & 0 \\ 0 & e^{i\omega_2 t} & 0 & 0 \\ 0 & 0 & e^{i\omega_3 t} & 0 \\ 0 & 0 & 0 & e^{i\omega_4 t} \end{bmatrix}, \tag{C.3}
$$

where $\mathcal{H}_0$ is the atomic Hamiltonian of the system. The transformation of Hamiltonian can be obtained as $\mathcal{H}' = U\mathcal{H}U^+$ such that,

$$
\mathcal{H}' = \begin{bmatrix} \hbar\omega_1 & 0 & -\mu_{13}E_{C_2}e^{i(\omega_1-\omega_3)t} & -\mu_{14}E_{C_1}e^{i(\omega_1-\omega_4)t} \\ 0 & \hbar\omega_2 & -\mu_{23}E_p e^{i(\omega_2-\omega_3)t} & 0 \\ -\mu_{31}E_{C_2}e^{-i(\omega_1-\omega_3)t} & -\mu_{32}E_p e^{-i(\omega_2-\omega_3)t} & \hbar\omega_3 & 0 \\ -\mu_{41}E_{C_1}e^{-i(\omega_1-\omega_4)t} & 00 & \hbar\omega_4 & \end{bmatrix}. \tag{C.4}
$$

In this transformed Hamiltonian, the expression of electric field from equation (C.2) can be used, which results in two exponential terms like $e^{i(\omega_j-\omega_k-\omega_{C_{1/2}})t}$ and $e^{i(\omega_j-\omega_k+\omega_{C_{1/2}})t}$, with $j \in \{1,2\}$ and $k \in \{3,4\}$. According to rotating-wave approximation (RWA), the terms like

$e^{i(\omega_j-\omega_k-\omega_{C_{1/2}})t}$ can be neglected. The transformed Hamiltonian after RWA is,

$$\mathcal{H}' = U\mathcal{H}U^{+} = \frac{1}{2}\begin{bmatrix} 2\hbar\omega_1 & 0 & -\mu_{13}\epsilon_{C_2}e^{-i(\omega_3-\omega_1-\omega_{C_2})t} & -\mu_{14}\epsilon_{C_1}e^{-i(\omega_4-\omega_1-\omega_{C_1})t} \\ 0 & 2\hbar\omega_2 & -\mu_{23}\epsilon_p e^{-i(\omega_3-\omega_2-\omega_p)t} & 0 \\ -\mu_{31}\epsilon_{C_2}e^{i(\omega_3-\omega_1-\omega_{C_2})t} & -\mu_{32}\epsilon_p e^{i(\omega_3-\omega_2-\omega_p)t} & 2\hbar\omega_3 & 0 \\ -\mu_{41}\epsilon_{C_1}^{i(\omega_4-\omega_1-\omega_{C_1})t} & 00 & 2\hbar\omega_4 & \end{bmatrix} \tag{C.5}$$

With definition $\Omega_p = -\frac{\epsilon_p|\mu_{13}|}{\hbar}$, $\Omega_{C_2} = -\frac{\epsilon_{C_2}|\mu_{23}|}{\hbar}$ and $\Omega_{C_1} = -\frac{\epsilon_{C_1}|\mu_{24}|}{\hbar}$, we again transform the above Hamiltonian into Schrödinger picture as,

$$\mathcal{H} = U^{+}\mathcal{H}'U = \frac{\hbar}{2}\begin{bmatrix} 2\omega_1 & 0 & \Omega_{C_2}e^{i\omega_{C_2}t} & \Omega_{C_1}e^{i\omega_{C_1}t} \\ 0 & 2\omega_2 & \Omega_p e^{i\omega_p t} & 0 \\ \Omega^*_{C_2}e^{-i\omega_{C_2}t} & \Omega^*_p e^{-i\omega_p t} & 2\omega_3 & 0 \\ \Omega^*_{C_1}e^{-i\omega_{C_1}t} & 0 & 0 & 2\omega_4 \end{bmatrix} \tag{C.6}$$

The time dependence from above Hamiltonian can be removed by transforming the Hamiltonian in a corotating frame with a new basis, named as rotating basis. This rotating basis is defined as $|\tilde{n}\rangle = \tilde{U}(t)|n\rangle$, where $|n\rangle$ is old basis and $\tilde{U}(t)$ is the unitary matrix, given by

$$\tilde{U}(t) = \begin{bmatrix} e^{-i\omega_{C_2}t} & 0 & 0 & 0 \\ 0 & e^{-i\omega_p t} & 0 & 0 \\ 0 & 0 & 1 & 0 \\ 0 & 0 & 0 & e^{i(\omega_{C_1}-\omega_{C_2})t} \end{bmatrix}. \tag{C.7}$$

The transformation of the Hamiltonian in corotating frame can be obtained using equation (1.37) *i.e*,

$$\tilde{\mathcal{H}} = i\hbar\dot{\tilde{U}}\tilde{U}^{\dagger} + \tilde{U}\mathcal{H}\tilde{U}^{\dagger}. \tag{C.8}$$

On inserting unitary matrix $\tilde{U}$ from equation (C.7) into equation (C.8), we obtain

$$\tilde{\mathcal{H}} = \frac{\hbar}{2}\begin{bmatrix} 2(\omega_1 + \omega_{C_2}) & 0 & \Omega_{C_2} & \Omega_{C_1} \\ 0 & 2(\omega_2 + \omega_p) & \Omega_p & 0 \\ \Omega^*_{C_2} & \Omega^*_p & 2\omega_3 & 0 \\ \Omega^*_{C_1} & 0 & 0 & 2(\omega_4 - \omega_{C_1} + \omega_{C_2}) \end{bmatrix} \tag{C.9}$$

Without any loss of generality, multiple of identity can be added to the Hamiltonian $\tilde{\mathcal{H}}$. With addition of $-2\omega_3 I$, we obtain the Hamiltonian for N-system (shown in Fig 3.1 (a)) in terms of fields detuning ($\Delta_p = \omega_3 - \omega_2 - \omega_p$, $\Delta_{C_1} = \omega_4 - \omega_1 - \omega_{C_1}$ and $\Delta_{C_2} = \omega_3 - \omega_1 - \omega_{C_2}$) and Rabi frequencies (as a real parameters) as,

$$\tilde{\mathcal{H}} = \frac{\hbar}{2}\begin{bmatrix} -2\Delta_{c2} & 0 & \Omega_{c2} & \Omega_{c1} \\ 0 & -2\Delta_p & \Omega_p & 0 \\ \Omega_{c2} & \Omega_p & 0 & 0 \\ \Omega_{c1} & 0 & 0 & 2(\Delta_{c1} - \Delta_{c2}) \end{bmatrix} \tag{C.10}$$

Bibliography

[1] K.-J. Boller, A. Imamoğlu, and S. E. Harris. Observation of electromagnetically induced transparency. *Phys. Rev. Lett.*, **66**, 2593–2596, (May 1991).

[2] S. E. Harris, J. E. Field, and A. Imamoğlu. Nonlinear optical processes using electromagnetically induced transparency. *Phys. Rev. Lett.*, **64**, 1107–1110, (Mar 1990).

[3] Yong-qing Li and Min Xiao. Observation of quantum interference between dressed states in an electromagnetically induced transparency. *Phys. Rev. A*, **51**, 4959–4962, (Jun 1995).

[4] Melissa A. Guidry, Elena Kuchina, Irina Novikova, and Eugeniy E. Mikhailov. Characterization of frequency stability in electromagnetically induced transparency-based atomic clocks using a differential detection scheme. *J. Opt. Soc. Am. B*, **34**(10), 2244–2249, (Oct 2017).

[5] Koji Motomura and Masaharu Mitsunaga. High-resolution spectroscopy of hyperfine zeeman components of the sodium d1 line by coherent population trapping. *J. Opt. Soc. Am. B*, **19**(10), 2456–2460, (Oct 2002).

[6] A. Krishna, K. Pandey, A. Wasan, and V. Natarajan. High-resolution hyperfine spectroscopy of excited states using electromagnetically induced transparency. *EPL (Europhysics Letters)*, **72**(2), 221, (2005).

[7] Y. B. Kale, S. R. Mishra, V. B. Tiwari, S. Singh, and H. S. Rawat. Resolution of hyperfine transitions in metastable ^{83}Kr using electromagnetically induced transparency. *Phys. Rev. A*, **91**, 053852, (May 2015).

[8] S. C. Bell, D. M. Heywood, J. D. White, J. D. Close, and R. E. Scholten. Laser frequency offset locking using electromagnetically induced transparency. *Applied Physics Letters*, **90**(17), 171120, (2007).

[9] Charu Mishra, A. Chakraborty, Vivek Singh, S.P. Ram, V.B. Tiwari, and S.R. Mishra. Coupling field dependent quantum interference effects in a λ-system of ^{87}rb atom. *Physics Letters A*, **382**(45), 3269 – 3273, (2018).

[10] Michael M. Kash, Vladimir A. Sautenkov, Alexander S. Zibrov, L. Hollberg, George R. Welch, Mikhail D. Lukin, Yuri Rostovtsev, Edward S. Fry, and Marlan O. Scully. Ultraslow group velocity and enhanced nonlinear optical effects in a coherently driven hot atomic gas. *Phys. Rev. Lett.*, **82**, 5229–5232, (Jun 1999).

[11] Yi Chen, Xiao Gang Wei, and Byoung S. Ham. Detuned slow light in the doppler broadened multi-level d2 line of rubidium. *Opt. Express*, **17**(3), 1781–1788, (Feb 2009).

[12] Hessa M. M. Alotaibi and Barry C. Sanders. Slowing the probe field in the second window of double-double electromagnetically induced transparency. *Phys. Rev. A*, **91**, 043817, (Apr 2015).

[13] Olga Kocharovskaya, Yuri Rostovtsev, and Marlan O. Scully. Stopping light via hot atoms. *Phys. Rev. Lett.*, **86**, 628–631, (Jan 2001).

[14] Leon Karpa and Martin Weitz. A stern-gerlach experiment for slow light. *nature physics*, **2**, 332–335, (2006).

[15] F. Goldfarb, J. Ghosh, M. David, J. Ruggiero, T. ChaneliÃÍre, J.-L. Le GouÃńt, H. Gilles, R. Ghosh, and F. Bretenaker. Observation of ultra-narrow electromag-

netically induced transparency and slow light using purely electronic spins in a hot atomic vapor. *EPL (Europhysics Letters)*, **82**(5), 54002, (2008).

[16] H. Schmidt and A. Imamoglu. Giant kerr nonlinearities obtained by electromagnetically induced transparency. *Opt. Lett.*, **21**(23), 1936–1938, (Dec 1996).

[17] Huiwen Wang, David J. Goorskey, and M. Xiao. Enhanced kerr nonlinearity via atomic coherence in a three-level atomic system. *Physical review letters*, **87 7**, 073601, (2001).

[18] Hoonsoo Kang and Yifu Zhu. Observation of large kerr nonlinearity at low light intensities. *Phys. Rev. Lett.*, **91**, 093601, (Aug 2003).

[19] J. Kou, R. G. Wan, Z. H. Kang, H. H. Wang, L. Jiang, X. J. Zhang, Y. Jiang, and J. Y. Gao. Eit-assisted large cross-kerr nonlinearity in a four-level inverted-y atomic system. *J. Opt. Soc. Am. B*, **27**(10), 2035–2039, (Oct 2010).

[20] Le Van Doai, Dinh Xuan Khoa, and Nguyen Huy Bang. Eit enhanced self-kerr nonlinearity in the three-level lambda system under doppler broadening. *Physica Scripta*, **90**(4), 045502, (2015).

[21] Xu Yang, Kang Ying, Yueping Niu, and Shangqing Gong. Reversible self-kerr nonlinearity in an n-type atomic system through a switching field. *Journal of Optics*, **17**(4), 045505, (2015).

[22] Hong Liang, Yueping Niu, Li Deng, and Shangqing Gong. Enhancement of kerr nonlinearity completely without absorption. *Physics Letters A*, **381**(48), 3978 – 3982, (2017).

[23] Jin-Yue Gao, Su-Hui Yang, Dong Wang, Xiu-Zhen Guo, Kai-Xin Chen, Yun Jiang, and Bin Zhao. Electromagnetically induced inhibition of two-photon absorption in sodium vapor. *Phys. Rev. A*, **61**, 023401, (Jan 2000).

[24] Min Yan, Edward G. Rickey, and Yifu Zhu. Suppression of two-photon absorption by quantum interference. *Phys. Rev. A*, **64**, 043807, (Sep 2001).

[25] Jianbing Qi. Electromagnetically induced transparency in an inverted y-type four-level system. *Physica Scripta*, **81**(1), 015402, (2010).

[26] Dong Yan, Yi-Mou Liu, Qian-Qian Bao, Chang-Bao Fu, and Jin-Hui Wu. Electromagnetically induced transparency in an inverted-Y system of interacting cold atoms. *Phys. Rev. A*, **86**, 023828, (Aug 2012).

[27] Ali, Sabir, Ray, Ayan, and Chakrabarti, Alok. Double dark resonance in inverted y system and its application in attenuating the optical switching action. *Eur. Phys. J. D*, **70**(2), 27, (2016).

[28] Kavita Yadav and Ajay Wasan. Sub-luminal and super-luminal light propagation in inverted-y system with wavelength mismatching effects. *Physics Letters A*, **381**(37), 3246 – 3253, (2017).

[29] J. Wang, Yifu Zhu, K. J. Jiang, and M. S. Zhan. Bichromatic electromagnetically induced transparency in cold rubidium atoms. *Phys. Rev. A*, **68**, 063810, (Dec 2003).

[30] Xiang-Ming Hu, Jin-Hua Zou, Xing Li, Dan Du, and Guang-Ling Cheng. Amplitude and phase control of trichromatic electromagnetically induced transparency. *Journal of Physics B: Atomic, Molecular and Optical Physics*, **38**(6), 683–692, (mar 2005).

[31] Harshawardhan Wanare. Multicolored coherent population trapping in a Λ system using phase modulated fields. *Phys. Rev. Lett.*, **96**, 183601, (May 2006).

[32] Jiepeng Zhang, Jun Xu, Gessler Hernandez, Xiang-Ming Hu, and Yifu Zhu. Polychromatic-field-induced transparency and absorption in a three-level Λ system. *Phys. Rev. A*, **75**, 043810, (Apr 2007).

[33] Yang Liu, Jinghui Wu, Dongsheng Ding, Baosen Shi, and Guangcan Guo. Bichromatic field generation from double-four-wave mixing in a double-electromagnetically induced transparency system. *New Journal of Physics*, **14**(7), 073047, (jul 2012).

[34] R. G. Beausoleil, W. J. Munro, D. A. Rodrigues, and T. P. Spiller. Applications of electromagnetically induced transparency to quantum information processing. *Journal of Modern Optics*, **51**(16-18), 2441–2448, (2004).

[35] R. G. Beausoleil, W. J. Munro, and T. P. Spiller. Applications of coherent population transfer to quantum information processing. *Journal of Modern Optics*, **51**(11), 1559–1601, (2004).

[36] Hwang Lee, Michael Fleischhauer, and Marlan O. Scully. Sensitive detection of magnetic fields including their orientation with a magnetometer based on atomic phase coherence. *Phys. Rev. A*, **58**, 2587–2595, (Sep 1998).

[37] Michael Fleischhauer and Marlan O. Scully. Quantum sensitivity limits of an optical magnetometer based on atomic phase coherence. *Phys. Rev. A*, **49**, 1973–1986, (Mar 1994).

[38] V. I. Yudin, A. V. Taichenachev, Y. O. Dudin, V. L. Velichansky, A. S. Zibrov, and S. A. Zibrov. Vector magnetometry based on electromagnetically induced transparency in linearly polarized light. *Phys. Rev. A*, **82**, 033807, (Sep 2010).

[39] Kevin Cox, Valery I. Yudin, Alexey V. Taichenachev, Irina Novikova, and Eugeniy E. Mikhailov. Measurements of the magnetic field vector using multiple electromagnetically induced transparency resonances in rb vapor. *Phys. Rev. A*, **83**, 015801, (Jan 2011).

[40] L. Margalit, M. Rosenbluh, and A. D. Wilson-Gordon. Degenerate two-level system in the presence of a transverse magnetic field. *Phys. Rev. A*, **87**, 033808, (Mar 2013).

[41] Hong Cheng, Han-Mu Wang, Shan-Shan Zhang, Pei-Pei Xin, Jun Luo, and Hong-Ping Liu. Electromagnetically induced transparency of 87 rb in a buffer gas cell with magnetic field. *Journal of Physics B: Atomic, Molecular and Optical Physics*, **50**(9), 095401, (2017).

[42] Lijun Ma, Oliver Slattery, and Xiao Tang. Optical quantum memory based on electromagnetically induced transparency. *Journal of Optics*, **19**(4), 043001, (2017).

[43] Jason Clarke, Hongxin Chen, and William A. van Wijngaarden. Electromagnetically induced transparency and optical switching in a rubidium cascade system. *Appl. Opt.*, **40**(12), 2047–2051, (Apr 2001).

[44] Ayan Ray, Md. Sabir Ali, and Alok Chakrabarti. Optical switching in a ξ system: A comparative study on drop and eit. *The European Physical Journal D*, **67**(4), 78, (Apr 2013).

[45] Yong-qing Li and Min Xiao. Electromagnetically induced transparency in a three-level Λ-type system in rubidium atoms. *Phys. Rev. A*, **51**, R2703–R2706, (Apr 1995).

[46] Min Yan, Edward G. Rickey, and Yifu Zhu. Electromagnetically induced transparency in cold rubidium atoms. *J. Opt. Soc. Am. B*, **18**(8), 1057–1062, (Aug 2001).

[47] V B Tiwari, S Singh, H S Rawat, Manoranjan P Singh, and S C Mehendale. Electromagnetically induced transparency in cold ^{85}rb atoms trapped in the ground hyperfine f = 2 state. *Journal of Physics B: Atomic, Molecular and Optical Physics*, **43**(9), 095503, (2010).

[48] O. S. Mishina, M. Scherman, P. Lombardi, J. Ortalo, D. Felinto, A. S. Sheremet, A. Bramati, D. V. Kupriyanov, J. Laurat, and E. Giacobino. Electromagnetically induced transparency in an inhomogeneously broadened Λ transition with multiple excited levels. *Phys. Rev. A*, **83**, 053809, (May 2011).

[49] Richard R. Moseley, Sara Shepherd, David J. Fulton, Bruce D. Sinclair, and Malcolm H. Dunn. Two-photon effects in continuous-wave electromagnetically-induced transparency. *Optics Communications*, **119**(1), 61 – 68, (1995).

[50] M. Anil Kumar and Suneel Singh. Electromagnetically induced transparency and slow light in three-level ladder systems: Effect of velocity-changing and dephasing collisions. *Phys. Rev. A*, **79**, 063821, (Jun 2009).

[51] Dinh Xuan Khoa, Pham Van Trong, Le Van Doai, and Nguyen Huy Bang. Electromagnetically induced transparency in a five-level cascade system under doppler broadening: an analytical approach. *Physica Scripta*, **91**(3), 035401, (2016).

[52] Jianming Zhao, Lirong Wang, Liantuan Xiao, Yanting Zhao, Wangbao Yin, and Suotang Jia. Experimental measurement of absorption and dispersion in v-type cesium atom. *Optics Communications*, **206**(4), 341 – 345, (2002).

[53] A. Lazoudis, T. Kirova, E. H. Ahmed, P. Qi, J. Huennekens, and A. M. Lyyra. Electromagnetically induced transparency in an open v-type molecular system. *Phys. Rev. A*, **83**, 063419, (Jun 2011).

[54] Kang Ying, Yueping Niu, Dijun Chen, Haiwen Cai, Ronghui Qu, and Shangqing Gong. Observation of multi-electromagnetically induced transparency in v-type rubidium atoms. *Journal of Modern Optics*, **61**(8), 631–635, (2014).

[55] David J. Fulton, Sara Shepherd, Richard R. Moseley, Bruce D. Sinclair, and Malcolm H. Dunn. Continuous-wave electromagnetically induced transparency: A comparison of v, Λ, and cascade systems. *Phys. Rev. A*, **52**, 2302–2311, (Sep 1995).

[56] Shi Rao, Xiangming Hu, Jun Xu, and Lingchao Li. Optical switching of cross intensity correlation in cavity electromagnetically induced transparency. *Journal of Physics B: Atomic, Molecular and Optical Physics*, **50**(5), 055504, (2017).

[57] Marlan O. (Marlan Orvil) Scully and 1952 Zubairy, Muhammad Suhail. *Quantum optics*. Cambridge ; New York : Cambridge University Press. (1997). Includes bibliographical references and index.

[58] C. Cohen-Tannoudji, J. Dupont-Roc, G. Grynberg, and P. Thickstun. *Atom-Photon Interactions: Basic Processes and Applications*. Physics Textbook. Wiley. (1992).

[59] C.J. Foot. *Atomic physics*. Oxford master series in physics. Oxford University Press. (2005).

[60] P. D. Lett, W. D. Phillips, S. L. Rolston, C. E. Tanner, R. N. Watts, and C. I. Westbrook. Optical molasses. *J. Opt. Soc. Am. B*, **6**(11), 2084–2107, (Nov 1989).

[61] Christopher J Foot. *Atomic physics*. Oxford master series in atomic, optical and laser physics. Oxford University Press, Oxford. (2007).

[62] M. V. Pack, R. M. Camacho, and J. C. Howell. Electromagnetically induced transparency line shapes for large probe fields and optically thick media. *Phys. Rev. A*, **76**, 013801, (Jul 2007).

[63] S. M. Iftiquar, G. R. Karve, and Vasant Natarajan. Subnatural linewidth for probe absorption in an electromagnetically-induced-transparency medium due to doppler averaging. *Phys. Rev. A*, **77**, 063807, (Jun 2008).

[64] Serge Haroche and Francis Hartmann. Theory of saturated-absorption line shapes. *Phys. Rev. A*, **6**, 1280–1300, (Oct 1972).

[65] Arthur L. Schawlow. Spectroscopy in a new light. *Rev. Mod. Phys.*, **54**, 697–707, (Jul 1982).

[66] K. B. MacAdam, A. Steinbach, and C. Wieman. A narrowâĂŘband tunable diode laser system with grating feedback, and a saturated absorption spectrometer for cs and rb. *American Journal of Physics*, **60**(12), 1098–1111, (1992).

[67] Daryl W. Preston. DoppleräĂŘfree saturated absorption: Laser spectroscopy. *American Journal of Physics*, **64**(11), 1432–1436, (1996).

[68] P. R. S. Carvalho, Luís E. E. de Araujo, and J. W. R. Tabosa. Angular dependence of an electromagnetically induced transparency resonance in a doppler-broadened atomic vapor. *Phys. Rev. A*, **70**, 063818, (Dec 2004).

[69] M. Pinard, C. G. Aminoff, and F. Laloë. Velocity-selective optical pumping and doppler-free spectroscopy. *Phys. Rev. A*, **19**, 2366–2370, (Jun 1979).

[70] B. Gross, N. Papageorgiou, V. Sautenkov, and A. Weis. Velocity selective optical pumping and dark resonances in selective reflection spectroscopy. *Phys. Rev. A*, **55**, 2973–2981, (Apr 1997).

[71] Shrabana Chakrabarti, Amitkiran Pradhan, Biswajit Ray, and Pradip N Ghosh. Velocity selective optical pumping effects and electromagnetically induced transparency for d_2 transitions in rubidium. *Journal of Physics B: Atomic, Molecular and Optical Physics*, **38**(23), 4321, (2005).

[72] S. M. Iftiquar and Vasant Natarajan. Line narrowing of electromagnetically induced transparency in rb with a longitudinal magnetic field. *Phys. Rev. A*, **79**, 013808, (Jan 2009).

[73] M M Hossain, S Mitra, P Poddar, C Chaudhuri, B Ray, and P N Ghosh. Nonlinear resonances caused by coherent, optical pumping and saturating effects in the presence of three laser fields for the $^{85}rb\ d_2$ line. *Journal of Physics B: Atomic, Molecular and Optical Physics*, **44**(11), 115501, (2011).

[74] Vineet Bharti and Ajay Wasan. Electromagnetic induced transparency in the doppler broadened cascade transition with multiple excited levels. *Journal of Physics B: Atomic, Molecular and Optical Physics*, **45**(18), 185501, (2012).

[75] Chen, Zhuo Ren and Su, Xue Mei. Asymmetrical spectra due to atomic coherence of neighboring excited levels. *Eur. Phys. J. D*, **67**(7), 138, (2013).

[76] Thorsten Peters, Benjamin Wittrock, Frank Blatt, Thomas Halfmann, and Leonid P. Yatsenko. Thermometry of ultracold atoms by electromagnetically induced transparency. *Phys. Rev. A*, **85**, 063416, (Jun 2012).

[77] E. Figueroa, F. Vewinger, J. Appel, and A. I. Lvovsky. Decoherence of electromagnetically induced transparency in atomic vapor. *Opt. Lett.*, **31**(17), 2625–2627, (Sep 2006).

[78] Baolong Lü, W. H. Burkett, and Min Xiao. Electromagnetically induced transparency with variable coupling-laser linewidth. *Phys. Rev. A*, **56**, 976–979, (Jul 1997).

[79] Joyee Ghosh, R. Ghosh, F. Goldfarb, J.-L. Le Gouët, and F. Bretenaker. Analysis of electromagnetically induced transparency and slow light in a hot vapor of atoms undergoing collisions. *Phys. Rev. A*, **80**, 023817, (Aug 2009).

[80] M. Shuker, O. Firstenberg, Y. Sagi, A. Ben-kish, N. Davidson, and A. Ron. Ramsey-like measurement of the decoherence rate between zeeman sublevels. *Phys. Rev. A*, **78**, 063818, (Dec 2008).

[81] In-Ho Bae, Han Seb Moon, Min-Koeung Kim, Lim Lee, and Jung Bog Kim. Transformation of electromagnetically induced transparency into enhanced absorption with a standing-wave coupling field in an rb vapor cell. *Opt. Express*, **18**(2), 1389–1397, (Jan 2010).

[82] B. J. Feldman and M. S. Feld. Laser-induced line-narrowing effects in coupled doppler-broadened transitions. ii. standing-wave features. *Phys. Rev. A*, **5**, 899–918, (Feb 1972).

[83] Erkki Kyrölä and Rainer Salomaa. Probe spectroscopy in an inhomogeneously broadened three-level system saturated by an intense standing wave. *Phys. Rev. A*, **23**, 1874–1892, (Apr 1981).

[84] L. Roso, R. Corbalán, G. Orriols, R. Vilaseca, and E. Arimondo. Dressed-atom approach for probe spectroscopy in doppler-broadened three-level systems with standing-wave saturator. *Applied Physics B*, **31**(2), 115–129, (Jun 1983).

[85] F. Silva, J. Mompart, V. Ahufinger, and R. Corbalán. Electromagnetically induced transparency with a standing-wave drive in the frequency up-conversion regime. *Phys. Rev. A*, **64**, 033802, (Aug 2001).

[86] Z.R. Chen, X.M. Su, J.B. Kim, and Z.C. Zhuo. Observation of electromagnetically induced photonic band gaps in hot two-level atoms. *Journal of Modern Optics*, **61**(11), 898–903, (2014).

[87] Charu Mishra, A. Chakraborty, A. Srivastava, S. K. Tiwari, S. P. Ram, V. B. Tiwari, and S. R. Mishra. Electromagnetically induced transparency in λ-systems of ^{87}rb atom in magnetic field. *Journal of Modern Optics*, **65**(19), 2184–2192, (2018).

[88] Tom O'Haver. A pragmatic introduction to signal processing. *University of Maryland at College Park, College Park, MD, accessed Jan*, **14**, 2018, (1997).

[89] T.Y. Abi-Salloum, S. Snell, J.P. Davis, and F.A. Narducci. Variations of dispersion and transparency in four level n-scheme atomic systems. *Journal of Modern Optics*, **58**(21), 2008–2014, (2011).

[90] L.B. Kong, X.H. Tu, J. Wang, Yifu Zhu, and M.S. Zhan. Sub-doppler spectral resolution in a resonantly driven four-level coherent medium. *Optics Communications*, **269**(2), 362 – 369, (2007).

[91] Yong-qing Li and Min Xiao. Electromagnetically induced transparency in a three-level Λ-type system in rubidium atoms. *Phys. Rev. A*, **51**, R2703–R2706, (Apr 1995).

[92] C. Goren, A. D. Wilson-Gordon, M. Rosenbluh, and H. Friedmann. Atomic four-level *n* systems. *Phys. Rev. A*, **69**, 053818, (May 2004).

[93] M. Anil Kumar and Suneel Singh. Electromagnetically induced transparency and slow light in three-level ladder systems: Effect of velocity-changing and dephasing collisions. *Phys. Rev. A*, **79**, 063821, (Jun 2009).

[94] Somia Abd-Elnabi and KI Osman. Controllability of electromagnetically induced transparency in a doppler broadened four-level atomic system. *International Journal of Modern Physics B*, **27**(11), 1350037, (2013).

[95] Nathaniel B. Phillips, Irina Novikova, Eugeniy E. Mikhailov, Dmitry Budker, and Simon Rochester. Controllable steep dispersion with gain in a four-level n-scheme with four-wave mixing. *Journal of Modern Optics*, **60**(1), 64–72, (2013).

[96] Kang Ying, Yueping Niu, Dijun Chen, Haiwen Cai, Ronghui Qu, and Shangqing Gong. White light cavity via modification of linear and nonlinear dispersion in an n-type atomic system. *Optics Communications*, **342**, 189 – 192, (2015).

[97] Dinh Xuan Khoa, Pham Van Trong, Le Van Doai, and Nguyen Huy Bang. Electromagnetically induced transparency in a five-level cascade system under doppler broadening: an analytical approach. *Physica Scripta*, **91**(3), 035401, (2016).

[98] Khairul Islam, Dipankar Bhattacharyya, Arindam Ghosh, Debasish Biswas, and Amitava Bandyopadhyay. Study on probe field propagation in the presence of control and coupling fields through a four-level n-type atomic system. *Journal of Physics B: Atomic, Molecular and Optical Physics*, **50**(21), 215401, (2017).

[99] Anh Nguyen Tuan, Doai Le Van, and Bang Nguyen Huy. Manipulating multi-frequency light in a five-level cascade-type atomic medium associated with giant self-kerr nonlinearity. *J. Opt. Soc. Am. B*, **35**(6), 1233–1239, (Jun 2018).

[100] Masayoshi Nakano and Kizashi Yamaguchi. Numerical liouville approach: A calculation method for nonlinear optical susceptibilities of n-state systems. *Phys. Rev. A*, **50**, 2989–3004, (Oct 1994).

[101] Masayoshi Nakano and Kizashi Yamaguchi. Numerical liouville approach: intensity-dependent transient linear and nonlinear optical susceptibilities. *Chemical Physics Letters*, **234**(4), 323 – 329, (1995).

[102] P. R. Hemmer, M. S. Shahriar, V. D. Natoli, and S. Ezekiel. Ac stark shifts in a two-zone raman interaction. *J. Opt. Soc. Am. B*, **6**(8), 1519–1528, (Aug 1989).

[103] G. S. Agarwal. Nature of the quantum interference in electromagnetic-field-induced control of absorption. *Phys. Rev. A*, **55**, 2467–2470, (Mar 1997).

[104] Cui-Li Cui, Ji-Kui Jia, Yan Zhang, Yan Xue, Huai-Liang Xu, and Jin-Hui Wu. Resonant gain suppression and quantum destructive interference in a three-level open v system. *Journal of Physics B: Atomic, Molecular and Optical Physics*, **44**(21), 215504, (oct 2011).

[105] H. S. Moon, L. Lee, and J. B. Kim. Double resonance optical pumping effects in electromagnetically induced transparency. *Opt. Express*, **16**(16), 12163–12170, (Aug ts , url = http://www.opticsexpress.org/abstract.cfm?URI=oe-16-16-12163, doi = 10.1364/OE.16.012163,).

[106] T. Abi-Salloum, S. Meiselman, J.P. Davis, and F.A. Narducci. Four-level n-scheme in bare and quasi-dressed states pictures. *Journal of Modern Optics*, **56**(18-19), 1926–1932, (2009).

[107] Charu Mishra, A Chakraborty, S P Ram, S Singh, V B Tiwari, and S R Mishra. On electromagnetically induced transparency in n-systems in cold 87rb atoms. *Journal of Physics B: Atomic, Molecular and Optical Physics*, **53**(1), 015001, (dec 2019).

[108] Charu Mishra, A Chakraborty, and S R Mishra. Spectral characteristics of a modified inverted-y system beyond rotating wave approximation. *Journal of Physics B: Atomic, Molecular and Optical Physics*, **52**(9), 095002, (apr 2019).